Argonne
NATIONAL LABORATORY

ANL-HEP-TR-09-49

High-Power Radio Frequency Pulse Generation and Extraction Based on Wakefield Excited by an Intense Charged Particle Beam in Dielectric-Loaded Waveguides

---

High Energy Physics Division

About Argonne National Laboratory
Argonne is a U.S. Department of Energy laboratory managed by UChicago Argonne, LLC under contract DE-AC02-06CH11357. The Laboratory's main facility is outside Chicago, at 9700 South Cass Avenue, Argonne, Illinois 60439. For information about Argonne and its pioneering science and technology programs, see www.anl.gov.

Availability of This Report
This report is available, at no cost, at http://www.osti.gov/bridge. It is also available on paper to the U.S. Department of Energy and its contractors, for a processing fee, from:

U.S. Department of Energy
Office of Scientific and Technical Information
P.O. Box 62
Oak Ridge, TN 37831-0062
phone (865) 576-8401
fax (865) 576-5728
reports@adonis.osti.gov

HIGH-POWER RADIO FREQUENCY PULSE GENERATION AND EXTRACTION BASED ON WAKEFIELD EXCITED BY AN INTENSE CHARGED PARTICLE BEAM IN DIELECTRIC-LOADED WAVEGUIDES

BY

FENG GAO

DEPARTMENT OF ELECTRICAL AND COMPUTER ENGINEERING

Submitted in partial fulfillment of the
requirements for the degree of
Doctor of Philosophy in Electrical Engineering
in the Graduate College of the
Illinois Institute of Technology

Approved ______________________
Adviser

Chicago, Illinois
July 2009

ACKNOWLEDGEMENTS

It is a great honor for me to write this dissertation as a tribute to the promising research area, high-power wakefield extraction using dielectric-loaded structures. I could not have completed the Ph.D. research without the great support of my friends, colleagues and my family.

First I would like to thank Prof. Thomas T.Y. Wong for steering me into the field of microwave engineering, and for his consistent advice and support during my years at the Illinois Institute of Technology. I am also deeply grateful to Dr. Wei Gai, my supervisor in the High Energy Physics Division of Argonne National Laboratory. Dr. Gai has put a lot of effort into shaping my research attitude and guiding me in projects on beam-structure interaction. It is certainly a great experience to work in the Argonne Wakefield Accelerator group, and I appreciate the support from my colleagues. Dr. Manoel E. Conde, Mr. Richard Konecny, Dr. Zikri Yusof and Mr. Felipe Franchini have helped me in both engineering design and beam experiments, without whom the project could not have been successful; Dr. John G. Power has showed great patience in helping and guiding me in experimental setup and his enthusiasm is always inspiring to me; Dr. Wanming Liu has kindly given me expert support in numerical simulation and microwave component design; Dr. Chunguang Jing, Dr. Haitao Wang and Dr. Min Yan have not only helped me in research, but also encouraged me in many aspects during my stay in the U.S.; Ms. Malhotra Pramilia and Ms. Sandra Klepec have helped me with administrative support. I am very thankful to Dr. Paul Schoessow for his valuable suggestions in writing this thesis. I also want to express my appreciation to my friends

Dr. Feng Guo and Mr. Yang Wang. This research program is supported by the U. S. Department of Energy, Office of Science, under the Contract No. DE-AC02-06CH11357.

This dissertation is dedicated to my parents who have selflessly supported me from day one, and my endless love goes to my wife, Qingyan.

TABLE OF CONTENTS

CHAPTER

LIST OF TABLES

LIST OF FIGURES

LIST OF SYMBOLS

Symbol	Definition
α_0	Field Attenuation per Unit Length
β	Longitudinal Wave Propagation Constant
β_g	Group Velocity of RF Mode Normalized to the Speed of Light in Free Space
β_{gn}	Group Velocity of the *n*-th RF Mode Normalized to the Speed of Light in Free Space
δ_d	Loss Tangent of Dielectric
ε_0	Permittivity of Free Space
ε_r	Relative Permittivity
φ	Angular Position in Cylindrical Coordinates
λ	Laser Wavelength
λ_{RF}	RF Wavelength
τ_s	Length of RF Pulse Excited by a Single Particle Bunch
τ_t	Flat-top Duration of RF Pulse Excited by a Particle Bunch Train
ω	Angular Frequency
ω_n	Angular Frequency of the *n*-th Mode
σ_z	R.m.s. Length of a Particle Bunch
μ_0	Permeability of Free Space
$\Delta\lambda$	FWHM Bandwidth of Laser Source

Φ	Particle Bunch Shape Factor
a	Inner Radius of a Cylindrical Dielectric Tube
b	Outer Radius of a Cylindrical Dielectric Tube
c	Speed of Light in Free Space
f	Frequency
f_0	Synchronous Frequency of an RF Mode
f_b	Bunch Frequency in a Bunch Train
k_0	Wave Number of TEM Wave in Free Space
k_1	Cutoff Wave Number of a Waveguide Mode in the Vacuum Region of a Circular Cross Section Dielectric-loaded Waveguide
k_2	Cutoff Wave Number of the Waveguide Mode in the Dielectric Region of a Circular Cross Section Dielectric-loaded Waveguide
k_z	Longitudinal Wave Number
q	Charge per Bunch
r	Radial Position in Cylindrical Coordinates
r_L	Shunt Impedance per Unit Length
$[r/Q]$	Normalized Shunt Impedance per Unit Length of an Accelerating Mode
s	Distance between a Witness Point Charge and a Drive Bunch
t	Time

t_r	Rise-time of an RF Pulse Excited by a Train of Particle Bunches
t_f	Fall-time of an RF Pulse Excited by a Train of Particle Bunches
v_g	Group Velocity of a Wave
v_p	Phase Velocity of a Wave
z	Longitudinal Position in Cylindrical Coordinates
E	Energy of a Laser Pulse
E_a	Acceleration/Deceleration Gradient of an RF Mode
E_{as}	Acceleration/Deceleration Gradient of an RF Mode Excited by a Single Particle Bunch
E_{at}	Acceleration/Deceleration Gradient of an RF Mode Excited by a Particle Bunch Train
E_r	Radial Component of Electric Field in Cylindrical Coordinates
E_φ	Azimuthal Component of Electric Field in Cylindrical Coordinates
E_z	Longitudinal Component of Electric Field in Cylindrical Coordinates
H_r	Radial Component of Magnetic Field in Cylindrical Coordinates
H_φ	Azimuthal Component of Magnetic Field in Cylindrical Coordinates

H_z	Longitudinal Component of Magnetic Field in Cylindrical Coordinates
L	Length of a Decelerating Waveguide
P_w	Traveling-wave Power of an RF Mode
P_s	Traveling-wave Power of an RF Mode Excited by a Single Particle Bunch
P_t	Traveling-wave Power of an RF Mode Excited by a Particle Bunch Train
Q	Total Quality Factor (including Metallic and Dielectric Losses)
Q_w	Wall Quality Factor (including Metallic Losses Only)
T	Period of the Operational Frequency of the Gun and the Linac
T_b	Bunch Frequency in a Bunch Train
U	Stored Energy per Unit Length

ABSTRACT

Power extraction using a dielectric-loaded (DL) waveguide is a way to generate high-power radio frequency (RF) waves for future particle accelerators, especially for two-beam-acceleration. In a two-beam-acceleration scheme, a low-energy, high-current particle beam is passed through a deceleration section of waveguide (*decelerator*), where the power from the beam is partially transferred to trailing electromagnetic waves (wakefields); then with a properly designed RF output coupler, the power generated in the decelerator is extracted to an output waveguide, where finally the power can be transmitted and used to accelerate another usually high-energy low-current beam. The decelerator, together with the RF output coupler, is called a *power extractor*.

At Argonne Wakefield Accelerator (AWA), we designed a 7.8GHz power extractor with a circular DL waveguide and tested it with single electron bunches and bunch trains. The output RF frequency (7.8GHz) is the sixth harmonic of the operational frequency (1.3GHz) of the electron gun and the linac at AWA. In single bunch excitation, a 1.7ns RF pulse with 30MW of power was generated by a single 66nC electron bunch passing through the decelerator. In subsequent experiments, by employing different splitting-recombining optics for the photoinjector laser, electron bunch trains were generated and thus longer RF pulses could be successfully generated and extracted. In 16-bunch experiments, 10ns and 22ns RF pulses have been generated and extracted; and in 4-bunch experiments, the maximum power generated was 44MW with 40MW extracted.

A 26GHz DL power extractor has also been designed to test this technique in the millimeter-wave range. A power level of 148MW is expected to be generated by a bunch

train with a bunch spacing of 769ps and bunch charges of 20nC each. The arrangement for the experiment is illustrated in a diagram.

Higher-order-mode (HOM) power extraction has also been explored in a dual-frequency design. By using a bunch train with a bunch spacing of 769ps and bunch charges of 50nC each, 90.4MW and 8.68MW of extracted power levels are expected to be reached at 20.8GHz and 35.1GHz, respectively. In order to improve efficiency in HOM power extraction, a novel technique has been proposed to suppress unintended modes.

CHAPTER 1

INTRODUCTION

To study the elementary constituents of matter and radiation in the high energy regime, colliders with center-of-mass energy on the order of TeV have been constructed or proposed, such as the large hadron collider (LHC) (CERN 2008)[*] and the international linear collider (ILC) (Brau 2007). In the LHC, the proton-proton collision energy reaches 14TeV, while in the ILC the electron-positron collision energy reaches 500GeV. To achieve such high energy, the charged particles need to be properly accelerated using high-power sources. This motivates research on new high-power radio frequency (RF) sources based on new accelerating structures, i.e. the dielectric-loaded (DL) waveguide.

In this chapter, the basics on accelerators will be addressed first, and then one of the new acceleration techniques, DL acceleration will be introduced. Some traditional high-power RF sources and the power extraction method will also be described.

1.1 Particle Accelerator Fundamentals

Over the past few decades, continuous efforts have been put into the development of particle accelerators, where the main goal is to reach higher beam energy. In this section, we first present a brief history of particle accelerators. Afterwards the DL waveguide used in this power extraction project is introduced.

1.1.1 History of Particle Accelerators. The particle accelerator was originally developed as an alternative to radioactive sources and cosmic rays to reach higher particle energy for atomic research. The electrostatic (DC) accelerator was invented first,

---

[*] Corresponding to references in the Bibliography.

and the RF accelerator was developed later to reach higher energies that cannot be achieved by DC accelerators.

One of the first particle accelerators was the 700KV DC Cockcroft-Walton generator developed in 1930s. The first fully man-controlled atom splitting was realized with its generated 400KV protons (Cockcroft 1932). In this accelerator the DC voltage is generated with capacitors and rectifiers, and the acceleration is implemented with electrodes. About the same time, Van de Graaff developed another type of DC accelerator, where charge is physically transported with a belt to generate 1.5MV of voltage for acceleration (Van de Graaff 1931). At that time the particle energy could not be higher than the accelerating voltage inside a DC machine. To overcome this limitation, the tandem accelerator was developed that makes use of the accelerating voltage twice by stripping electrons from ions being accelerated. Currently the highest energy tandem accelerator (24.5MV) operates at the Oak Ridge National Laboratory (Bair 1975).

Although the tandem accelerator is able to push the particle energy higher than the maximum voltage inside the machine, it is still not good enough for further high energy physics research. Therefore, instead of DC acceleration, resonant acceleration using alternating fields was proposed by Ising in 1924 (Bryant 1993). Inspired by this concept, Wideröe built a prototype radio frequency (RF) linear accelerator with alternating drift tubes to generate a 50KeV beam, powered by a 1MHz, 25KV oscillator (Waloschek 1994). Since in the early days a linear accelerator was hard to build due to its large size, a fixed frequency cyclotron was proposed by Ernest Lawrence in 1929, where magnetic fields were used to guide the particle to follow half-circle traces and acceleration was performed by the electrical field inside the gap between two "D"s

(Lawrence 1930). However, despite the compact circular shape of the cyclotron, the particle energy was limited by relativistic effects, where the movement of the particle cannot remain synchronized with the applied constant frequency RF accelerating field when the particle energy becomes very high. A new circular accelerator, the synchrotron was introduced to replace the cyclotron for higher energy acceleration (McMillan 1945). Unlike the cyclotron, the synchrotron uses distributed bending magnets and accelerating structures, allowing the machine to be built to be much larger than the cyclotron. In a synchrotron, the particle is made to travel in a closed loop by strong magnetic fields, where the particle emits electromagnetic waves due to a change in its travel direction. This well known phenomenon is called synchrotron radiation and is the basis of many of today's X-ray sources. For example, the Advanced Photon Source (APS) located at the Argonne National Laboratory (ANL) has an electron storage ring with an 1104m circumference, which consists of 40 straight sections (APS 2008). A 7GeV electron beam circulates in the storage ring and emits X-rays at 35 insertion device sections, while 5 other sections are used as RF accelerators to replenish the energy lost by the beam due to synchrotron radiation. Although synchrotron radiation is useful for X-ray generation, the energy loss $\Delta E \propto E^4$ makes it difficult to efficiently accelerate particles to high energies in a circular machine.

For the RF linear accelerator, on the other hand, synchrotron radiation is a weak effect. This makes it a suitable candidate for accelerating particles to high energy. There are primarily two types of structures used in RF acceleration: the standing-wave structure and the traveling-wave structure. For particles whose velocity is only a small portion of the speed of light in free space c (for example $0.01c$), the standing-wave structure is most suitable, because the structure can be easily designed to accommodate the fast changing speed of the particles during the acceleration process. For example, in Wideröe's accelerators, increasing lengths of successive drift tubes ensures that the particles always reach an acceleration gap between two drift tubes when the accelerating field in the gap has the correct phase (Bryant 1993; Waloschek 1994). For ultra-relativistic particles whose velocity is nearly c (for example an electron at 5MeV has a velocity $0.996c$), the traveling-wave structure can also be used. In traveling-wave acceleration, the phase velocity of the acceleration mode is designed to be equal to c, thus ultra-relativistic particles can be placed to always ride the crest of the RF wave for continuous acceleration. For a traveling-wave structure, the design of the RF input/output coupler is not as critical as that for a standing-wave device. Usually the former has a much wider bandwidth than the latter, thus the central frequency of the couplers does not need to be as accurate.

One of the most well known RF linear accelerators is the Stanford two-mile-long accelerator, which is able to accelerate electrons and positrons to 50GeV (Neal 1968). This accelerator, like many others, uses circular disc-loaded waveguides as accelerating structures. A circular waveguide is a fast wave structure which means the phase velocity of the mode is larger than c, so the wave cannot synchronize with any particles since the particle velocity is always smaller than c. Therefore, the circular waveguide is loaded with discs to slow down the phase velocity, which is equivalent to a series of RF cavities coupled to each other through irises (the inner holes of the discs). This traditional structure is designed with a smooth inner surface to avoid breakdown. Superconducting cavities have also been widely used to reduce power consumption (Proch 1998). One property of the disc-loaded accelerator is that it is not uniform in the longitudinal direction; therefore its cost is high due to complicated design, fabrication, tuning and assembly.

1.1.2 Dielectric-loaded Particle Acceleration. Some traditional cavity-based accelerators encounter breakdown problems for RF pulse lengths on the order of hundreds of nanoseconds when the gradient reaches ~100MV/m (Aldophsen 2007). In order to push the acceleration gradient even higher, alternative acceleration techniques have been extensively investigated, such as DL acceleration (Zhang 1997; Zou 2000), laser acceleration (Plettner 2005) and laser-plasma acceleration (Leemans 2006).

Among various advanced accelerator concepts, the DL accelerator can be traced back to the early 1950's (Flesher 1951) and is a potential candidate for future high gradient particle acceleration. Although there are two main types of DL accelerators, one based on rectangular waveguides (Zhang 1997) and one based on circular waveguides (Zou 2000), in this thesis we concentrate on the latter.

As shown in Figure 1.1, the circular DL waveguide consists of a cylindrical metallic tube partially filled with dielectric material in the region $a \le r \le b$, and a vacuum channel in the region $0 \le r < a$, for the beam. The dielectric tube (the region $a \le r \le b$) is used to slow down the phase velocity of the acceleration mode to the velocity of ultra-relativistic particles. Usually, the TM_{01} mode is used as the acceleration mode since it has the strongest interaction with an on-axis beam. By changing the inner and outer radii, and the permittivity of the dielectric, the structure can be tuned so that the phase velocity is set to the particle velocity at the desired frequency. Compared with the traditional, disc-loaded metallic waveguide with similar RF properties, the dielectric-

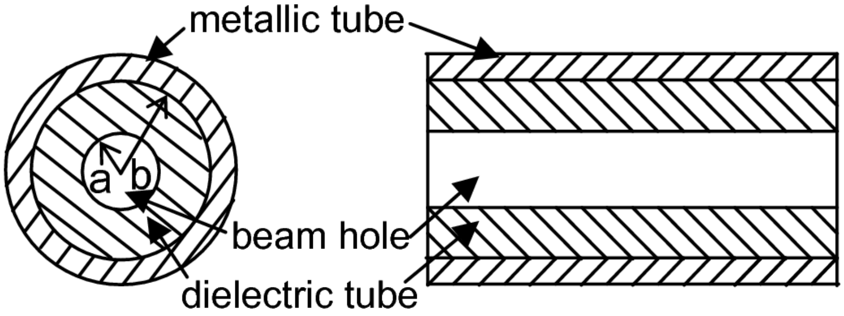

Figure 1.1. Transverse and Longitudinal Cross-sectional Views of the Circular Dielectric-loaded Waveguide. *a* and *b* are the inner and outer radii of the dielectric tube, respectively.

loaded waveguide is potentially simpler to fabricate due to its uniformity in the longitudinal direction, especially when high precision is needed at high frequencies (Zou 2000). Furthermore, a simple scheme is available for damping the undesired deflection modes (Chojnacki 1991). There is an ongoing program in the AWA group at Argonne National Laboratory (ANL) to develop DL acceleration. An X-band DL accelerator has been developed (Zou 2001), and Several standing-wave DLA structures have been tested under high gradients up to 100MV/m (Conde 2007). Recently lower power loss and higher acceleration efficiency multilayer DL structures were proposed (Jing 2005), and an enhanced transformer ratio was shown in a ramped bunch train test in a DLA structure (Jing 2007). Different materials such as Cordierite ($\varepsilon_r = 4.6 \sim 4.76$), MCT-20 ($\varepsilon_r = 20$), Alumina ($\varepsilon_r = 9.4$) and quartz ($\varepsilon_r = 3.75$) have been used for different applications, which give useful experience on choosing dielectric materials and solving breakdown problems.

1.2 High-power RF Sources for Particle Acceleration

High-power RF sources are the "pumps" of RF accelerators, and various RF sources have been developed mainly based on one of three mechanisms (Gold 1997): Cherenkov/Smith-Purcell radiation, transition radiation and bremsstrahlung. For example, the traveling-wave tube (TWT) and backward-wave oscillator (BWO) are based on Cherenkov/Smith-Purcell radiation, the klystron is based on transition radiation, and the gyrotron is based on bremsstrahlung. In the following subsections, first some well known and widely used traditional high-power RF sources are introduced, and then a more recent particle acceleration scheme, the two-beam-acceleration (TBA) and associated RF power generation and extraction are described.

1.2.1 Traditional High-power RF Sources for Particle Accelerators. The most well known high-power RF source for accelerators is the klystron, which can be traced back to 1939 (Varian 1939). A typical klystron consists of two standing-wave cavities: a bunching cavity and an output cavity. The electrons are first generated on the surface of a thermocathode, then pushed out of the cathode by a DC voltage between the cathode and a ring anode. The DC voltage is usually a few hundred kilovolts and the beam current is usually a few hundred amperes. Then, the generated DC electron beam is guided via focusing solenoids to pass through the two cavities. In the bunching cavity, the electron beam is modulated by a weak RF input signal. The beam becomes a train of electron bunches with the same spacing as the RF period. Then, the modulated beam drifts in a cutoff tube to the operating RF mode, and travels into the output cavity, where the beam power is transferred to RF power by exciting electromagnetic fields. The RF power is then coupled out to power acceleration devices. For a klystron, the size of the cavities and the drift-tube radius become smaller when the frequency becomes higher. For high-power application at higher frequencies, especially in the millimeter-wave range, the traditional klystron is no longer suitable since the size of the structure will becomes so small that the beam current cannot be high enough to generate that much power. An example of state-of-the-art klystrons is the SLAC X5011, which can generate a 600ns pulse with 62MW of power at 11.4GHz (Wilson 1996).

Gyrodevices, unlike the traditional linear beam tubes such as TWTs and klystrons, are based on the electron cyclotron maser instability (Baker 2001; Granatstein 1997). For gyrodevices, the tube diameter can be larger than the wavelength of the output electromagnetic (EM) signal, thus much higher frequencies can be reached than that for the linear beam tubes. The gyrodevices have two main categories: gyrotron oscillators and the gyrotron amplifiers. Gyrotron amplifiers are of more interest for particle acceleration since the phase of the output signal can be easily controlled through an input signal. The gyroklystron, as the corresponding gyrodevice of the linear beam klystron, has been extensively investigated (Blank 1997; Cheng 1999; Gouveia 2002; Ives 2003; Lawson 1992). The gyroklystron can generate 10MW of power at a frequency as high as 91GHz (Blank 1997).

Another type of high power RF source is the magnicon (Nezhevenko 1994). A typical magnicon uses the interaction of a gyrating pencil electron beam and rotating TM modes to generate high power. In a simplified version of the magnicon, the particle beam first comes out of an electron gun then gets deflected in a series of deflecting cavities by a rotating TM mode, and spun up to high transverse momentum by a magnetic field after a drift section. Upon entering into the output cavity, the gyrating beam excites another rotating TM mode, whose frequency is the same as or a multiple of that of the mode in the deflecting cavities. Currently, at the Naval Research Laboratory (NRL), the X-band magnicon can produce 25MW of power with a pulse length of 200ns and a repetition rate of 10Hz (Gold 2007). At a much higher frequency, 34GHz, 17MW of power has also been generated (Nezhevenko 2005).

1.2.2 The TBA Scheme and Power Extraction. Aside from the traditional RF sources, an alternative way to generate higher RF power based on traveling-wave wakefield power extraction has been investigated, and the related acceleration method is called the TBA. Just like a boat excites waves when traveling in a river, a charged particle excites electromagnetic (EM) fields inside an accelerating/decelerating structure when an effective interaction between the particle and the structure exists. The excited fields are called wakefields because they are always behind the particle if the particle travels at a speed *c*, the speed of light in free space. The wakefields excited by a particle beam can act back on the beam, and this may cause beam instabilities under certain conditions (Chao 1993). Although wakefields often play a harmful role in beam dynamics, they also can be used as a "medium" for energy exchange between two beams.

As an example, Figure 1.2 shows the longitudinal electrical field (E_z) excited by an ultra-relativistic particle beam (the speed of the beam is equal to *c*) consisting of a positively charged Gaussian bunch inside a circular DL waveguide. The traveling bunch experiences a negative axial electric field E_z, which means it is being decelerated, and part of the beam power is transferred to the excited EM fields, i.e. wakefields. High wakefield power can be obtained by optimizing the following two factors: the ability of such a structure to interact with the beam (often quantified by "r over Q" or a loss factor), and the bunch charge of the beam (the beam current is often used for describing periodic bunches). The first factor, either for a traveling-wave or a standing-wave structure, is usually optimized by adjusting the physical dimensions of the structure to obtain higher accelerating/decelerating gradient for given power. The second factor, i.e. the charge which contributes to wakefield generation, can be optimized by maximizing the charge transmitted from the particle source (an electron gun etc.) to the interaction structure. For example, for an electron beamline with a photocathode, the ways to increase charge include increasing the input laser power onto the cathode, increasing the quantum efficiency (QE) of the photocathode, optimizing the launch phase of the electron beam with respect to the EM wave externally fed into the gun and the linac, and using

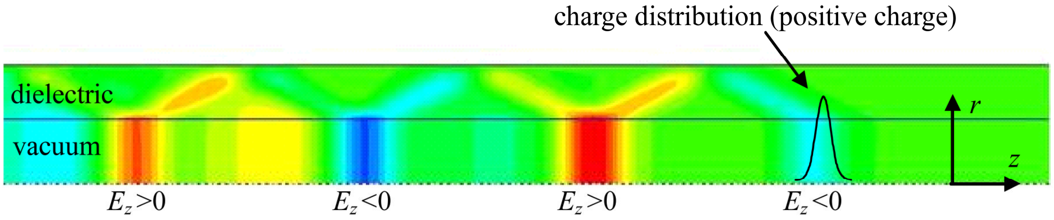

Figure 1.2. Longitudinal Electric Wakefield Excited by an Ultra-relativistic Positively Charged Gaussian Particle Bunch inside a Circular Dielectric-loaded Waveguide.

focusing magnets in the beamline (Gai 1987), etc. However, high bunch charge (high beam current) leads to strong beam instabilities, which can greatly change the beam profile and may generate strong unwanted higher-order-modes (HOMs).

Figure 1.3 shows a diagram of the TBA concept powered by a wakefield as discussed above. This idea can be traced back to the 1980's (Sessler 1982) and one of the best known applications is the CERN-CLIC system (Braun 1998). As shown in the figure, a typical TBA scheme consists of three stages: i) RF power is extracted from a low-energy, high-current beam (*drive beam*) within decelerating sections; ii) RF power is coupled out of the decelerating sections into output waveguides; and iii) RF power is delivered into accelerating sections for acceleration of the high-energy, low-current beam (Gao 2008). This option may overcome some of the limitations of high-power RF generation, transfer, and pulse compression compared to a traditional klystron-based system (Braun 1998; Kübner 1992) at frequencies above X-band (Danly 1995) and power levels beyond a few hundred megawatts (Gai 2001). This is due to the ease with which the RF power characteristics can be changed by manipulating the decelerating sections and its drive bunch. It has been demonstrated that a properly designed TBA scheme can provide RF power on the order of gigawatts (Sessler 1987).

In Figure 1.3, a decelerating section (*decelerator*) together with the RF coupler used to couple power into an output waveguide is referred to as a *power extractor* in this thesis. Therefore, for high output power, the decelerator needs to be properly designed so that the power of the beam can be efficiently transferred to the excited wakefields, and the RF coupler also needs to be properly designed so that the wakefield power can be efficiently coupled to the output waveguide.

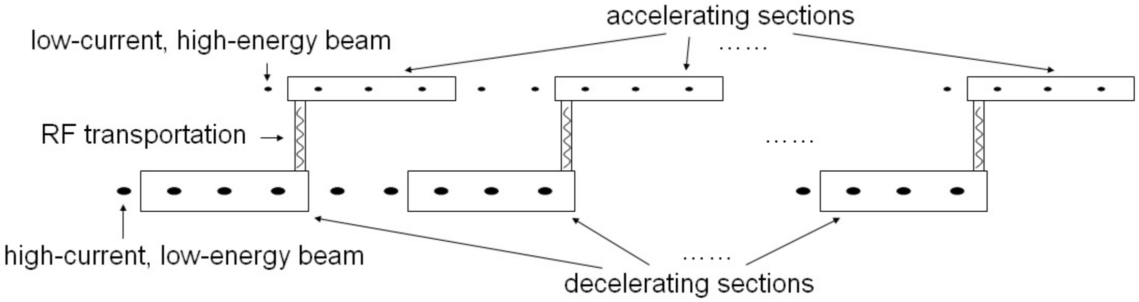

Figure 1.3. Conceptual Diagram for Two-beam-acceleration. A high-current, low-energy beam (*drive beam*) is passed through decelerating sections, where its kinetic energy is transferred to generated RF wakefields and transported to separate RF structures to accelerate a low-current, high-energy beam (*witness beam*).

The decelerator in principle is not much different from an accelerator, which can be either a traditional metallic disc-loaded structure (or one of its cousins based on coupled cavities or corrugated waveguides), or a DL waveguide as described in Section 1.1.2. The decelerator is a traveling wave structure, but unlike an externally powered traveling-wave accelerator which needs both input and output RF ports, it only needs one port for RF output.

The use of a DL waveguide as part of an RF power extractor was first proposed in 1991 (Chojnacki 1991) and later, a 7.8GHz structure producing 3.4MW of power was generated by a 24nC single bunch (Conde 1999). A 21 GHz structure was tested at the CTF2 (Newsham 2003).

Maintaining both the simple geometry of a dielectric loaded cavity and similar electrical properties of a traditional RF structure, in this project we designed a 7.8GHz circular DL waveguide as a decelerator to be used at the present AWA beamline. Measurements show that ~10ns and ~22ns RF pulses with a few megawatts of power have been successfully generated by electron bunch trains consisting of 16 electron bunches, and 44MW of saturation power has been reached by a train consisting of 4 bunches. With the new high QE photocathode, we expect generation of power on the order of 100MW.

The remainder of this thesis is organized as follows: in Chapter 2, theoretical background on the circular DL waveguide and power extraction is introduced; in Chapter 3, designs for the 7.8GHz power extractor (including the decelerator and the RF output coupler), an auxiliary RF bidirectional coupler, and a high vacuum flange-gasket set are shown; in Chapter 4, the setup for 7.8GHz beam tests is described; in Chapter 5, results of the 7.8GHz beam tests are shown and analyzed; in Chapter 6, the design of a future 26GHz power extractor is given, in Chapter 7 HOM power extraction is introduced at frequencies of 20.8GHz and 35.1GHz and Chapter 8 concludes the thesis.

CHAPTER 2

THEORY OF POWER EXTRACTION WITH A DIELECTRIC-LOADED WAVEGUIDE

As introduced in Chapter 1, this 7.8GHz power extractor was designed with a circular DL waveguide, and the RF power comes from an electron drive beam. In this chapter, first the mathematical expressions for the fields of the interacting modes inside the circular DL waveguide are given, and then derivations of the power generated by a drive beam are shown.

2.1 Guided Wave in a Circular Dielectric-loaded Waveguide

For the DL waveguide shown in Figure 1.1, guided waves exist only when they satisfy the boundary conditions. Here a summary of analytical results from Dr. Peng Zou's thesis, completed at the Illinois Institute of Technology, are given as follows (Zou 2001):

$$
\begin{aligned}
E_z &= \begin{cases} B_1 J_m(k_1 r)\cos(m\phi)e^{j(\omega t-\beta z)} & 0 \le r < a \\ B_2[J_m(k_2 r) - \dfrac{J_m(k_2 b)}{Y_m(k_2 b)} Y_m(k_2 r)]\cos(m\phi)e^{j(\omega t-\beta z)} & a \le r \le b \end{cases} \\
H_z &= \begin{cases} A_1 J_m(k_1 r)\sin(m\phi)e^{j(\omega t-\beta z)} & 0 \le r < a \\ A_2[J_m(k_2 r) - \dfrac{J_m{}'(k_2 b)}{Y_m{}'(k_2 b)} Y_m(k_2 r)]\sin(m\phi)e^{j(\omega t-\beta z)} & a \le r \le b \end{cases}
\end{aligned}
\tag{2.1a}
$$

$$
\begin{aligned}
E_\phi &= \begin{cases} \left[\dfrac{j\omega\mu_0}{k_1} A_1 J_m{}'(k_1 r) + \dfrac{j\beta m}{k_1{}^2 r} B_1 J_m(k_1 r)\right]\sin(m\phi)e^{j(\omega t-\beta z)} & 0 \le r < a \\ \left[\dfrac{j\omega\mu_0}{k_2} A_2 G_{mm}{}'(k_2 r) + \dfrac{j\beta m}{k_2{}^2 r} B_2 F_{mm}(k_2 r)\right]\sin(m\phi)e^{j(\omega t-\beta z)} & a < r \le b \end{cases} \\
E_r &= \begin{cases} \left[-\dfrac{j\omega\mu_0 m}{k_1{}^2 r} A_1 J_m(k_1 r) - \dfrac{j\beta}{k_1} B_1 J_m{}'(k_1 r)\right]\cos(m\phi)e^{j(\omega t-\beta z)} & 0 \le r < a \\ \left[-\dfrac{j\omega\mu_0 m}{k_2{}^2 r} A_2 G_{mm}(k_2 r) - \dfrac{j\beta}{k_2} B_2 F_{mm}{}'(k_2 r)\right]\cos(m\phi)e^{j(\omega t-\beta z)} & a < r \le b \end{cases}
\end{aligned}
\tag{2.1b}
$$

$$H_\phi = \begin{cases} \left[-\dfrac{j\omega\varepsilon_0}{k_1} B_1 J_m{}'(k_1 r) - \dfrac{j\beta m}{k_1{}^2 r} A_1 J_m(k_1 r) \right] \cos(m\phi) e^{j(\omega t - \beta z)} & 0 \le r < a \\ \left[-\dfrac{j\omega\varepsilon_r\varepsilon_0}{k_2} B_2 F_{mm}{}'(k_2 r) - \dfrac{j\beta m}{k_2{}^2 r} A_2 G_{mm}(k_2 r) \right] \cos(m\phi) e^{j(\omega t - \beta z)} & a < r \le b \end{cases} \tag{2.1c}$$

$$H_r = \begin{cases} \left[-\dfrac{j\omega\varepsilon_0 m}{k_1{}^2 r} B_1 J_m(k_1 r) - \dfrac{j\beta}{k_1} A_1 J_m{}'(k_1 r) \right] \sin(m\phi) e^{j(\omega t - \beta z)} & 0 \le r < a \\ \left[-\dfrac{j\omega\varepsilon_r\varepsilon_0 m}{k_2{}^2 r} B_2 F_{mm}(k_2 r) - \dfrac{j\beta}{k_2} A_2 G_{mm}{}'(k_2 r) \right] \sin(m\phi) e^{j(\omega t - \beta z)} & a < r \le b \end{cases}$$

where a is the radius of the vacuum region, b is the outer radius of the ceramic tube. B_1, B_2, A_1 and A_2 are the field amplitudes in the region $0 \le r < a$ (vacuum) and $a \le r \le b$ (dielectric) respectively, v_p is the phase velocity of the wave traveling inside the tube, ω is the angular frequency of the wave. Also k_1 and k_2 are cutoff wave numbers in the region $0 \le r < a$ and $a \le r \le b$ respectively, β is the propagation constant in z direction, ε_0 and μ_0 are the permittivity and permeability of free space respectively, and ε_r is the relative permittivity of the dielectric. Their relationship is expressed as follows, where k_0 is the wave number in free space:

$$\begin{aligned} k_1 &= \omega\sqrt{\frac{1}{c^2} - \frac{1}{v_p{}^2}} \\ k_2 &= \omega\sqrt{\frac{\varepsilon_r}{c^2} - \frac{1}{v_p{}^2}} \\ \beta^2 &= k_0{}^2 - k_1{}^2 = \varepsilon_r k_0{}^2 - k_2{}^2 \\ k_0{}^2 &= \omega^2 \mu_0 \varepsilon_0 \end{aligned} \tag{2.2}$$

J_m and Y_m are m-th order Bessel functions of the first and second kinds respectively, and

$$\begin{aligned} F_{mm}(k_2 r) &= J_m(k_2 r) - \frac{J_m(k_2 b)}{Y_m(k_2 b)} Y_m(k_2 r) \\ G_{mm}(k_2 r) &= J_m(k_2 r) - \frac{J_m{}'(k_2 b)}{Y_m{}'(k_2 b)} Y_m(k_2 r) \\ F_{mm}{}'(k_2 r) &= J_m{}'(k_2 r) - \frac{J_m(k_2 b)}{Y_m(k_2 b)} Y_m{}'(k_2 r) \\ G_{mm}{}'(k_2 r) &= J_m{}'(k_2 r) - \frac{J_m{}'(k_2 b)}{Y_m{}'(k_2 b)} Y_m{}'(k_2 r) \end{aligned} \tag{2.3}$$

Using the boundary conditions at $r = a$ (E_z, E_ϕ, H_ϕ, and H_z continuous), the dispersion relation of guided wave traveling in this waveguide can be obtained as

$$\begin{aligned}&\left[\frac{\mu_0}{k_1 a}\frac{J_m'(k_1 a)}{J_m(k_1 a)}-\frac{\mu_0}{k_2 a}\frac{G_{mm}'(k_2 a)}{G_{mm}(k_2 a)}\right]\left[\frac{\varepsilon_0}{k_1 a}\frac{J_m'(k_1 a)}{J_m(k_1 a)}-\frac{\varepsilon_r\varepsilon_0}{k_2 a}\frac{F_{mm}'(k_2 a)}{F_{mm}(k_2 a)}\right]\\&=\frac{(\beta m\omega)^2}{(k_1 k_2 a)^4}(\mu_0\varepsilon_r\varepsilon_0-\mu_0\varepsilon_0)^2\end{aligned} \tag{2.4}$$

In applications to particle acceleration, if the beam is traveling on the axis of the waveguide, the family of TM$_{0n}$ modes (n = 1, 2, …) will interact with the beam. For the TM$_{0n}$ mode, the electric and magnetic field components can be simplified as

$$\begin{aligned}E_z &= \begin{cases} B_1 J_0(k_1 r)e^{j(\omega t-\beta z)} & 0 \le r < a \\ B_2\left[J_0(k_2 r)-\dfrac{J_0(k_2 b)}{Y_0(k_2 b)}Y_0(k_2 r)\right]e^{j(\omega t-\beta z)} & a \le r \le b \end{cases}\\ E_r &= \begin{cases} -\dfrac{j\beta}{k_1}B_1 J_0'(k_1 r)e^{j(\omega t-\beta z)} & 0 \le r < a \\ -\dfrac{j\beta}{k_2}B_2 F_{00}'(k_2 r)e^{j(\omega t-\beta z)} & a < r \le b \end{cases}\\ H_\phi &= \begin{cases} -\dfrac{j\omega\varepsilon_0}{k_1}B_1 J_0'(k_1 r)e^{j(\omega t-\beta z)} & 0 \le r < a \\ -\dfrac{j\omega\varepsilon_r\varepsilon_0}{k_2}B_2 F_{00}'(k_2 r)e^{j(\omega t-\beta z)} & a < r \le b \end{cases}\end{aligned} \tag{2.5}$$

The dispersion relation of the TM$_{0n}$ modes is given by the following equation

$$\left[\frac{1}{k_1}\frac{J_0'(k_1 a)}{J_0(k_1 a)}-\frac{\varepsilon_r}{k_2}\frac{F_{00}'(k_2 a)}{F_{00}(k_2 a)}\right]=0 \tag{2.6}$$

From Equations 2.2 and 2.5, we note that when the TM$_{0n}$ mode has a phase velocity $v_p = c$, the longitudinal electric field E_z inside the beam hole is independent of the radial position r. This means that there are no focusing and defocusing forces for a relativistic particle traveling on axis inside the beam hole according to the Panofsky-Wenzel theorem (Vaganian 1995), and this can possibly reduce the occurrence of beam instabilities.

From Equations 2.2 and 2.6, it can be seen that once a and b of the waveguide are set, and v_p is set to be equal to c, there are a series of angular frequencies which satisfy the equations, denoted ω_n ($n = 1, 2, \ldots$), corresponding to the family of TM_{0n} modes. In this project the TM_{01} mode was chosen to be the decelerating mode since it interacts most strongly with the beam.

2.2 Beam–structure Interaction in a Dielectric-loaded Waveguide

In this section, the RF power level and RF pulse duration excited by a drive beam (a bunch or bunch train) in a DL waveguide are described (Gao 2008).

2.2.1 General Relationships for the Traveling-wave Waveguide. We will need to make use of two general relationships of the traveling-wave waveguide so we begin by recalling them here for completeness (Wangler 1998). For each mode in the structure, the relationship between the longitudinal accelerating field amplitude, E_a, and the stored energy per unit length, U, are related through the accelerator figure of merit 'r over Q'

$$\left[\frac{r}{Q}\right] = \frac{E_a^{\,2}}{\omega U} \tag{2.7}$$

where ω is the angular frequency of the mode. The $[r/Q]$ of each mode can be calculated with standard EM codes such as CST Microwave Studio (CST 2003). The travelling-wave power, P_w, is related to E_a through

$$P_w = \frac{E_a^{\,2}}{2\alpha_0 r_L} \tag{2.8}$$

where $\alpha_0 = \omega / 2Qv_g$ is the field attenuation per unit length, v_g is the group velocity, and r_L is the shunt impedance per unit length. This shunt impedance can be calculated from knowledge of the quality factor Q of the structure and $[r/Q]$ since $r_L = Q \times [r/Q]$.

2.2.2 The Beam Driven Traveling-wave Waveguide. Consider a charged particle beam (the drive bunch) traveling down the axis of a DL waveguide (the decelerator) of the length L. The drive bunch will excite wakefield that carries travelling-wave power, P_w, into the modes of the structure. In this article, the drive bunch (or drive bunch train) is considered ultra-relativistic (the particle velocity equals c, the speed of light in free space).

2.2.2.1 Time Structure of the RF Pulse. Let a drive bunch traveling in the $z+$ direction enter the decelerator of length L at the moment $t = 0$ and location $z = 0$ (Figure 2.1(a)). At time t when the bunch is still inside the decelerator (Figure 2.1(b)), the head of the RF pulse (moving at c) is located at $z = ct$, while the tail of the RF pulse (moving at v_g) is located at $z = v_g t$. When the bunch (and the head of the RF pulse) reaches the downstream end ($z = L$) of the decelerator (Figure 2.1(c)) the time is $t = L/c$ and the tail of the RF pulse has reached the position $z = v_g L/c$. At this moment, the generated RF pulse would begin to be extracted by an RF coupler (not shown) at $z = L$, but in this heuristic description we imagine the RF packet propagating out of the end of the decelerator at $z = L$. The final event occurs when the tail of the RF pulse exits the decelerator (Figure 2.1(d)) at time $t = L/v_g$. The duration of the RF pulse is the difference between the moment the bunch reaches the exit ($t = L/c$) and the moment the tail of the RF pulse reaches the exit ($t = L/v_g$).Therefore, the RF pulse duration for single-bunch excitation is given by

$$\tau_s = L(1-\beta_g)/v_g \tag{2.9}$$

where $\beta_g = v_g/c$ is the group velocity normalized to c.

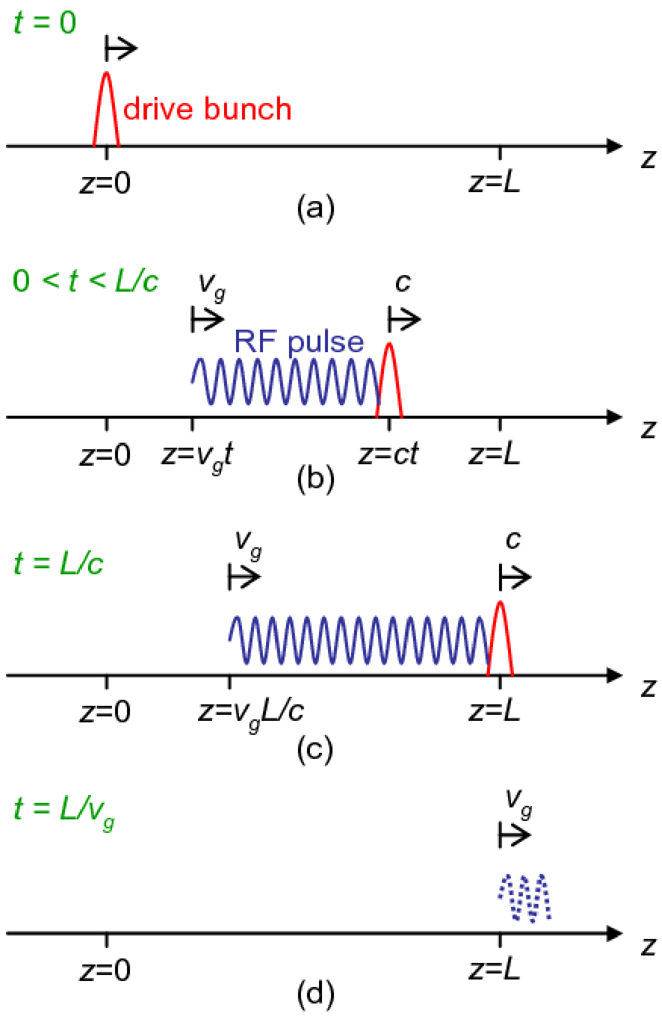

Figure 2.1. The RF Pulse due to a Single Drive Bunch. Snapshots of a single bunch and the excited RF pulse inside the decelerator region $0 \le z \le L$. (a) the bunch enters the decelerator ($t = 0$); (b) the bunch and the RF pulse are fully inside the decelerator where the head and the tail of the RF pulse travel at different speed ($0 < t < L/c$); (c) the bunch reaches the exit of the decelerator ($t = L/c$); (d) the tail of the RF pulse exits the decelerator ($t = L/v_g$).

Now let us consider the field build-up process due to bunch-train excitation. If a second bunch reaches the exit after the first bunch but before the tail of the first RF pulse, then there will be a region where the RF pulses of the two bunches overlap. To create constructive interference (in-phase superposition) of the excited RF fields, the *synchronous frequency* f_0 (at which the phase velocity of the mode is equal to c) of the excited RF mode is chosen to be a harmonic of the bunch frequency, $1/T_b$, for a train of n bunches evenly spaced in time by T_b.

The build-up in time of the amplitude of the longitudinal electrical field due to a bunch train (E_{at}) at the exit of the decelerator ($z = L$) is shown in Figure 2.2. (Note: This is the field that would be observed by an antenna located at $z = L$ and we have now redefined the reference time so that $t = 0$ corresponds to arrival of the first bunch at $z = L$.) The RF pulses excited by individual bunches are labeled in patterns and the increasing amplitude of the net field (E_{at}) is due to superposition. The time structure of the bunch train RF pulse (at $z = L$) consists of a rise-time, a flat-top, and a fall-time; all of which are determined by the overlap of the individual single-bunch RF pulses. The rise-time is determined by the number of bunches whose RF pulses overlap with the first RF pulse and is equal to $\mathit{ceiling}(\tau_s / T_b) - 1$. For example, if the single-bunch pulse length is $\tau_s = 2.4\text{ns}$ and the bunches are spaced at $T_b = 0.769\text{ns}$, then there will be $\mathit{ceiling}(2.4/0.769) - 1 = 3$ trailing bunches whose RF pulses overlap with the first RF pulse. In general, the number of RF pulses that overlap at the exit of the decelerator is $N = \mathit{ceiling}(\tau_s / T_b)$. From Figure 2.2, it can be seen for a long bunch train with $n \geq N$, the rise-time t_r can be written as

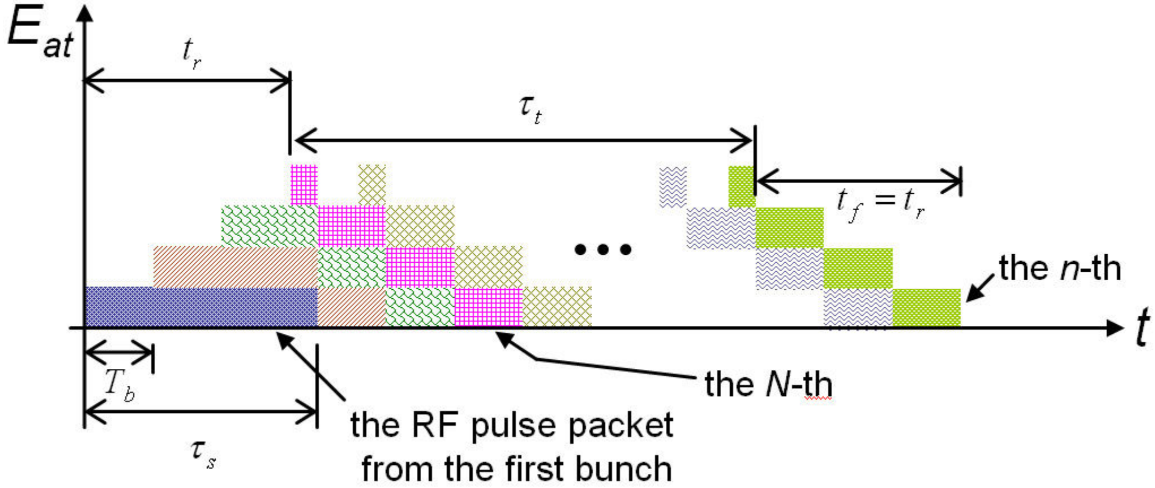

Figure 2.2. The RF Pulse due to a Drive Bunch Train. The longitudinal electrical field amplitude measured at the exit of the decelerator with bunch train excitation. (RF pulses excited by different bunches are labeled with different patterns).

$$t_r = (N-1) \times T_b \tag{2.10a}$$

Similarly the fall-time is

$$t_f = t_r \tag{2.10b}$$

The steady-state (flat-top) duration of the RF pulse is simply the total length duration minus the rise-time and the fall-time, i.e.

$$\tau_t = (n-1) \times T_b + \tau_s - 2t_r \tag{2.10c}$$

Note that for a very long train ($n >> N$) the pulse length is simply $\tau_t \approx nT_b$.

2.2.2.2 Pulsed RF Power Generated by Ultra-relativistic Drive Bunches. In this subsection, we provide expressions for the travelling-wave power excited by a single drive bunch, P_s, and a train of n drive bunches with $n \geq N$, P_t.

When a charged particle bunch (drive bunch) passes through the decelerator it excites a wakefield which, in turn, carries a traveling-wave power P_w. We define the direction of the traveling wave as $z+$, the entrance of the decelerator as $z = 0$, and its exit as $z = L$. In the absence of an external RF power source all RF power comes from the wakefield of the drive bunch. For each mode, the power decreases along the length of the structure as

$$\frac{dP_w}{dz} = -2\alpha_0 P_w \tag{2.11}$$

where α_0 is the field attenuation per unit length. In the presence of an infinitely long charged particle bunch train with bunch spacing T_b and bunch charge q, a second term representing the power increase per unit length due to the wakefield must be added to Equation 2.11 (Whittum 1998)

$$\frac{dP_w}{dz} = \frac{qE_a}{T_b} - 2\alpha_0 P_w \tag{2.12}$$

where it is assumed that all the particles experience the same deceleration gradient E_a (i.e. the bunch length is short compared to the mode wavelength, $\sigma_z << \lambda_{RF}$, so that all particles within the bunch experience the same RF phase).

For nonzero bunch length, the particles within a bunch experience different deceleration gradients less than or equal to the on-crest gradient E_a and therefore a bunch form factor Φ is added to Equation 2.12

$$\frac{dP_w}{dz} = \frac{qE_a}{T_b}\Phi - 2\alpha_0 P_w \tag{2.13}$$

where for an ultra-relativistic bunch, Φ is expressed as (Wilson 1991; Yu 2002)

$$\Phi = \left| \frac{1}{q}\int_{-\infty}^{+\infty} f(z) e^{-jk_z z} dz \right| \tag{2.14}$$

$f(z)$ is the spatial charge distribution for one bunch, and k_z is the longitudinal wave number of the RF field. In other words, Φ is just the Fourier transform of the charge distribution function, $f(z)$. For simplicity, we have dropped the explicit k_z dependence ($\Phi(k_z) = \Phi$) since the above equations apply to each mode individually. It is straightforward to show that for a Gaussian spatial bunch distribution $f(z) = \frac{q}{\sigma_z\sqrt{2\pi}}\exp\left(-\frac{z^2}{2\sigma_z^2}\right)$, with r.m.s. length σ_z, that the form factor is given by

$$\Phi = \exp[-(k_z\sigma_z)^2/2] \tag{2.15}$$

Following the derivation by D. Whittum (Whittum 1998), for a constant impedance structure ($r_L = \text{constant}$), by substituting Equation 2.8 into Equation 2.13 we can get

$$\frac{d}{dz}\left(\frac{E_a^2}{2\alpha_0 r_L}\right)=\frac{q\Phi E_a}{T_b}-\frac{E_a^2}{r_L} \tag{2.16}$$

$$\frac{dE_a}{dz}+\alpha_0 E_a=\frac{q\Phi\alpha_0 r_L}{T_b} \tag{2.17}$$

$$\frac{d}{dz}\left(E_a e^{\alpha_0 z}\right)=\frac{q\Phi\alpha_0 r_L}{T_b}e^{\alpha_0 z} \tag{2.18}$$

$$E_a(z)=e^{-\alpha_0 z}\left[E_a(0)+\frac{q\Phi\alpha_0 r_L}{T_b}\int_0^z e^{\alpha_0\tau}d\tau\right] \tag{2.19}$$

We can further simplify this expression by realizing that the bunch must travel some distance before losing energy, or $E_a(0)=0$. Therefore, Equation 2.19 can be rewritten as

$$E_a(z)=\frac{r_L q}{T_b}\left(1-e^{-\alpha_0 z}\right)\Phi \tag{2.20}$$

At the exit of the decelerator ($z=L$), the longitudinal electrical field amplitude is

$$E_{at}=E_a(L)=\frac{r_L q}{T_b}\left(1-e^{-\alpha_0 L}\right)\Phi \tag{2.21}$$

Finally, substituting Equation 2.21 into Equation 2.8, one obtains the power level at the end of the deceleration waveguide as

$$P_t=q^2\frac{k_z}{4\beta_g}\left[\frac{r}{Q}\right]\left(\frac{1-e^{-\alpha_0 L}}{\alpha_0 T_b}\right)^2\Phi^2 \tag{2.22}$$

Furthermore, when the decelerator is lossless ($\alpha_0=0$), Equation 2.22 can be modified as

$$P_t=q^2\frac{k_z}{4\beta_g}\left[\frac{r}{Q}\right]\left(\frac{L}{T_b}\right)^2\Phi^2 \tag{2.23}$$

If the particle beam only contains a single bunch, the power level generated can be obtained by modifying Equation 2.23 if we arrange for the net RF pulse to be constant.

This can be done by changing the decelerator length, *L*, so that the single-bunch pulse duration, τ_s, is exactly the same as the bunch spacing T_b. In this case, the individual RF pulses exit the decelerator stacked one after the other, without overlap or a gap between them, according to the illustration in Figure 2.2. Therefore, the power level calculated from Equation 2.23 will be the same as that excited by a single bunch. In other words, by replacing T_b with τ_s in Equation 2.23, we obtain the power level at the exit of a lossless decelerator excited by a single bunch

$$P_s = q^2 \frac{k_z \beta_g}{4} \left[\frac{r}{Q}\right] \left(\frac{c}{1-\beta_g}\right)^2 \Phi^2 \tag{2.24}$$

For a lossy ($\alpha_0 \neq 0$) structure, Equation 2.24 can be modified to yield Equation 2.25

$$P_s(t) = q^2 \frac{k_z \beta_g}{4} \left[\frac{r}{Q}\right] \left(\frac{c}{1-\beta_g}\right)^2 \Phi^2 e^{-2\alpha_0 v_g t} \qquad (0 \le t \le \tau_s) \tag{2.25}$$

where $t = 0$ is the moment the bunch exits the decelerator, i.e. the moment the head of the excited RF pulse exits the decelerator.

From Equation 2.23 and Equation 2.24, it can be easily shown that for a lossless structure

$$P_t = \left(\frac{\tau_s}{T_b}\right)^2 P_s \tag{2.26}$$

where we recall that $n \ge N$. The lower and upper limits of the power level excited by a bunch train are given by

$$(N-1)^2 P_s < P_t \le N^2 P_s \tag{2.27}$$

CHAPTER 3

DESIGN OF THE 7.8GHZ DIELECTRIC-LOADED POWER EXTRACTOR

In this chapter, the design of the 7.8GHz DL power extractor is described, including theoretical calculation, numerical simulation, mechanical fabrication and low power RF tests (cold tests). Through the procedures shown in this chapter, the power extractor was prepared for the final beam tests, which will be described in Chapter 5.

As shown in Figure 3.1, this DL power extractor includes two parts: a circular cross section DL waveguide as the decelerator at the upstream side, and an RF output coupler at the downstream side. The decelerator has a dielectric tube enclosed by a metal sleeve to reduce the phase velocity of RF waves. Inside the dielectric is a vacuum channel for the drive beam to pass. In Figure 3.1 an electron beam excites RF waves while traveling through the decelerator, then exits the power extractor through an opening on the RF output coupler at the downstream side, which is below cutoff for the RF wave that is to be extracted. With a properly designed RF output coupler, the power of the excited RF pulse is extracted from the DL waveguide to an output waveguide, which in this thesis is chosen to be a standard rectangular waveguide.

To monitor the extracted RF wave, an RF bidirectional coupler is needed in the output waveguide. At 7.8GHz, a high-power high-vacuum bidirectional coupler is not commercially available, thus the design of such a bidirectional coupler is shown. A special RF flange-gasket set is also designed for this high-vacuum application at 7.8GHz. The flange-gasket is designed for good electrical contact between two flanges, while high vacuum is kept at the same time.

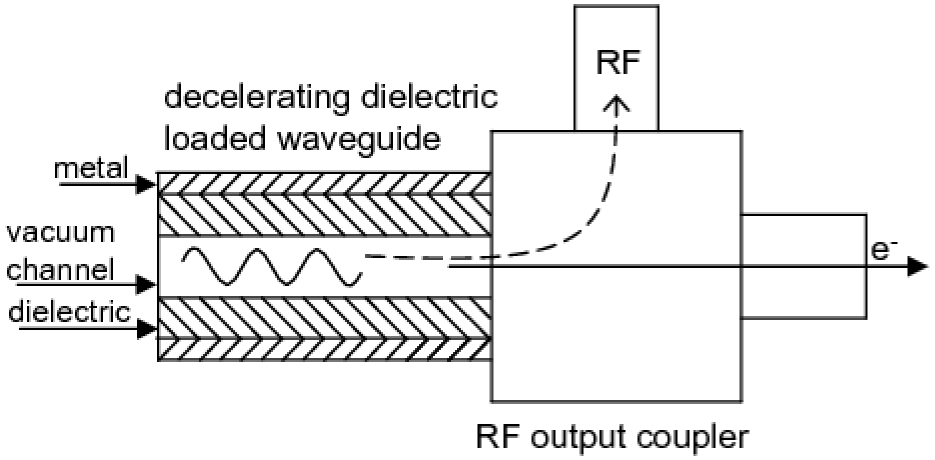

Figure 3.1. A Dielectric-loaded Power Extractor. It consists of a dielectric-loaded decelerator and an RF output coupler.

3.1 Design of the 7.8GHz Dielectric-loaded Decelerator

The design goal for the decelerator is to generate power as large as possible with given drive beam. From inspection of Equations 2.22 and 2.25, it is seen that high RF power is generated when several decelerator design constraints are met: i) the inner radius, a, should be large to allow for high beam-charge transmission but small to keep $[r/Q]$ high; ii). the length, L, should be long to increase the field superposition in multi-bunch excitation; iii). the group velocity v_g should be small in multi-bunch excitation for stronger field superposition but also large to reduce the rise time; iv). the attenuation coefficient should be small to reduce power loss. In other words, the final design is a tradeoff between these requirements.

The TM_{01} mode is chosen to be the operation mode of the power extractor because it has the strongest coupling with an on-axis beam; therefore the RF output coupler is specifically designed for transition from the TM_{01} mode to the TE_{10} mode, the operating mode of the output rectangular waveguide. However, inside the decelerator, besides the TM_{01} mode, other TM_{0n} modes ($n = 2, 3, \ldots$) are also excited, but with smaller amplitudes. If the beam is displaced off axis, dipole and quadruple modes, such as the hybrid HEM_{11} will also be excited, which may contribute to beam instability. The power of these higher order modes are usually not extracted to the output waveguide since the RF output coupler is not designed for these modes. In this section, first the design of the decelerator based on the TM_{01} mode is shown, and then the higher order modes are also analyzed. As a reminder, the electron beam in calculation is assumed to be ultra-relativistic, thus it has a velocity of c.

3.1.1 Design of the Decelerator Based on the TM_{01} Mode. The CST MAFIA T2 solver (CST 2000) is used to calculate the gradients E_{as} excited by a single bunch and E_{at} by a bunch train respectively, from which we can calculate the traveling-wave power inside the structure. In the simulations, a Gaussian electron bunch with bunch length $\sigma_z = 2\text{mm}$ (typical for the beam test) is used, and the bunch charge is set to 1nC for scaling purposes. In the experiment the expected charge range is 1-100nC. The dielectric material is Cordierite with a relative permittivity 4.6.

The final optimized parameters of the structure for generating high traveling-wave power P_t are listed in Table 3.1. The synchronous frequency of the excited TM_{01} mode was chosen to be 7.8GHz, which is the 6th harmonic of the fundamental frequency of the AWA electron gun and linac (1.3 GHz). For this proof-of-principle test, 7.8GHz gives a large bunch form factor ($\Phi = 0.95$), and also does not require high precision in fabrication. Figure 3.2 gives the dispersion curve of the TM_{01} mode inside this DL waveguide, where it can be seen this curve intersects the light line in free space (on which each point has a phase velocity of c) at 7.8GHz. This means the TM_{01} mode has a phase velocity of c at 7.8GHz, thus it can synchronize with the ultra-relativistic electron beam which has a velocity of c.

For single bunch excitation, the longitudinal electrical field excited in the 7.8GHz peak is plotted in Figure 3.3(a); it can be seen that the RF pulse length is 2.2ns, while the pulse length given by Equation 2.9 is 2.9ns. The difference is due to end effects at the upstream side of the decelerator, where a cutoff plug is used to secure the dielectric tube.

For a bunch train, the build-up of the longitudinal electric field excited by 10 consecutive bunches is shown in Fig. 3.3(b). Close inspection of the simulated fields

Table 3.1. Design Parameters of the 7.8GHz Dielectric-loaded Decelerator.

RF frequency	f_0	7.8GHz
Inner diameter of the dielectric tube	$2a$	12.04mm
Outer diameter of the dielectric tube	$2b$	22.34mm
Dielectric tube length	L	266mm
Relative permittivity of the dielectric	ε_r	4.6
Normalized group velocity of the RF mode	β_g	0.23
Loss tangent of the ceramic	δ_d	5×10^{-4}
Wall quality factor (metallic wall losses only)	Q_w	8777
Total quality factor (metallic wall and dielectric losses)	Q	2745
"r over Q" per unit length of the structure	$[r/Q]$	6.09 KΩ/m

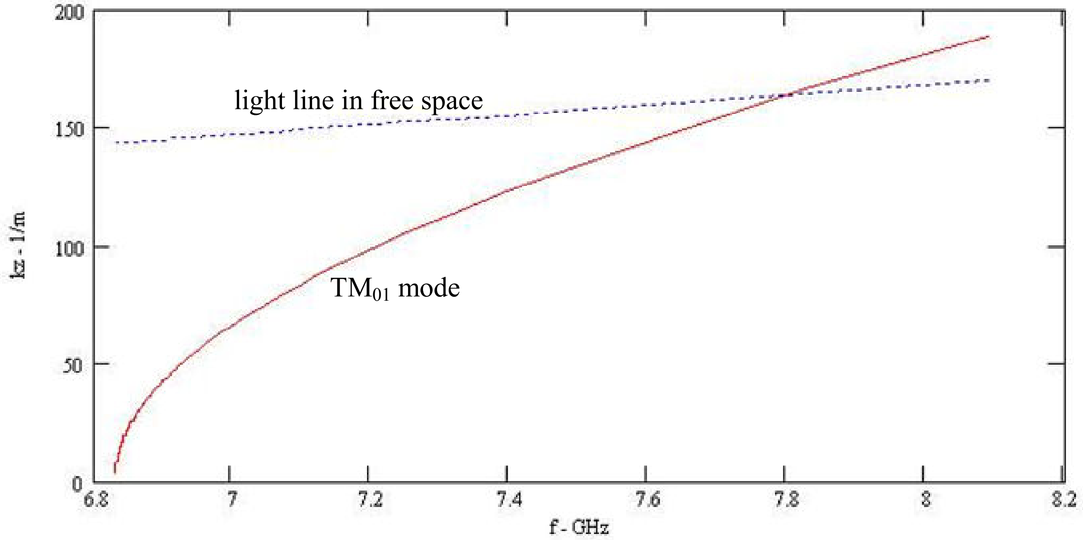

Figure 3.2. Dispersion Curve of the TM_{01} Mode in the Dielectric-loaded Waveguide. The dotted line describes the wave number of light with respect to frequency in free space, so any point on this line has a phase velocity of *c*.

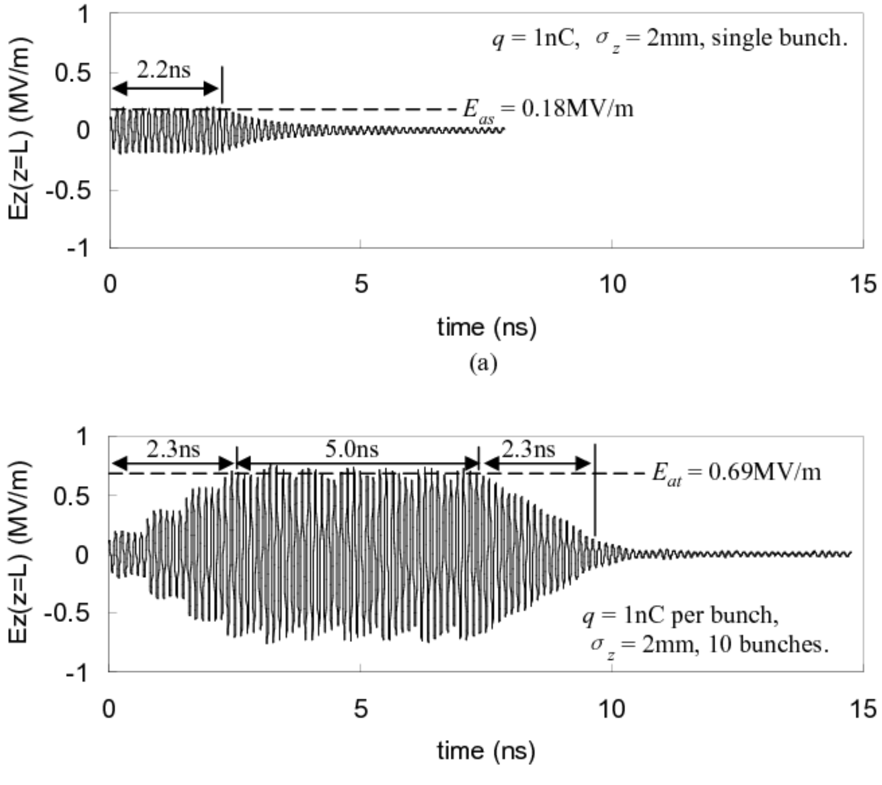

(a)

(b)

Figure 3.3. MAFIA Simulation of the Gradient at the End of the Decelerator. The gradient induced by (a) a single bunch and (b) a train of 10 bunches.

shows that the field reaches saturation after 4 pulses, with a rise time of 2.3ns, a flat-top length of 5.0ns and a fall time of 2.3ns. The rise time and the fall time agree with the values given by Equations 2.10(a) and (b), and the flat-top length is slightly different than the 5.2ns calculated with Equation 2.10(c). The RF pulse will increase in length as more bunches are added, but will not increase in power because there will be no overlap of RF pulses generated from bunches that are far apart. The simulated gradients (E_{as} for a single bunch and E_{at} for a bunch train) and power levels (P_s for a single bunch and P_t for a bunch train) listed in Table 3.2 are seen to be in good agreement with the results from Equations 2.25 and 2.22. In addition, we emphasize that the power is proportional to the square of the bunch charge as expected from Equation 2.25 and Equation 2.22.

3.1.2 TM$_{0n}$ (n = 1, 2, 3, …) Modes and the Hybrid HEM$_{11}$ Mode inside the Decelerator. When the beam travels in the decelerator, it excites the whole family of TM$_{0n}$ modes because in Equation 2.6 when k_1 is set to zero ($v_p = c$), k_2 and thus ω and β have multiple roots, corresponding to all the TM$_{0n}$ modes (n = 1, 2, …). In other words, the dispersion curves of these TM$_{0n}$ modes intersect the light line at different frequencies, so theoretically the whole family of TM$_{0n}$ modes can be excited. However, the higher modes have smaller [r/Q]s, and for a finite bunch length they have exponentially decreasing bunch shape factors, thus from Equation 2.22 only the lowest a few modes are excited significantly. Also since in Equation 2.5 the Bessel function $J_m(0)$ has a nonzero value only when $m = 0$, no hybrid mode can be excited when the beam travels on axis.

The distributions of the longitudinal electrical field E_z with respect to the radial position of the first five TM$_{0n}$ modes are shown in Figure 3.4, where for each mode the field is normalized to its on-axis value. It can be seen for all the modes, E_z in the beam

Table 3.2. Gradient and Power Generated in the Structure of Table 3.1 Driven by a Single Gaussian Bunch and a Bunch Train. E_{as}, P_s for a single bunch and E_{at}, P_t for a bunch train. The bunch length σ_z = 2mm.

	single bunch		bunch train	
	$E_{as} \propto q$	$P_s \propto q^2$	$E_{at} \propto q$	$P_t \propto q^2$
q = 1nC	0.18MV/m	0.0079MW	0.69MV/m	0.11MW
q = 100nC	18.0 MV/m	79MW	69MV/m	1.1GW

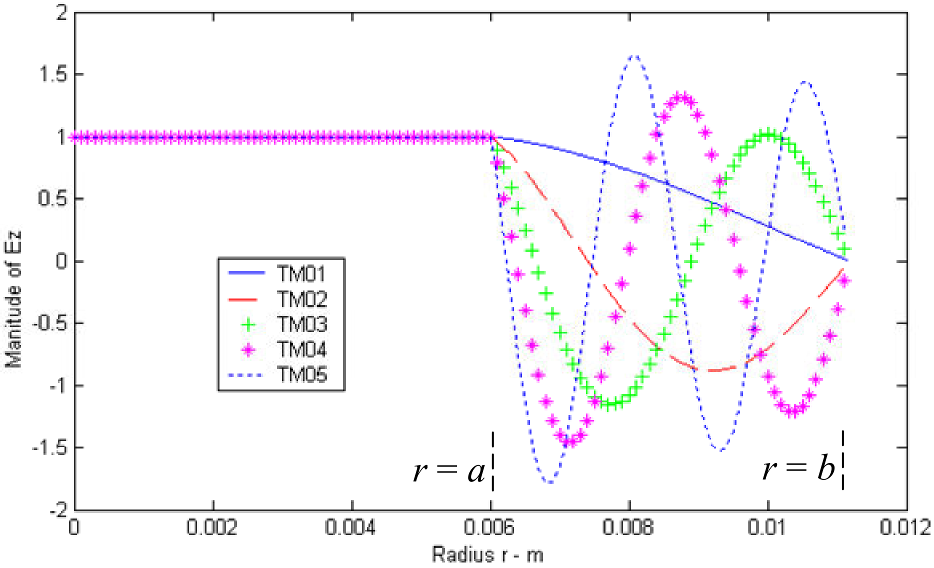

Figure 3.4. E_z Transverse Distribution of TM$_{0n}$ Modes. For each mode the magnitude is normalized to its on-axis value.

channel is independent of r, in agreement with Equation 2.5. We can further observe that the TM_{01} mode only has a zero at the outer edge of the dielectric tube ($r = b$), and the TM_{0n} has n zeros. The use of these high order modes has also been investigated for particle acceleration with a multilayer dielectric loaded waveguide (Jing 2005). In Table 3.3 the properties of the first five TM_{01} modes are listed, including the synchronous frequency f_0, the $[r/Q]$ which describes how much these modes interact with the beam, the group velocities v_g, and finally the bunch shape factors Φ of the modes. It can be seen for a higher order mode both $[r/Q]$ and the bunch shape factor are smaller.

For single bunch excitation, Figure 3.3(a) only shows the longitudinal electrical field of the TM_{01} mode. To take into account higher order modes, a geometry to calculate the wakefield of the drive bunch is shown in Figure 3.5. A Gaussian drive bunch travels in the z+ direction, which is followed by a point witness charge at a distance s behind the head of the drive bunch. Although a Gaussian bunch is infinitely long in both z- and z+ directions, in practical calculations it can be cut at $\pm 5\sigma_z$ from the center, where the charge density is only 0.000004 times the maximum value. With this geometry, the wakefield can be calculated as (Braun 1998; Jing 2004):

$$E_z(s) = \frac{q}{2\sigma_z\sqrt{2\pi}} \sum_n \left\{ \frac{\omega_n}{\left(1-\beta_{gn}\right)} \left[\frac{r}{Q}\right]_n \int_s^0 \cos\left(\omega_n \frac{u}{c}\right) \exp\left[-\frac{\left(s-u-5\sigma_z\right)^2}{2\sigma_z^2}\right] du \right\} \tag{3.1}$$

Here the wakefield calculated with Equation (3.1) is shown as a blue solid line in Figure 3.6, where only the first five TM_{0n} modes are counted. The wakefield simulated with the MAFIA T2 solver is shown as a red dashed line, and a very good agreement between the numerical and analytical results is found. When the electron bunch

Table 3.3. Properties of TM_{0n} Modes in the DL Waveguide When $v_p = c$.

Modes	TM_{01}	TM_{02}	TM_{03}	TM_{04}	TM_{05}
f_0 (GHz)	7.80	20.9	34.9	49.3	64.0
$[r/Q]$ (KΩ/m)	6.09	1.97	0.773	0.352	0.182
$\beta_g = v_g/c$	0.232	0.305	0.377	0.422	0.449
Φ	0.95	0.68	0.34	0.30	0.027

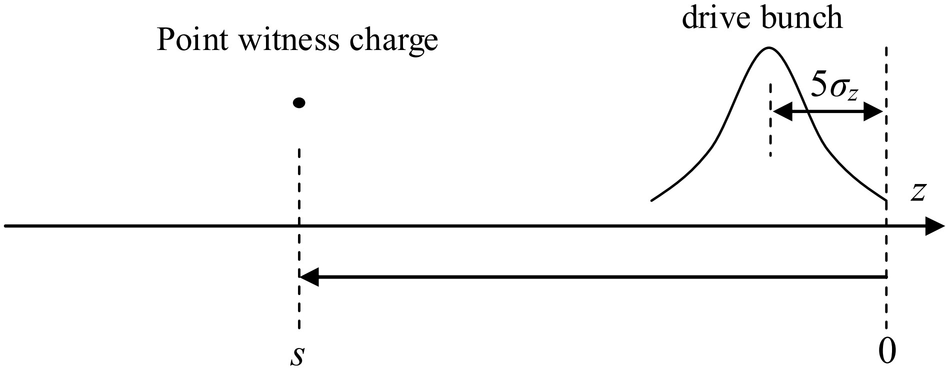

Figure 3.5. Geometry for Wakefield Calculation.

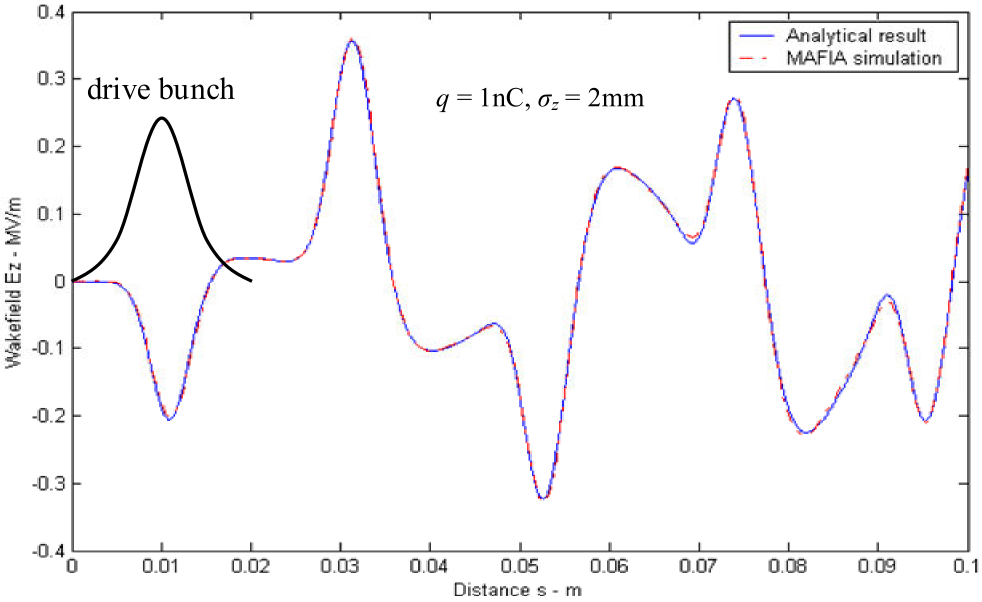

Figure 3.6. On-axis Longitudinal Wakefield in the Dielectric-loaded Waveguide.

length increases, the longitudinal wakefield is weaker, and the fundamental mode is more dominant, as shown in Figure 3.7.

The previous discussion is based on the assumption that the beam is traveling on-axis. If the beam is not centered, then besides the TM_{0n} modes, hybrid modes with higher azimuthal indices will be excited. The dipole HEM_{11} mode is the most harmful hybrid mode, because with a phase velocity of c, its frequency is usually close to and below that of the TM_{01} mode. The HEM_{11} mode generated by an off-axis beam can drive the beam farther away from the axis and possibly scrape the ceramic surface. The dispersion curve of the HEM_{11} mode inside the waveguide is shown in Figure 3.8, in which it can be seen that the curve intersects the light line at 6.49GHz, which is close to five times the bunch frequency. This means the beam needs to be centered as well as possible, otherwise for a bunch train coherent enhancement of this hybrid mode may occur. The MAFIA 3D Particle-in-Cell code TS3 provides a fully self-consistent solution for Maxwell's equations and the equations of motion in the time domain, and is an appropriate tool to analyze the effect of an off-axis beam (CST 2000). The disadvantage of this approach is that it requires a very large memory and a very long calculation time.

3.2 Design of the 7.8GHz RF Output Coupler

The output waveguide to which the RF power will be extracted, as shown in Figure 3.1, was chosen to be the commonly used WR112 waveguide. In order to extract the RF power from the decelerator to this WR112 waveguide, a TM_{01}-TE_{10} RF output coupler with a center frequency 7.8GHz is needed. In order that very short RF pulses (as small as 10ns for some future dielectric-based accelerator concepts) can be extracted, the desired bandwidth (in which the insertion loss is better than -3dB) is more than 200MHz.

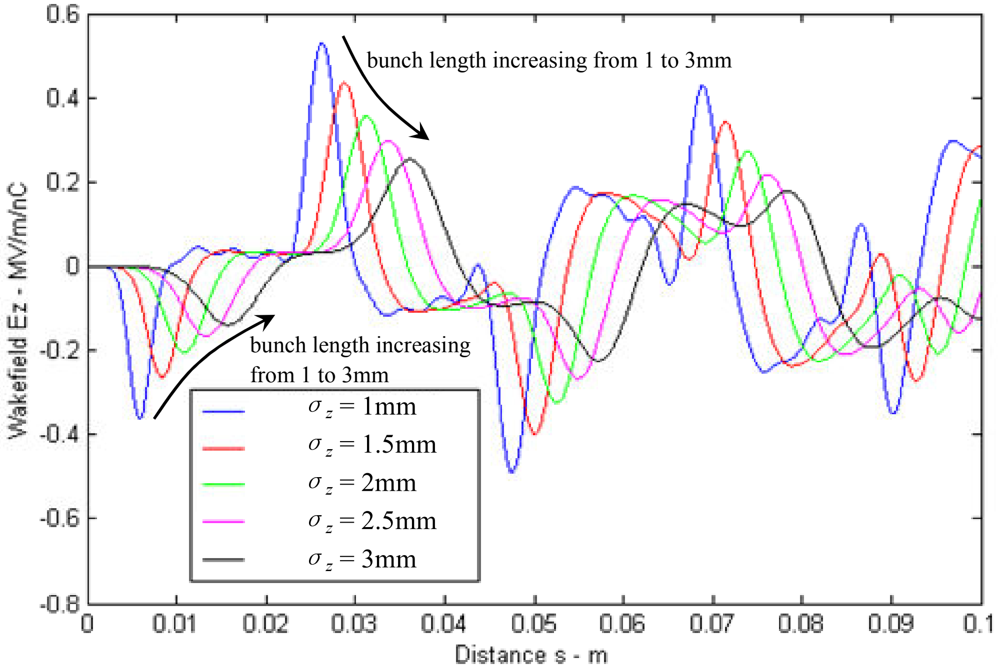

Figure 3.7. The On-axis Longitudinal Wakefield Decreases with Increasing Bunch Length. The bunch charge is 1nC in these calculations.

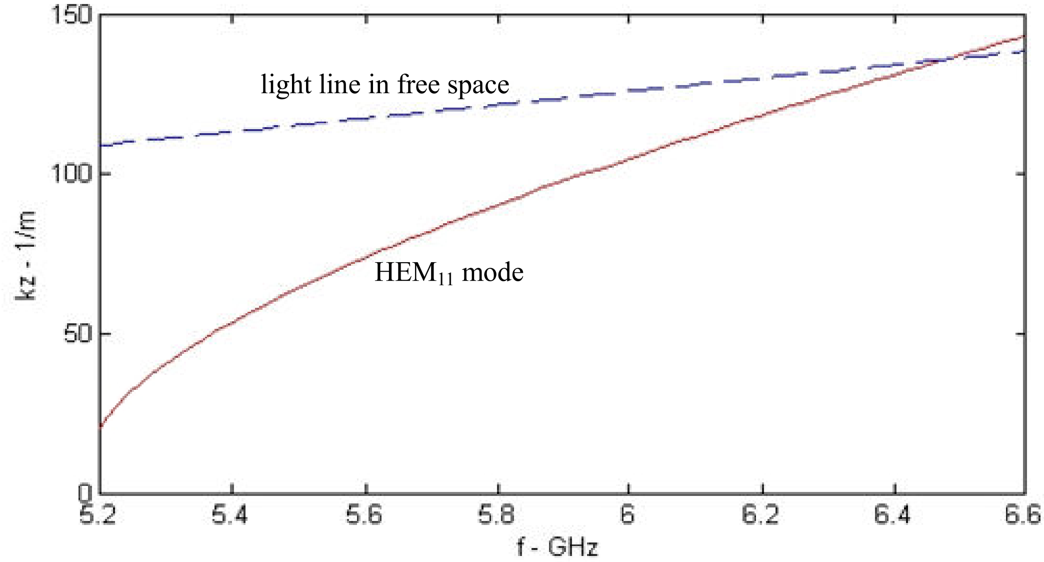

Figure 3.8. Dispersion Curve of the HEM_{11} Mode in the Dielectric-loaded Waveguide.

3.2.1 Modeling and Simulation. The RF coupler was modeled and optimized to achieve efficient coupling with CST Microwave Studio (CST 2003), as shown in Figures 3.9(a) and (b). The downstream end of the dielectric tube is inserted into a larger metallic tube (inner radius *d*) which is connected to a stepped rectangular waveguide for impedance matching. The downstream beam hole through the metallic section has the same radius as the inner radius of the dielectric, *a*, which is below cutoff for the TM_{01} mode at 7.8GHz, and thus no RF can be coupled into the beam hole.

By changing the cylinder length *h*, the cylinder radius *d*, the width of the narrowed waveguide *w*, and the position of the step *g*, the S-parameters of the coupler were tuned to maximize the coupler bandwidth around the center frequency at 7.8GHz, where the computed S_{21} is -0.23dB, while the S_{11} is -12.9dB. From 7.71GHz to 7.94GHz the S_{21} is better than -1dB, and from 7.68GH to 8.06GHz the S_{21} is better than -3dB.

3.2.2 Fabrication and Low-power RF Test. In this section, the fabrication and low-power RF measurement (cold test) of the power extractor assembly, including the decelerator and the RF coupler, are described. Based on the above numerical simulations, the assembly was fabricated at ANL. The outer conductor of the decelerator and the RF coupler housing were both machined out of oxygen-free electronic (OFE) copper.

Before the copper sleeve of the decelerator and the RF coupler housing were brazed together, a standing-wave cavity was built with this copper sleeve and tested to verify machining precision and accuracy of the permittivity. As shown in Figure 3.10, four 2-inch long dielectric tubes are placed inside the copper sleeve and secured with two end plugs whose beam hole is below cutoff for the TM_{01} mode, resulting in a standing-wave structure. Two probes made of coaxial cable are placed on axis inside the beam

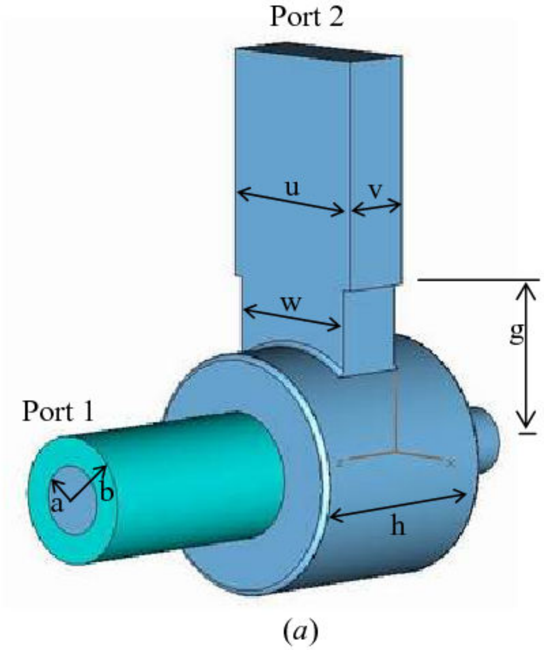

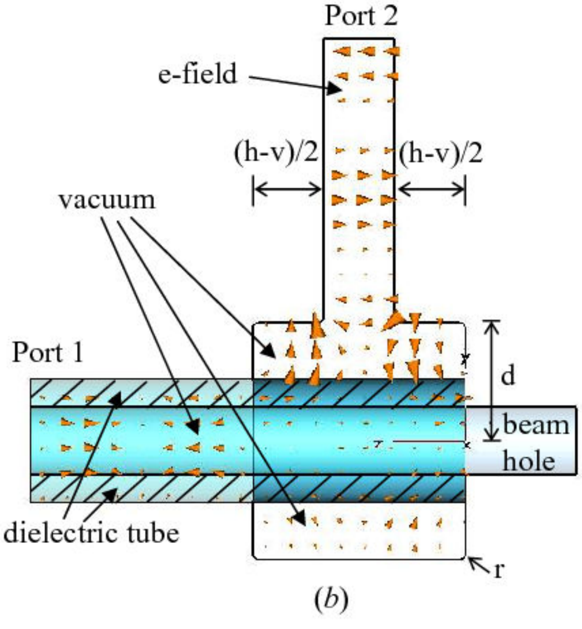

Figure 3.9. CST Microwave Studio Geometry of the TM_{01}-TE_{10} Coupler with the Background Material Satisfying the Perfect-electrical-conductor Boundary Condition. Dimensions are a = 6.02mm, b = 11.17mm, d = 21.30mm, g = 32.43mm, h = 38.32mm, r = 1.00mm, u = 28.50mm, v = 12.62mm, w = 25.00mm. (a) Full view; (b) cutplane.

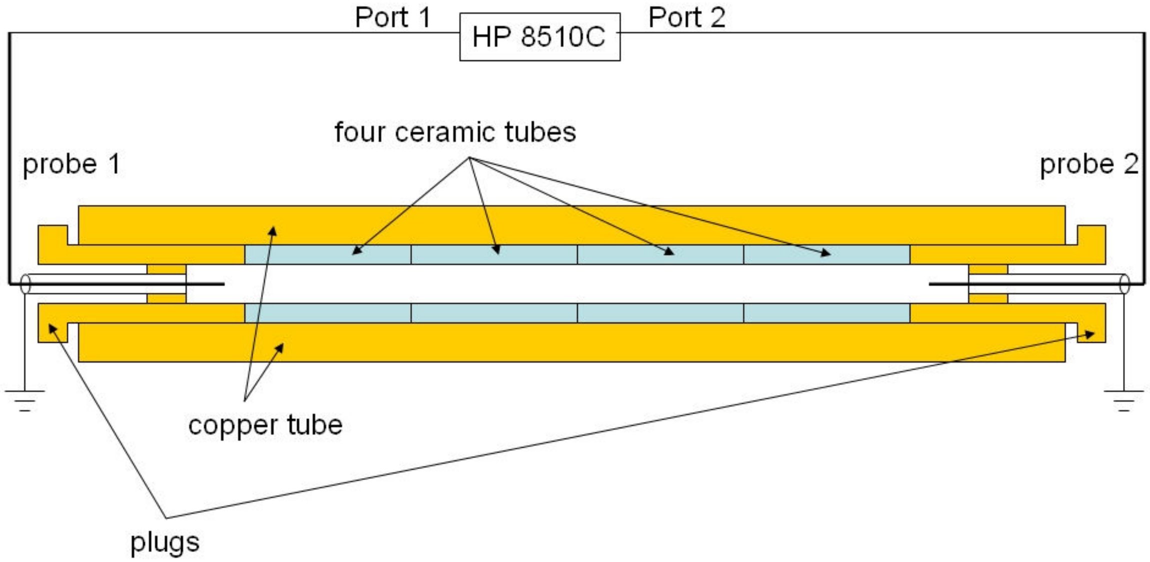

Figure 3.10. A Standing-wave Cavity was Built and Tested to Verify Machining Precision and Permittivity of the Dielectric. It consists of the copper sleeve of the decelerator, four 2-inch long dielectric tubes (ceramic tubes), and two end plugs. The resonant frequencies of the TM_{01n} standing wave modes were measured.

hole of the end plugs, and they are weakly coupled to the standing-wave modes inside the cavity (<-25dB). Since the two probes are on axis, they can only sense azimuthally symmetric standing-wave modes such as TM_{0mn} modes. The weak coupling makes disturbance of the probes on the cavity modes negligible. Figure 3.11 shows the measured resonant frequencies of the TM_{01n} ($n = 1, 2, \ldots 7$) modes compared with the simulated values, where good agreement is found. By doing this we verified that the machining is precise and the nominal value of the permittivity is accurate.

The copper sleeve and the RF coupler housing, along with the WR112 output rectangular waveguide and 3-3/8" stainless steel flanges (A&N Co., part No. 338-000-ANL) were then brazed together at the Advanced Photon Source (APS) machine shop. The fabricated structure is shown in Figure 3.12, and the configuration used for the low-power RF measurements of the power extractor is shown in Figure 3.13(a) and (b). A TEM-TM_{01} mode launcher was designed to convert the TEM mode to the TM_{01} mode for the dielectric loaded waveguide. This is needed to couple the RF power from the HP8510C network analyzer, through the coax line, and into the dielectric-loaded waveguide. The mode launcher consists of a center pin with a disc on the tip, and a grounded copper plug inserted into the copper sleeve. The diameter of the disc, *dp*, is 3.24mm, the thickness of the disc, *tp*, is 2mm, and the distance between the disc and the grounded plug, *gp*, is 4.67mm. The simulated S_{21} of this mode launcher is -0.036dB at 7.8GHz. It is better than -0.1dB in the range between 7.57GHz and 8.06GHz, and better than -1dB in the range between 7.36GHz and 8.41GHz. For comparison, the simulated S_{21} of the RF output coupler (described in Section 3.2.1) is -0.23dB at 7.8GHz, and better than -1dB in the range between 7.71GHz and 7.94GHz. It can be seen the bandwidth of

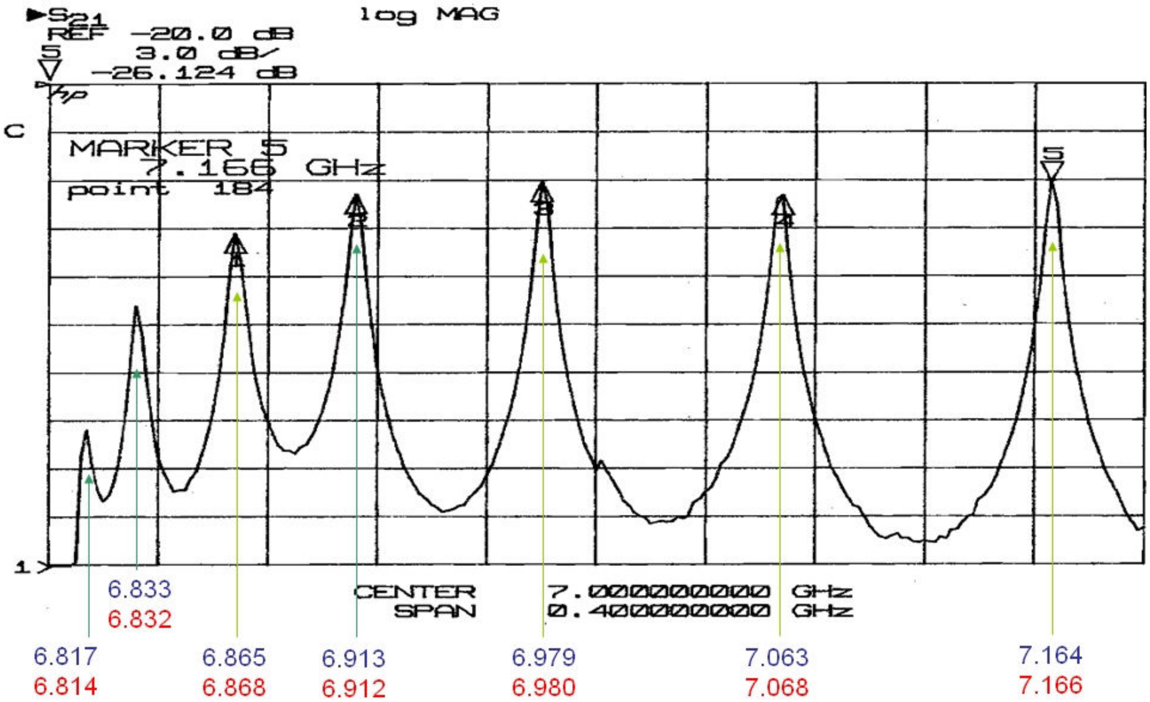

Figure 3.11. Simulated and Measured Resonant Frequencies of the TM_{01n} Modes inside the Standing-wave Structure. $n = 1, 2, \ldots 7$. The numbers indicated below each peak are the simulated (top) and measured (bottom) values.

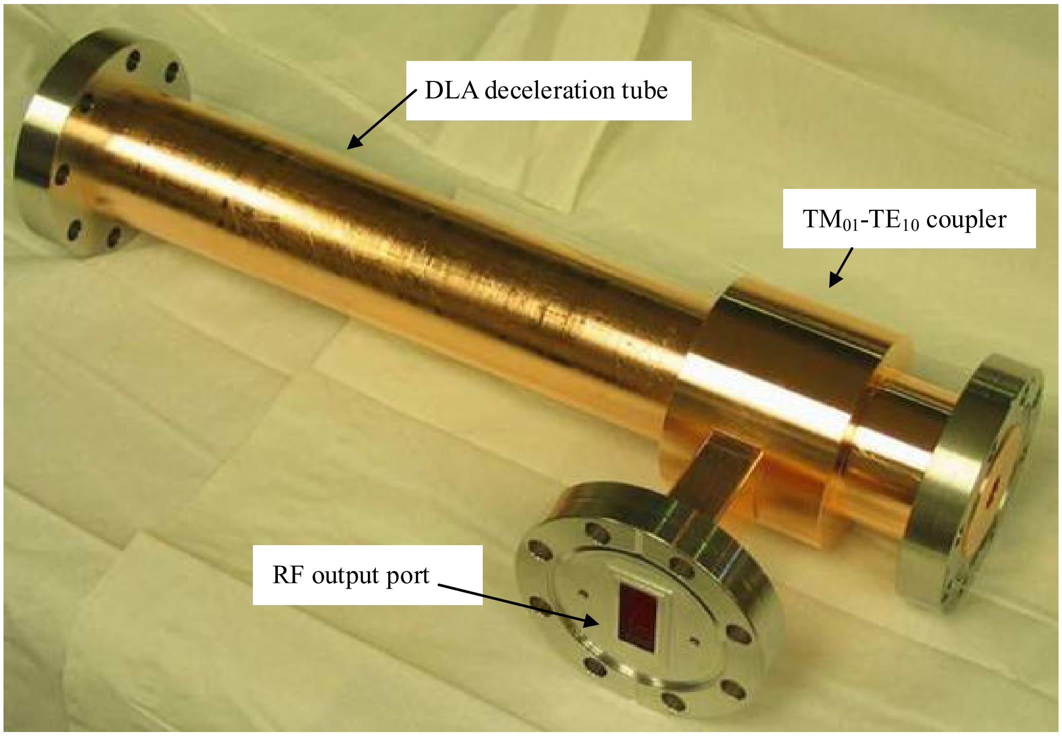

Figure 3.12. The Power Extractor Assembly including the Dielectric-loaded Waveguide and the TM_{01}-TE_{10} RF Output Coupler.

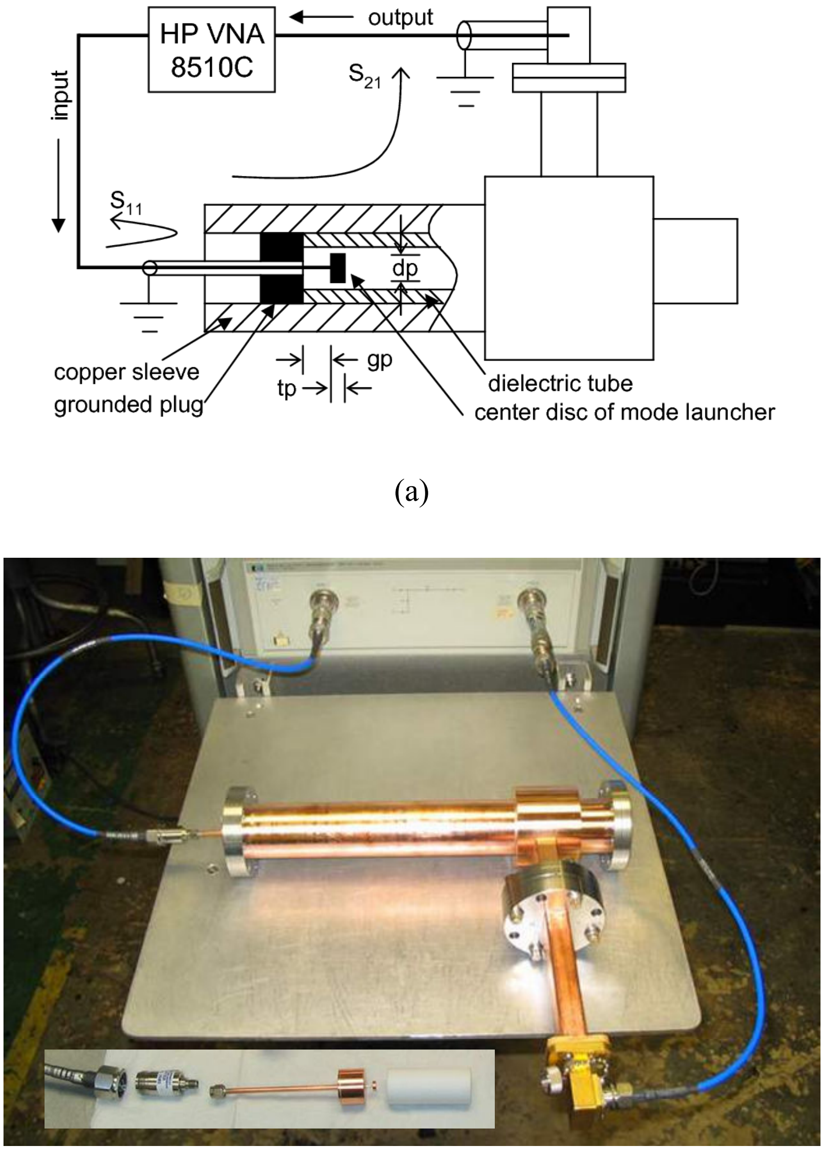

(a)

(b)

Figure 3.13. Setup Used for the RF Bench Measurement of the Power Extractor. (a) The diagram shows a homemade mode launcher (*dp* = 3.24mm, *tp* = 2mm, *gp* = 4.67mm) coupling power into the dielectric loaded waveguide, then through the TM_{01}-TE_{10} coupler and into a commercial waveguide-to-coax adapter. (b) Photo of the actual setup. Inset: from left to right: coaxial cable, N-to-3.5mm adaptor, the mode launcher, a 2-inch section of the ceramic tube.

the mode launcher is much wider than that of the RF output coupler, thus the insertion loss of the mode launcher is negligible. At the output side, a commercial WR112 waveguide-coax adapter (Space Machine & Engineering Co., part No. WCA112.B5MF.CN) is used to convert the TE_{10} mode to the TEM mode for the output cable. Only two 2-inch dielectric tubes were used in the measurement, where the distance between the tip of the mode launcher and the end of the decelerator (same as the entrance of the output coupler) is only 66.6mm, thus the loss due to the DL waveguide is negligible.

The S-parameters of the combined mode-launcher and power-extractor system were measured and simulated; results (Figure 3.14) show good agreement. Figure 3.14(a) shows that the system has a measured insertion loss S_{21} = -0.41dB at 7.8GHz, corresponding to a power coupling efficiency 91%. Figure 3.14(a) also shows that from 7.69GHz to 7.96GHz S_{21} is better than -1dB, and from 7.67GH to 7.99GHz S_{21} is better than -3dB. The measured S_{11} is better than the simulated value, and the small peak at 7.77GHz may be due to the fact the dielectric tube is not perfectly aligned with the axis. The peak at 7.65GHz in Figure 3.14(a) is due to a resonance inside the metallic cylinder (inner radius *d*) in Figure 3.9(b). To increase the bandwidth, adding a tapered section to the dielectric loaded waveguide would help at the expense of increasing the length. However, when longer RF pulses are generated (>10ns), this bandwidth is not a critical limitation anymore.

3.3 Design of the 7.8GHz Bidirectional Coupler and the High-vacuum Flange-gasket Set

To measure the power flow in the output WR112 waveguide, a bidirectional coupler, or at least a coupler with a small coupling coefficient is needed, which should be

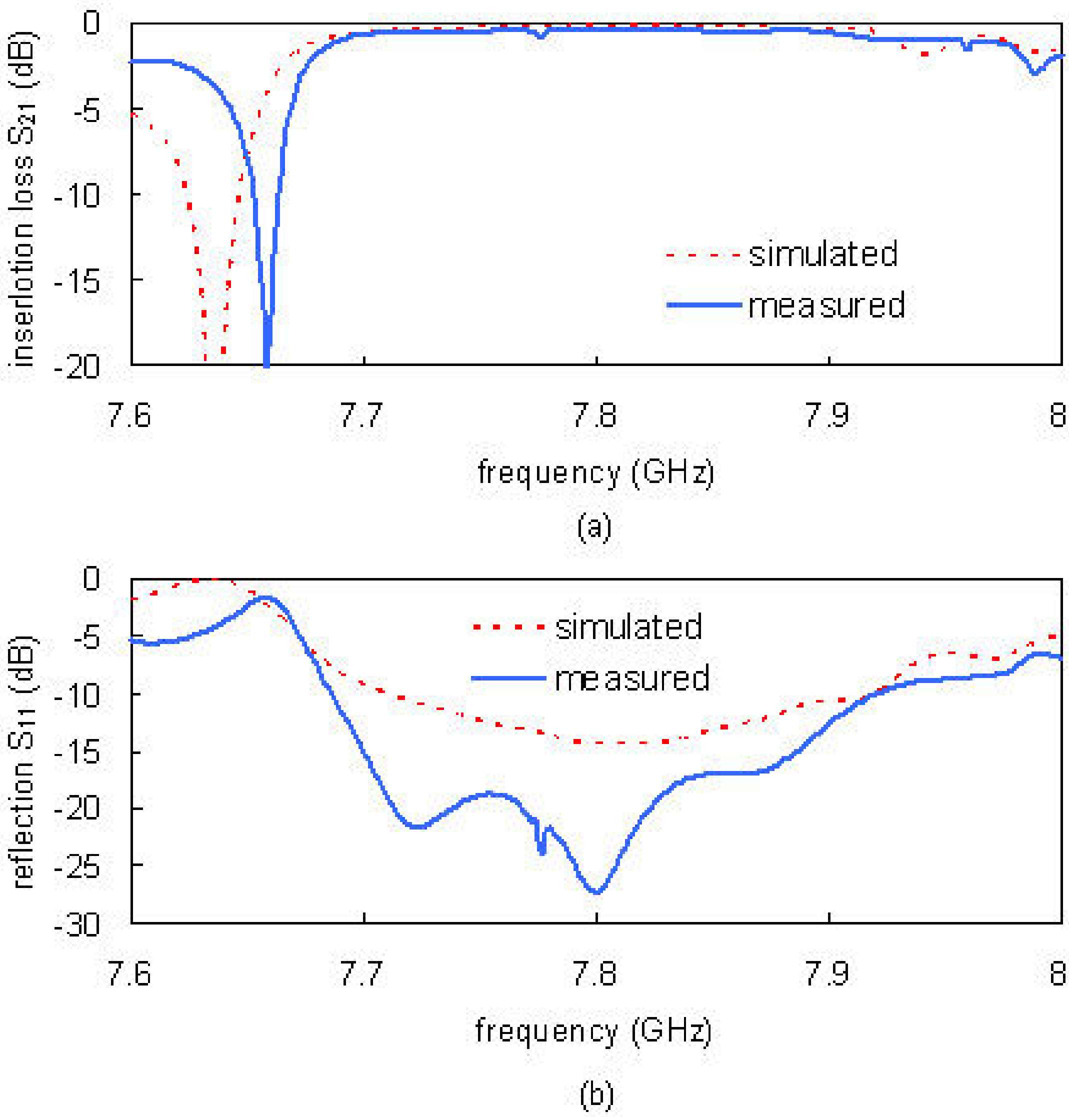

Figure 3.14. Comparison of the Measured and Simulated Transmission S_{21} and Reflection S_{11} Coefficients. The assembly under test consists of the mode launcher and the RF output coupler: (a) insertion loss S_{21}; (b) reflection S_{11}.

able to provide proper RF coupling while maintaining the high vacuum inside. In the AWA program, such a probe-based weak coupler was used in monitoring whether a breakdown occurs in standing-wave dielectric tubes when a high charge is passing through, and another loop-based coupler was used to monitor the RF field in the gun (Conde 2006).

As shown in Figure 3.15, a bidirectional coupler for the 7.8GHz high power signal was designed. The main waveguide, through which the high power RF signal propagates, has two waveguide ports. The coupling has two coaxial ports for the weak RF signal. On the wall between the two waveguides, there are five equidistant round holes with different sizes to provide forward coupling and backward isolation. The coupling and isolation coefficients were simulated with CST Microwave Studio. At 7.8GHz the forward coupling is -64.3dB, backward isolation -87.2 dB, and directivity 23dB. Figure 3.16 shows the parts for the bidirectional coupler before final brazing.

The 7.8GHz bidirectional coupler was also tested with the HP-8510C network analyzer. The comparison between measurement and simulation is given in Figure 3.17(a) and (b). At 7.8GHz, the measured coupling is -64.6dB, which is slightly lower than the simulated value -64.3dB. However, the measured curve is less flat than the simulated one, because the coaxial feed-throughs used in the bidirectional coupler are frequency sensitive, while in the simulation the feed-throughs are ideal. Accordingly, the isolation is not as good as the simulated case, and the directivity at 7.8GHz dropped to 7.9dB.

For the joints on the WR112 output rectangular waveguide, a special 7.8GHz flange-gasket set has also been designed to maintain RF continuity while also holding high vacuum during beam tests. As shown in Figure 3.18, a waveguide hole was machined out of a 3-3/8” stainless steel blank flange. Around the waveguide hole, a step was used to compress the annealed copper gasket for good electrical contact so that the RF signal will not be distorted. The knife-edge on the flange is used to bite into the gasket for a high vacuum seal. Furthermore, since the rectangular waveguide is not rotationally symmetric, two holes (not through) on the flange and two through holes on the gasket are used for alignment. Since the region between the inner electrical contact and the outer knife-edge seal may cause a virtual vacuum leak, two cuts on the gasket are made for air conduction from this region to the waveguide hole. The two cuts are made at the corner of the waveguide hole where the electric field is a minimum, to avoid possible high power breakdown.

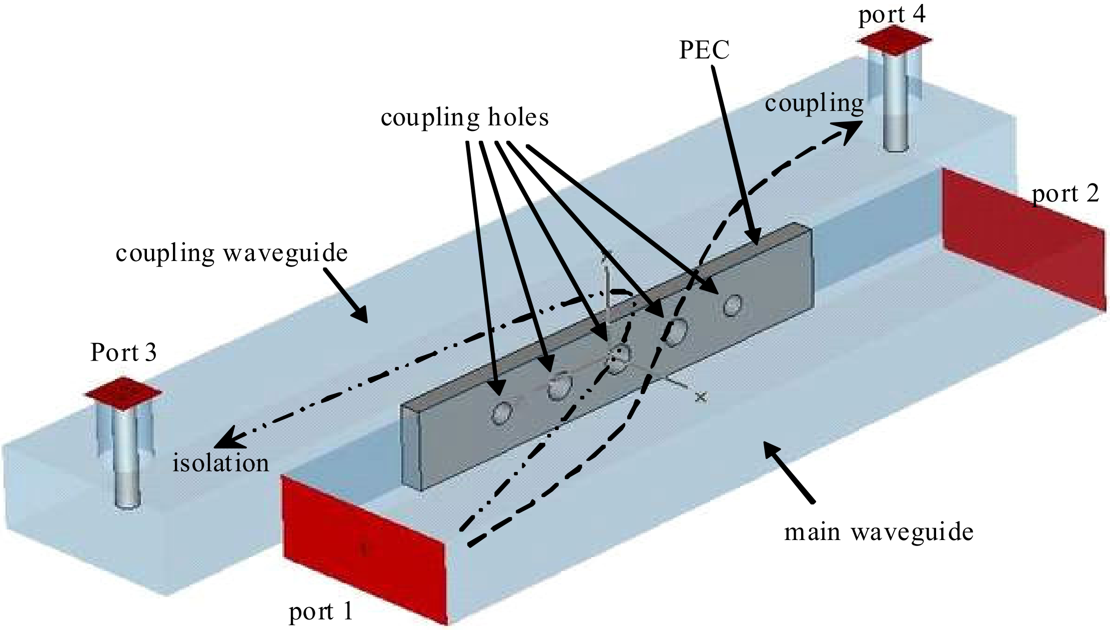

Figure 3.15. CST Microwave Studio Geometry of the Bidirectional Coupler.

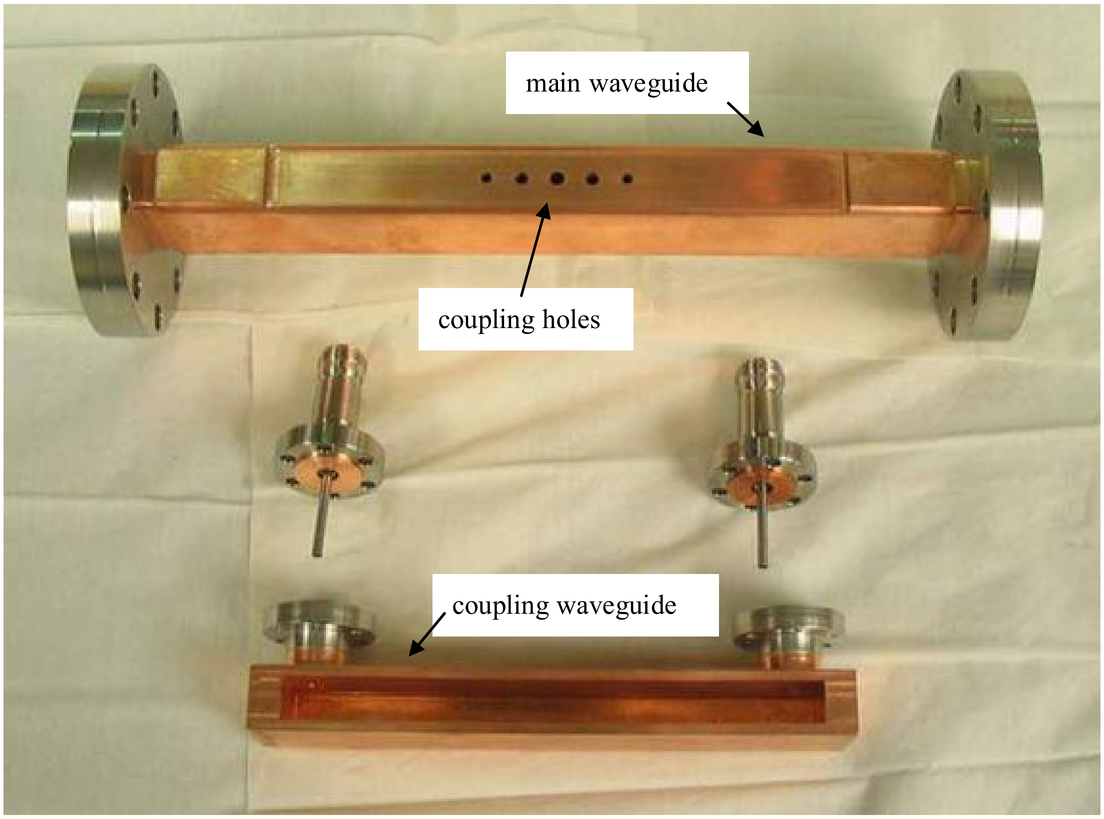

Figure 3.16. Parts for the Bidirectional Coupler Before Brazing.

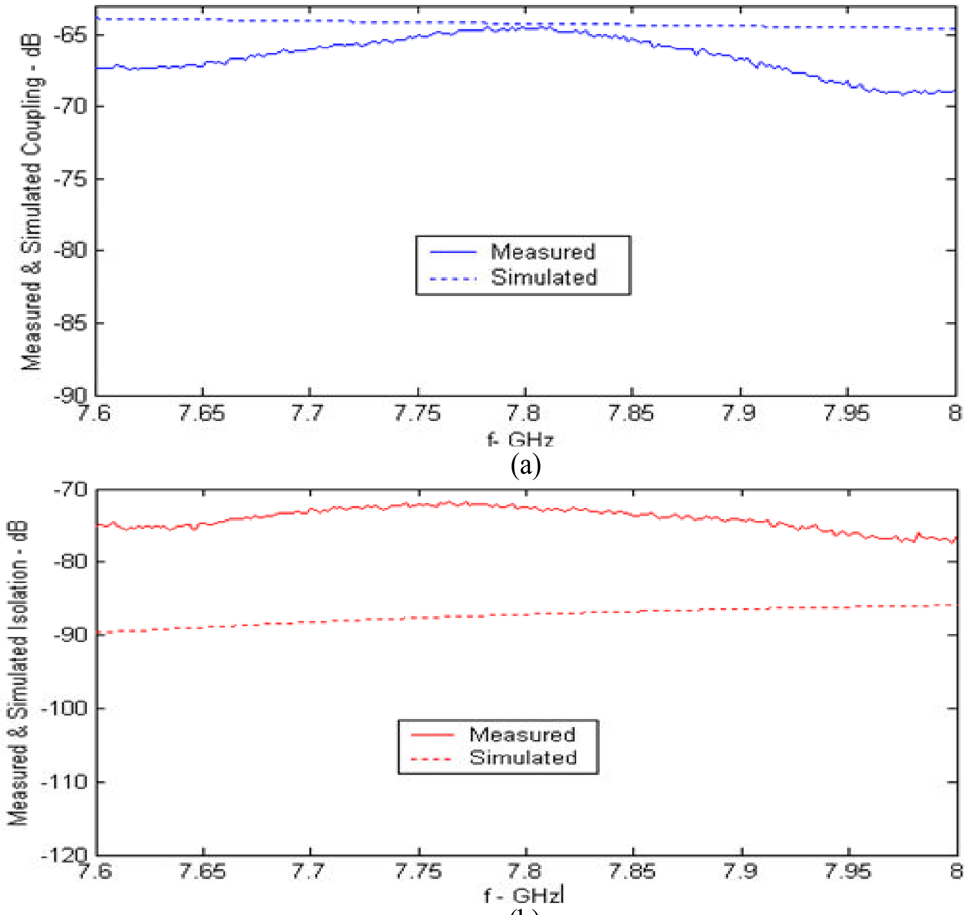

(a)

(b)

Figure 3.17. Measured and Simulated Coupling (a) and Isolation (b).

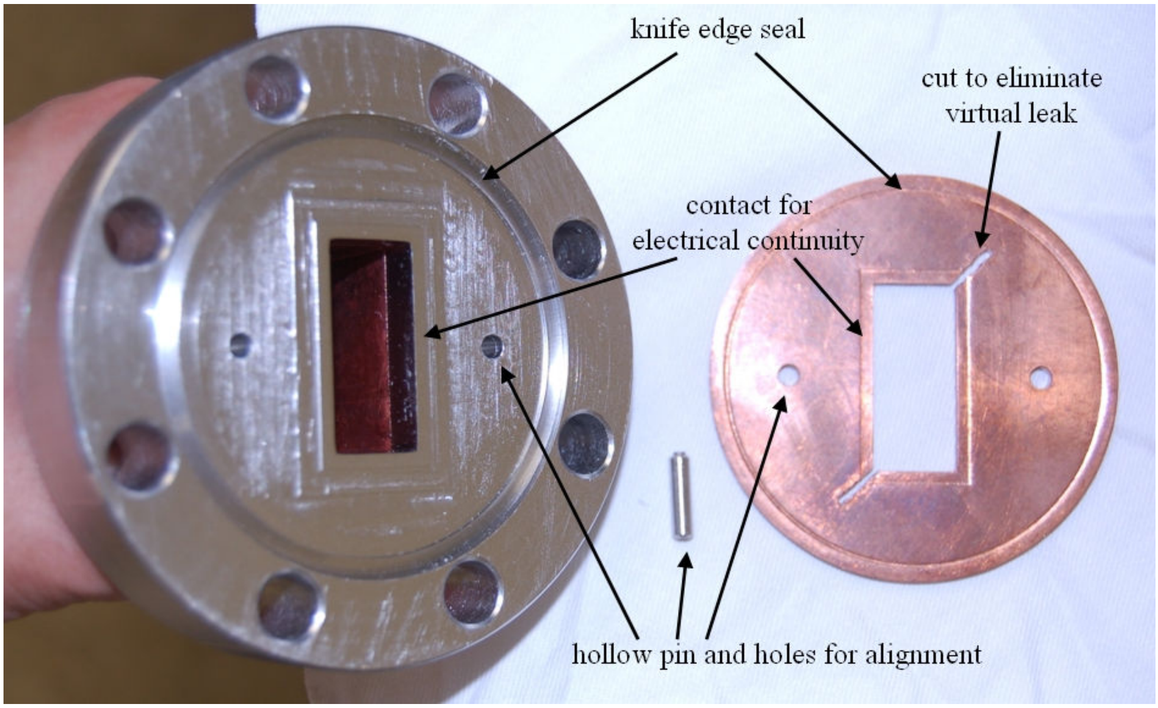

Figure 3.18. A high-vacuum 3-3/8” Flange and a Used Gasket.

CHAPTER 4

IMPLEMENTATION OF EXPERIMENT

The AWA is located at the Argonne National Laboratory, and its research focuses upon the physics and technology of advanced methods to accelerate charged particles. The goal is to identify and to develop techniques which may lead to more efficient, compact, and inexpensive particle accelerators. The AWA facility is supported by the United States Department of Energy, High Energy Physics Division, and is specifically designed for accelerator research that requires intense, short pulse electron beams.

4.1 Introduction to AWA Facility

As shown in Figure 4.1, the AWA facility consists of a control room, a laser room, and a concrete tunnel (AWA 2008). The interface with which operators and users control the beamline is located in the control room, and the UV laser system used for electron generation is located in the laser room. In the tunnel there had been three electron beamlines: the drive gun beamline, the witness beamline and the test stand beamline.

The drive gun beamline and the witness beamline were used to investigate interactions between a drive beam and a witness beam through the wakefields generated by the drive beam. The two beams were either collinear or parallel, which means the witness beam was influenced either directly by the wakefield of the drive beam in the same structure, or by the extracted and transported power of the wakefield excited by the drive beam. These two configurations made it possible to study the characteristics of an accelerating structure, such as probing the wakefield in the DL waveguide (Schoessow 1998), and the prototype TBA with DL waveguides (Conde 1999). Although the technology used was groundbreaking for its time, only modest accelerating gradients

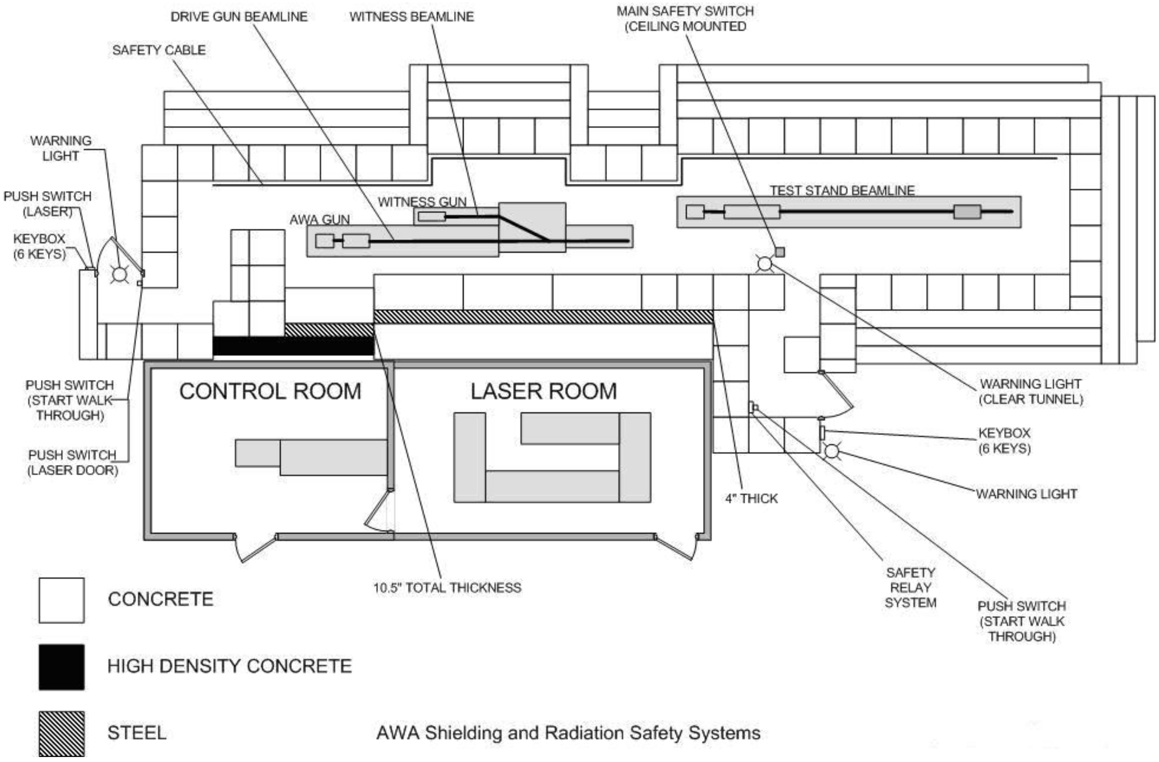

Figure 4.1. AWA Facility View.

were achieved with these two beamlines. The record-breaking >100nC/pulse generated by the drive linac could not entirely offset the 20-40ps FWHM length of the electron bunches, and the >1000 π mm-mrad transverse emittance. Advances in photoinjector technology have led to the development and construction of the new test stand beamline (Conde 2007).

4.1.1 The Test Stand Beamline. As shown in Figure 4.2, the test stand beamline consists of an electron gun with a magnesium photocathode, a linac and beam diagnostic components. (The beamline takes its name from its original use as a gun test fixture.) Both the gun and the linac operate at 1.3GHz, fed by a 30MW klystron. The one-and-a-half cell gun runs with 12MW of input power, and the accelerating gradient at the cathode surface reaches 80MV/m. Once the electrons are generated on the cathode surface by a UV laser pulse, they are accelerated to 8MeV by the high gradient RF field and pushed out of the gun. Figure 4.3 shows the improvement of the new gun in the test stand beamline compared to the old AWA gun, where with the new gun 2mm bunch length is achieved even under high charge condition. The linac runs with 18MW of input power and accelerates electron bunches from 8MeV to 15MeV. The charge of electron bunches can be easily varied from 1 to 100nC, with bunch lengths of 2 to 8ps, with emittances in the range from 5 to 200 π mm-mrad.

In Figure 4.2, along the test stand beamline, integral current transformers (ICTs) are used: ICT1 is used to monitor the charge coming out from the gun, while ICT2 is used to monitor the charge that passes through the device under test (DUT). After ICT1, a cross chamber with three quartz windows (two at both sides and one on the top) is used for UV laser input; inside the chamber UV pulses are reflected onto the photocathode

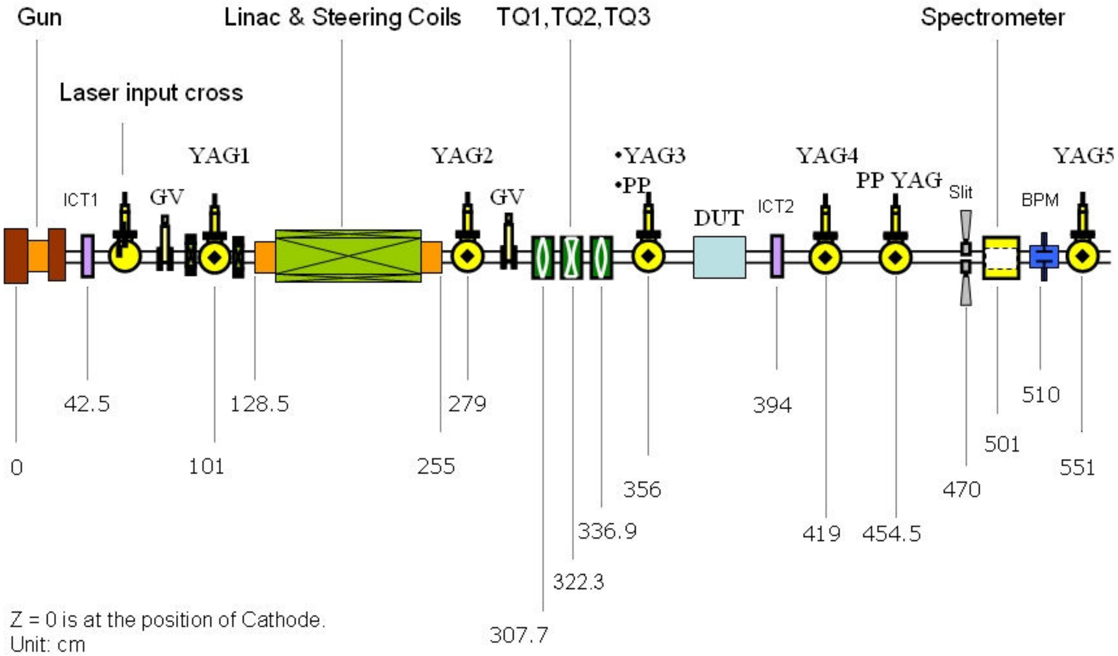

Figure 4.2. A View of the AWA Test Stand Beamline.

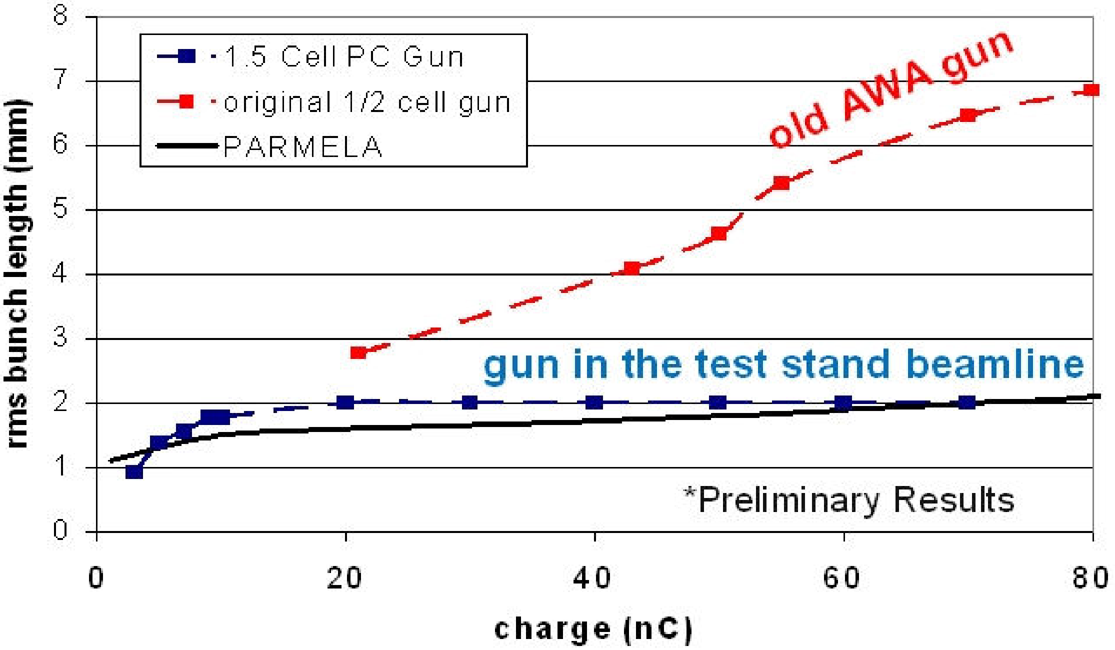

Figure 4.3. A Shorter Bunch Length is Achieved in the New Gun in the Test Stand Beamline. The bunch length is compared to that from the old AWA gun. Differing from the PARMELA simulation, the bunch length become fairly constant when the bunch charge is higher than 20nC.

surface by UV mirrors. Two gate valves (GVs) are used to separate vacuum regions of the gun, the linac and the downstream region during installation and pumping. YAG (Yttrium Aluminum Garnet) screens, shown as YAG1 through YAG5, are used to monitor the transverse position of the electron beam. A pepper pot plate (PP) and a pepper pot YAG (PP YAG) can be used for study of beam dynamics and diagnostics, together with the aforementioned YAGs. Steering and trimming coils (not shown in the figure) are used for adjusting beam position, and quadruple magnets (TQ1 through TQ3) for adjusting beam focusing. After PP YAG, a beam energy spectrometer and its slit are placed. The slit consists of a pair of micrometers and can be adjusted from 0.3 to 50.8mm. A beam position monitor (BPM) is located after the spectrometer and is sometimes used for low charge beam monitoring.

4.1.2 The AWA Laser System. The AWA laser system is shown in Figure 4.4. It consists of a Tsunami oscillator purchased from Spectra Physics and a TSA-50 chirped-pulse amplifier (CPA) from Positive Light. The oscillator is a regenerative mode-locking Ti:Sapphire oscillator tuned to $\lambda = 744$nm ($\Delta\lambda = 9$nm, $E = 7$nJ) output that is pumped by an all solid-state 5W, CW green laser (Millennia V). The oscillator runs at the 16th sub-harmonic (81.25MHz) of the RF (1.3GHz) and is phase locked to within 1ps (rms jitter) of the RF using the vendor's *Lok-to-Clock* box. The CPA consists of a stretcher followed by a Ti:Sapphire regenerative amplifier (ReGen), two stages of linear Ti:sapphire amplifiers and a compressor. After reducing the bandwidth with a mask in the stretcher, the seed pulse exits the stretcher with a pulse length of approximately 200ps where it is optically switched into the ReGen with the injection Pockels Cell, at a repetition rate of 10Hz. The extraction Pockels Cell timing is adjusted to extract the most stable pulse

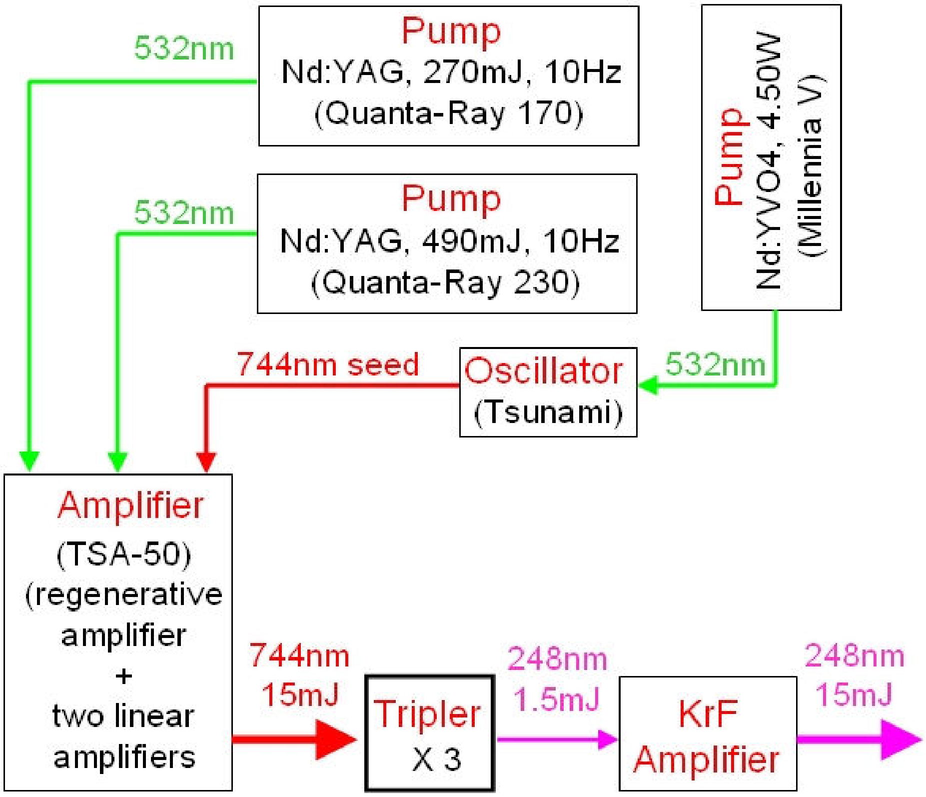

Figure 4.4. The AWA Laser System.

from the ReGen and this pulse (E = 2.5mJ) is then further amplified by the two linear amplifiers to 35mJ and directed into the compressor. Upon exiting the compressor the pulse energy is 15mJ and the pulse length is 8ps FWHM. After exiting the CPA, this pulse is frequency tripled to λ = 248nm (UV) and E = 1 - 2mJ, in the Tripler. The UV pulse is then amplified to 15mJ by a KrF amplifier. After exiting the KrF amplifier, the laser pulse passes through a variable telescope and is then transported by a series of mirrors into the accelerator tunnel. In the beamline, the laser pulse can either be used as a single pulse to generate a single electron bunch, or split into trains of micropulses to generate electron bunch trains.

4.2 Setup for Beam Tests

The power extractor was installed in the DUT section of the beamline in Figure 4.2. Figure 4.5 shows a simplified diagram of the installation, and Figure 4.6 gives the photo of the power extractor in the beamline. As shown in Figure 4.5, the electron beam travels through the decelerator part, and an RF wakefield is excited by the beam at the same time. The beam then exits the decelerator and passes through an ICT, where its charge is measured. The energy spectrum of the decelerated beam is monitored by a spectrometer. At the same time, the RF wakefield is coupled into the WR112 rectangular waveguide through the RF output coupler. Then the RF signal goes through the bidirectional coupler, where the forward and backward signals are coupled to and measured with a Tektronix TDS6154C 15GHz oscilloscope (sampling rate: 40GHz). Ideally after the bidirectional coupler a high power (thus high vacuum) load should be used to absorb the RF pulse so that the forward signal would not be mixed with the reflected signal. However, since such a load is not commercially available at 7.8GHz,

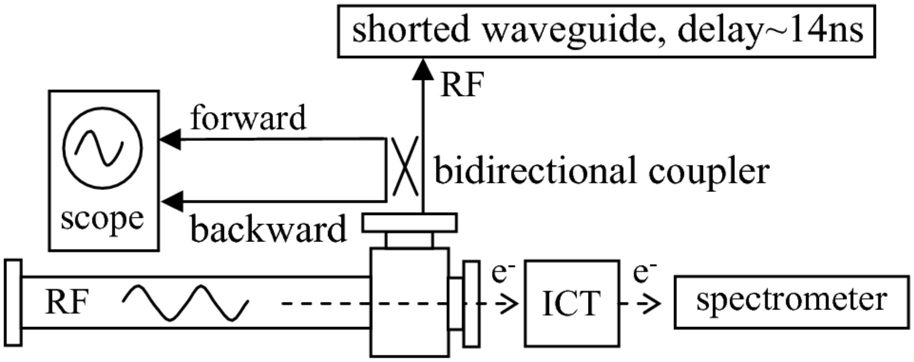

Figure 4.5. Experimental Setup for RF Power and Beam Charge Measurements.

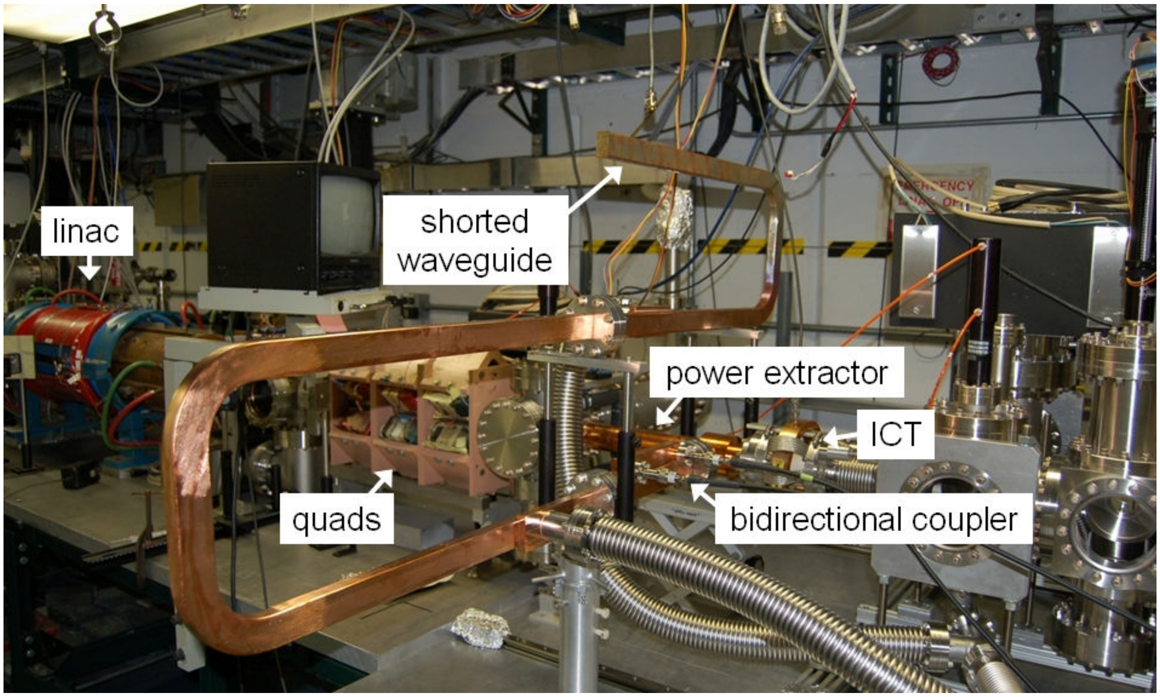

Figure 4.6. Power Extractor Installed in the Beamline.

a 1.4m shorted WR112 waveguide is used to provide ~14ns delay of the reflected signal for the single bunch test. During bunch train tests, since the RF signal is much longer, in order to distinguish the forward signal from the backward, the shorted waveguide has been extended to provide ~28ns delay of the reflected signal. On this shorted waveguide extra vacuum ports have also been made to help pumping.

For single bunch tests, generation of a single electron bunch is shown in Figure 4.7. The output UV laser pulse, shown in Figure 4.4, is sent into the beamline tunnel, then into the vacuum cross chamber through a window. Inside the chamber, there are two side mirrors behind the windows, and a third mirror on the top (not shown in the figure). The side mirrors are used to reflect UV laser beams onto the cathode, and the top one is used to reflect the cathode image to a laser camera for adjusting the laser spot on the cathode. In the single bunch test, only one side mirror is used. The reflected UV laser pulse from this mirror strikes the center of the cathode, and generates a single electron bunch. This electron bunch is then accelerated to 8MeV in the gun by the 1.3GHz RF power provided by the klystron. After exiting the gun, the bunch travels to the linac and is further accelerated to 15MeV for beam tests.

Generation of an electron bunch train is more complicated. It involves splitting the UV laser pulse into two trains of micropulses spaced by 2*T*, twice the period at 1.3GHz, and recombining the two trains with different relative delays for different 7.8GHz RF pulse lengths. The following two subsections will describe the splitting/combining process in detail (Gao 2009).

4.2.1 Splitting the UV Laser Pulse into Two Trains of Micropulses. Figure 4.8 shows a beam splitting setup for generation of the two micropulse trains. It consists of a

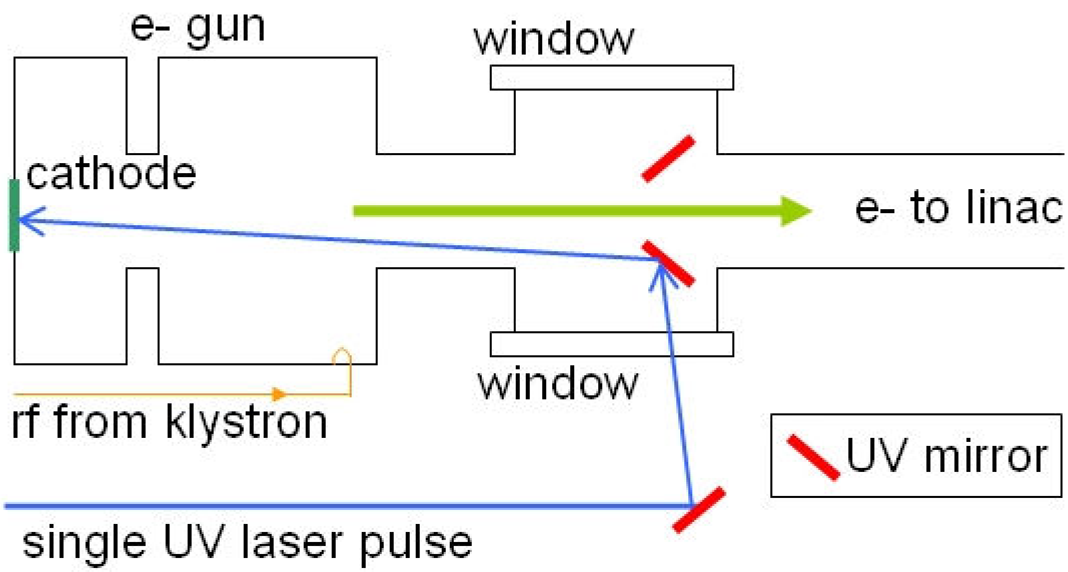

Figure 4.7. Generation of Single Electron Bunches.

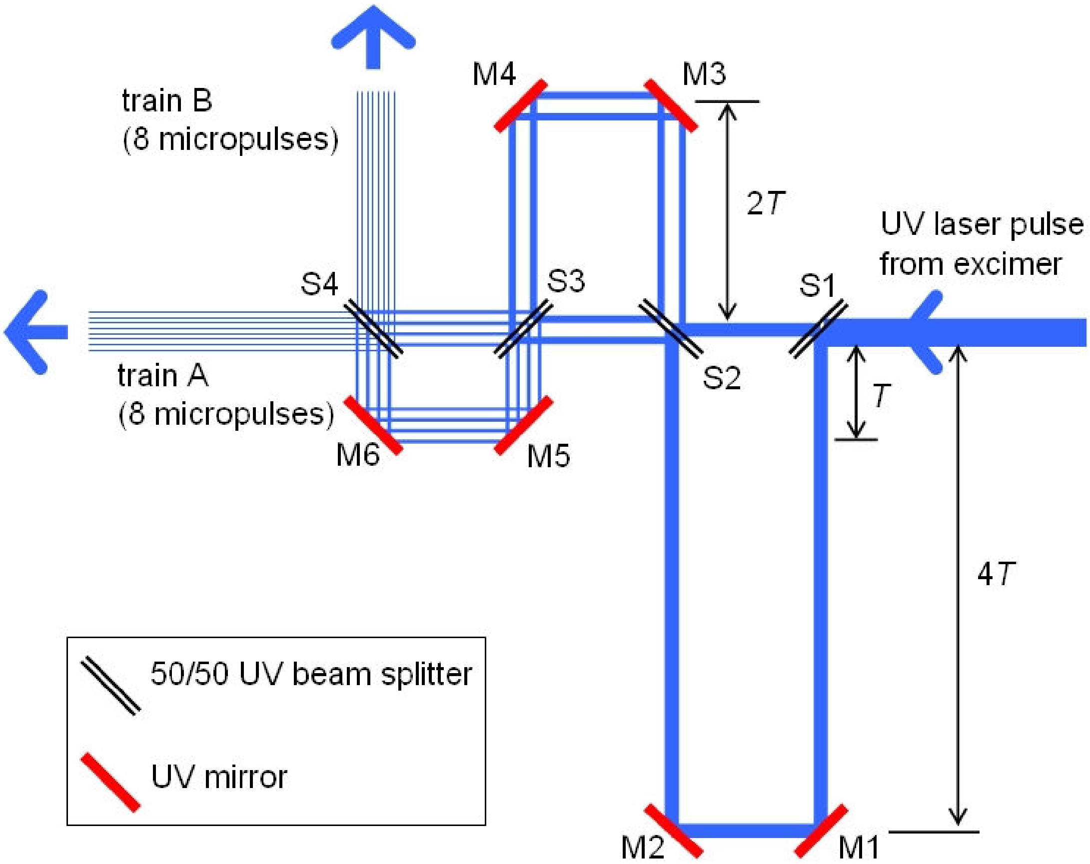

Figure 4.8. A Single UV Laser Pulse is Split into Two Trains of Micropulses. Each train consists of eight micropulses spaced by 2*T*, twice the period at 1.3GHz, the fundamental frequency of the electron gun and linac. Collinear laser beams are offset for display purposes.

series of 50/50 beam splitters labeled S1 - S4, and a series of UV mirrors labeled M1 - M6. The beam width in the figure represents intensity, and all collinear beams are offset for display purpose. This splitter has three arms to provide different delays for micropulses. The first arm with M1 and M2 gives a total delay (round-trip) of $8T$, the second arm with M3 and M4 gives a total delay of $4T$, and the third arm with M5 and M6 gives a total delay of $2T$. The incoming UV laser pulse (from the KrF excimer) passes through S1 to S4, the laser beams are split and combined at the four beam splitters, resulting two micropulse trains: train A and train B. Each train has 8 micropulses spaced by $2T$, thus the delays of micropulses with respect to the first one are 0, $2T$, $4T$, …$14T$. From the first micropulse to the last one, they are denoted A1 - A8 in train A, and B1 - B8 in train B.

To ensure the delay of each arm is precisely $2T$, $4T$ or $8T$, each mirror pair is placed on a movable stage equipped with a micrometer. The delay is adjusted so that for each train, the electron bunch generated by each UV micropulse has the same energy at the spectrometer, and therefore should have the same launch phase in the gun and are precisely spaced by integer multiples of T. The procedure is explained below.

To check the energy of each electron bunch, the focusing/defocusing magnets are adjusted so that the electron beam is focused on the screen of the spectrometer. Steering/trimming coils are also used to steer the beam to intercept a 0.3mm slit before the spectrometer. The transmitted portion of the beam is subsequently used for energy monitoring.

First A1 (path: S1-S2-S3-S4) is the only micropulse sent onto the cathode while all others are blocked, and its centroid energy is measured. Then A2 (path: S1-S2-S3-

M5-M6-S4) is the only one in use and the delay of the corresponding arm (with M5-M6) is adjusted in increments of 1mm (~3ps round-trip), to reach the goal that the energy of the electron bunch generated by A2 is closest to that of the one generated by A1 as observed with the spectrometer. Similarly the other two delay arms are adjusted by using A3 and A5, then all the four bunches should have same launch phase. At a later time, all electron bunches generated by the rest of UV micropulses are compared to the bunch generated by A1, and they also have the same energy. Then all 8 electron bunches generated by the 8 micropulses are evenly spaced by $2T$. Figure 4.9 shows the centroid of the beam energy distributions of all 8 electron bunches generated by train A normalized to that of the first bunch, which is generated by A1. The maximum deviation present is 1.5%.

Once the three delay arms are fixed using train A, train B automatically has 8 micropulses evenly spaced by $2T$. To confirm this, the electron bunch generated by each individual micropulse in train B has been checked with the spectrometer. Figure 4.10 shows the centroid beam energy of all 8 electron bunches generated by train B normalized to that of the first bunch, which is generated by B1. It can be seen that the maximum deviation is 0.8%.

A 26GHz photodiode is also used to get a rough understanding of the time structures of the two trains. Although the diode is not sensitive to UV light, a thin piece of paper is placed before it to generate florescence light, which has a broad spectrum and can be detected by the diode. The voltage generated by the diode is recorded with a 6GHz oscilloscope, as shown in Figure 4.11. From the curves it can be seen the micropulses are evenly spaced, although both the diode and the oscilloscope are not fast enough to show

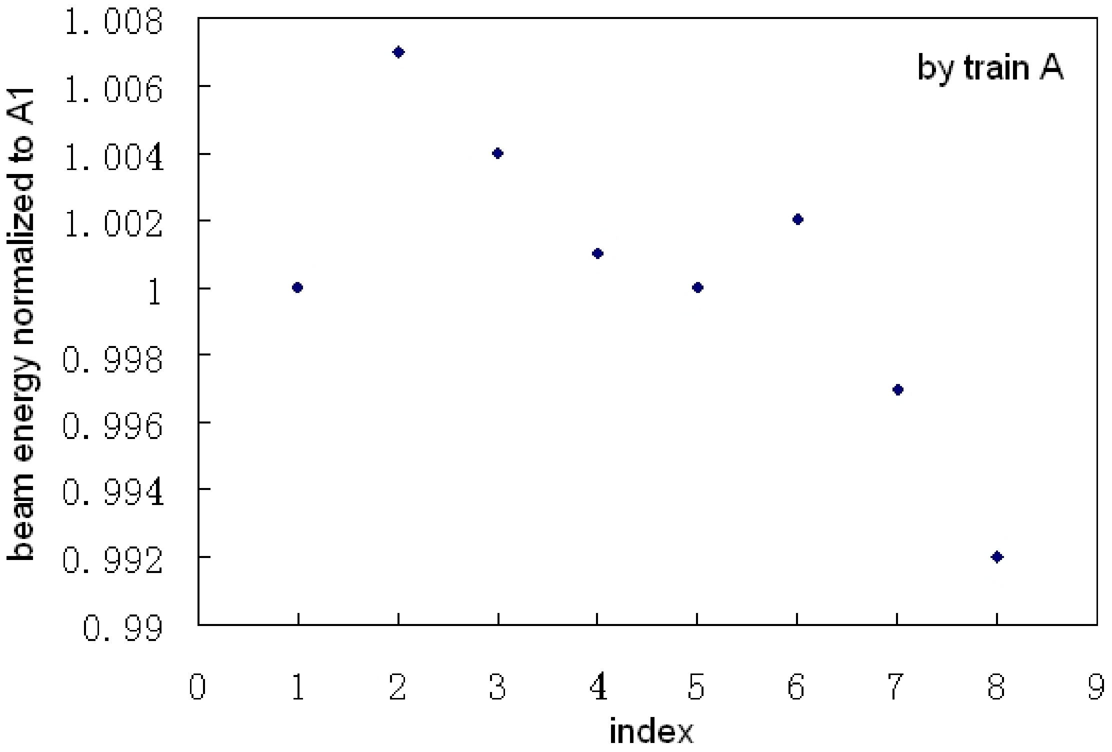

Figure 4.9. Centroid of the Beam Energy Spectrum of the 8 Electron Bunches Normalized to the Beam Energy of the First Electron Bunch in Train A (generated by A1).

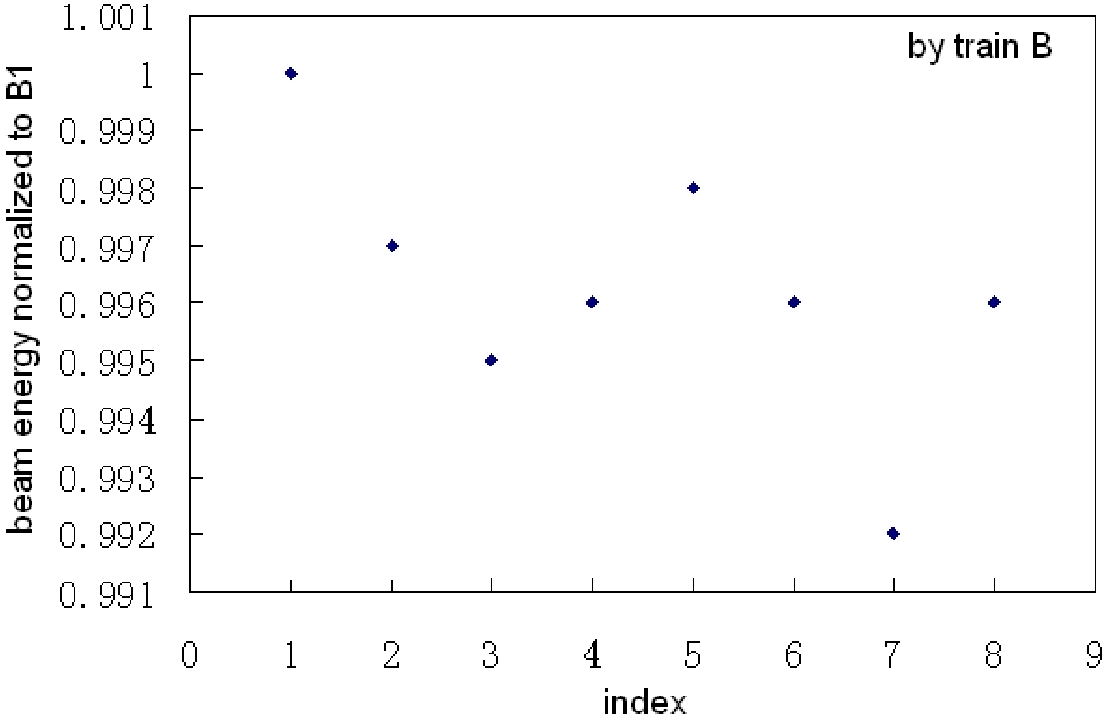

Figure 4.10. Centroid Beam Energy of the 8 Electron Bunches Normalized to the Beam Energy of the First Electron Bunch in Train B (generated by B1).

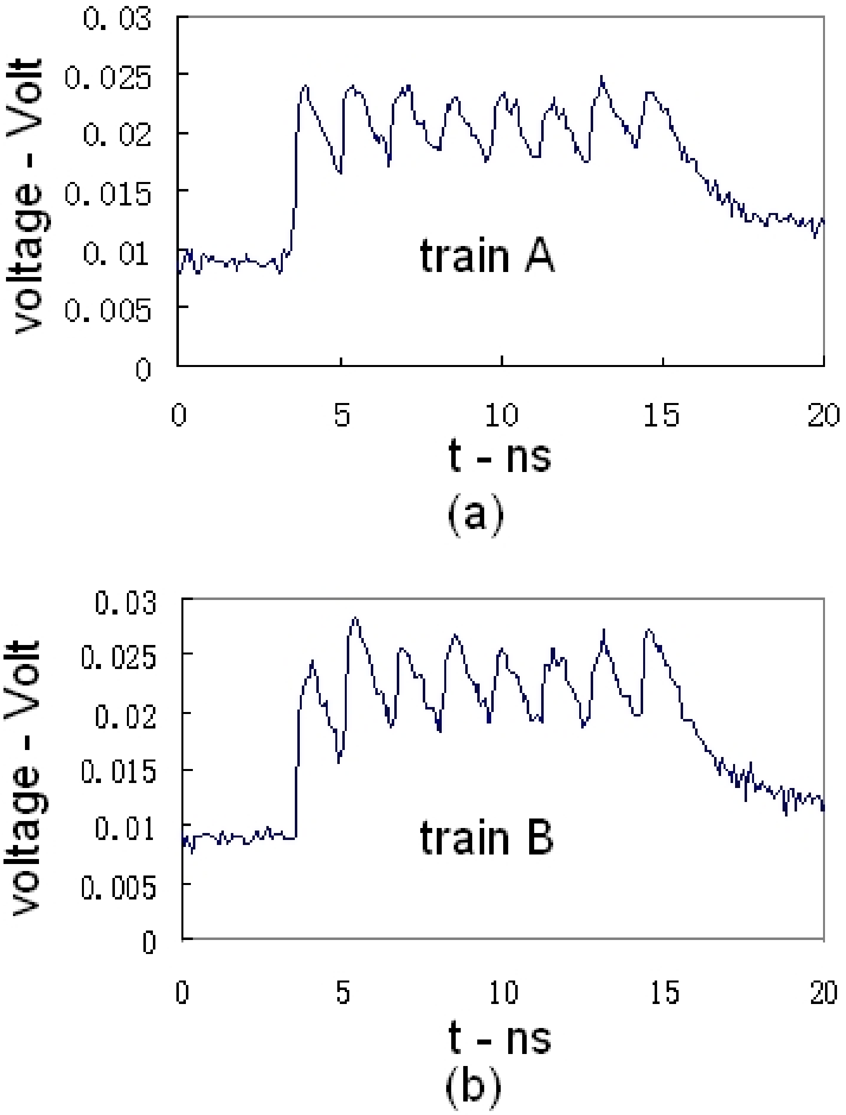

Figure 4.11. Time Structures of Train A (a) and Train B (b) Detected by a Photodiode. The diode is not fast enough to show the separation between micropulses.

the separation between two adjacent micropulses. The two laser micropulse trains are then ready for recombination in the next step.

4.2.2 Generation of Electron Bunch Trains. To generate electron bunch trains, the two trains of UV micropulses, are sent into the cross chamber in the beamline, through two windows at both sides, as shown in Figure 4.12. Train A and train B both hit the center of the photocathode surface. In one of the two laser paths (shown as train A in the figure), a motorized linear stage is used to carry a mirror pair for adjustable beam delay. This motorized linear stage is placed on a manual rail-carrier set. The manual set is used for coarse adjustment, while the motorized linear stage is used for fine adjustment, with a 2-inch round-trip range. When the delay between train A and train B is T, the two trains are interleaved with a spacing of T between two adjacent micropulses. Thus the generated electron bunch train will have 16 bunches with a spacing $T_b = T$, and the total length of the bunch train is $(16\text{-}1)\times T = 12.3$ns. When the delay between train A and train B is $16T$, one train follows the other, with a spacing of $2T$ between two adjacent micropulses. Thus the generated electron bunch train will have 16 bunches with a spacing $T_b = 2T$), and the total length of the bunch train is $(16\text{-}1)\times 2T = 24.6$ns.

Aside from beam energy monitoring, another method is used to ensure the delay between train A and train B is exactly T or $16T$, which means the delay between A1 and B1 is exactly T or $16T$. Figure 4.13 shows a curve of charge generated by the gun, versus the launch phase of the laser pulse with respect to the RF signal in the gun. The 50° launch phase is usually used to obtain small beam emittance. At 120° there is an abrupt drop in charge with increasing launch phase, which means that around this point the abrupt charge change can be used to determine the launch phase. First the first

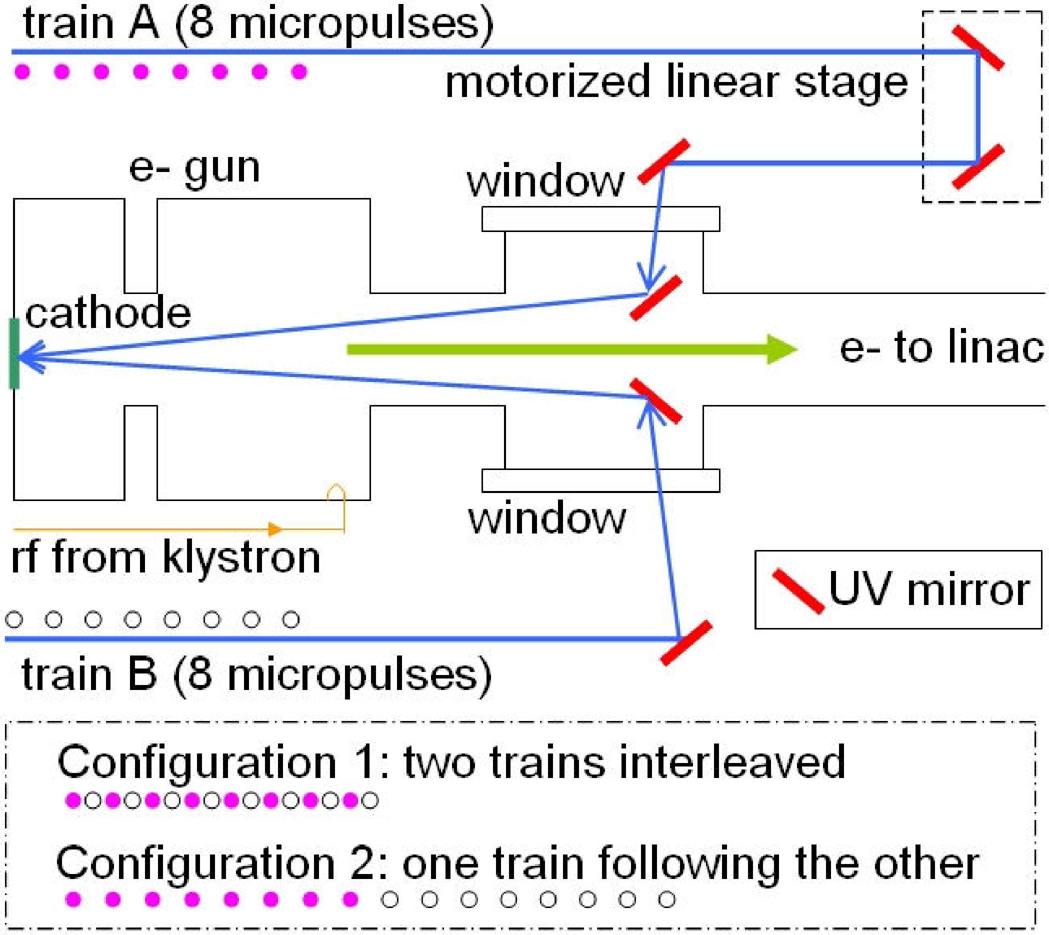

Figure 4.12. During the Bunch Test Two Trains of UV Laser Micropulses are Sent onto the Photocathode through Two Windows. By adjusting the delay between the two trains with a motorized linear stage, two configurations can be achieved to obtain ~10ns and ~20ns electron bunch trains, respectively.

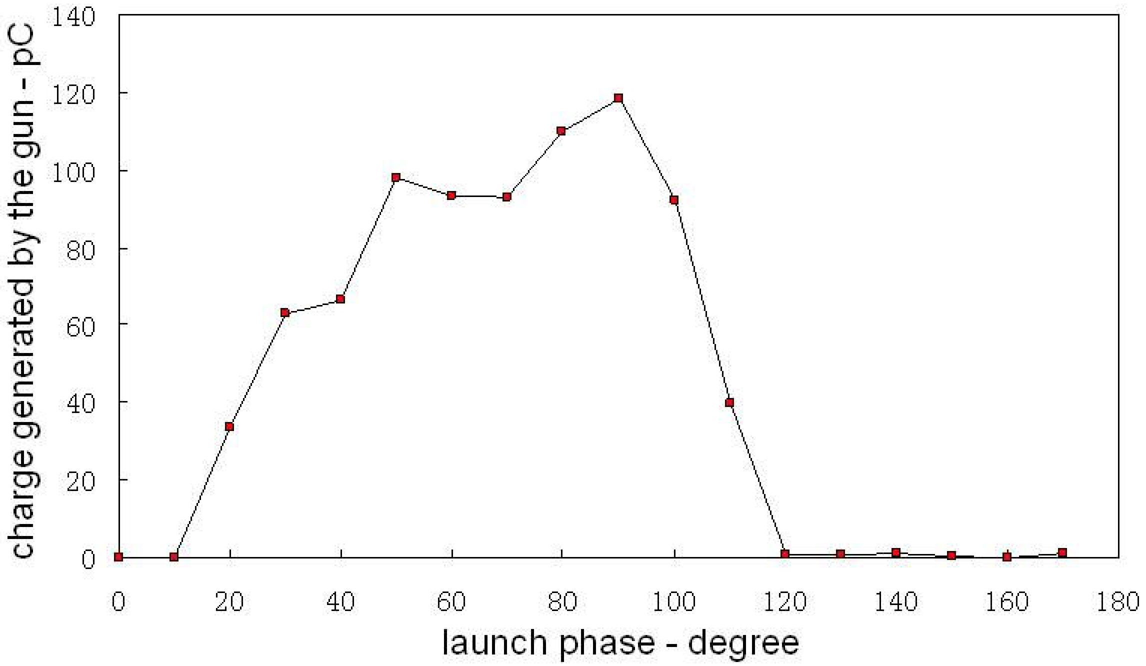

Figure 4.13. Charge vesus Launch Phase for the New Gun in the Test Stand Beamline. The test was conducted under low-charge condition. The abrupt drop of charge at 120° is used for fine tuning of the delay between the two UV micropulse trains, which is a multiple of 769ps.

micropulse in train B (B1) was set to this reference point where the generated charge barely becomes zero, then by using the motorized linear stage the first micropulse in train A (A1) was brought to this reference point, then the two trains have the same launch phase. This launch phase was varied by 1° of 1.3GHz (~2ps) to ensure the accuracy of the delay. After the adjustment was finished the launching phase was changed back to ~50° for normal operation. The beam energy centroid of the electron bunches generated by A1 and B1 was also checked with the spectrometer, and the difference was found to be only 0.2%.

Next the 16 UV micropulses and the 16 generated electron bunches need to be checked for balance, i.e. ideally all 16 micropulses should have same energy (in mJ) and all electron bunches should have the same charge (in nC). First a power meter is used which responds to the energy of the input UV micropulse, and the output is a voltage whose peak value is proportional to the energy. This power meter is placed immediately before each window to stop the UV micropulses, and with an oscilloscope the peak values for all 16 micropulses are measured and shown in Figure 4.14(a). The values are so close that good balance has been reached among the 16 micropulses.

Furthermore, the 16 electron bunches generated by the 16 micropulses are sent to pass through ICT2 (the downstream ICT right after the decelerator) for charge measurement. To reduce space charge effects, the diameter of the UV laser beam is set to 3~4mm by an iris placed before the beam splitting set, thus almost 100% charge transmission from ICT1 (the ICT immediately downstream of the gun) to ICT2 has been observed. The measured charge of each electron bunch is plotted in Figure 4.14(b), where charge deviation is larger than the energy deviation shown in Figure 4.14(a). This may be caused by not all the micropulses precisely hit the same spot on the photocathode and the QE is not uniform on the photocathode surface. Another observation from Figure 4.14(b) is that the electron bunches generated by train A generally have higher charge than those generated by train B. This would not cause any trouble in ~10ns RF pulse generation, since train A and train B are interleaved therefore the amplitude difference of wakefield is smoothed out. However, in ~20ns RF pulse generation, there would be a step-up in wakefield amplitude from the first half to the last half. This problem can be solved by placing a neutral density (ND) filter in the path of train A.

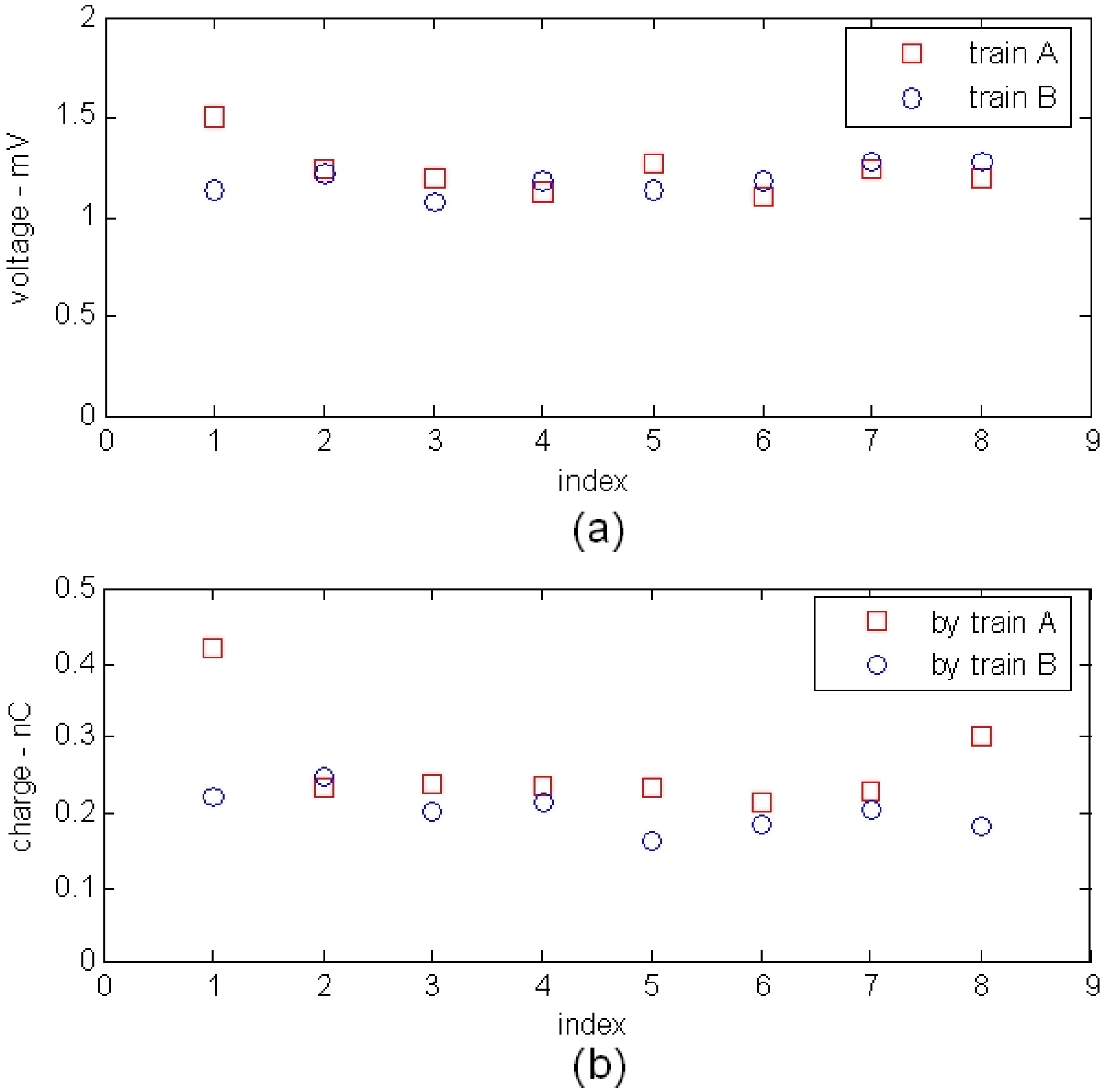

Figure 4.14. Comparison of Energy of Laser Micropulses and Charge of Generated Electron Bunches. (a) Relative micropulse energy detected as peak voltage by the power meter; (b). bunch charge detected by ICTs.

CHAPTER 5

POWER EXTRACTION BEAM TESTS

The power extraction beam tests have been implemented with the setup shown in Figure 4.5. The bunch charge in single bunch tests is higher than that in bunch train tests. In the single bunch test, up to 160nC of bunch charge has been pushed out of the gun and a maximum charge of 66nC has passed through the power extractor. In the bunch train tests, maximum bunch charge ranges from 5nC to 26.5nC, depending on the number of bunches in the electron bunch train (4 to 16).

The goals of single bunch tests and bunch train tests are also different. In the single bunch tests, since the length of the generated RF signal is short (2.2ns in simulation), its spectrum is limited by the bandwidth of the RF output coupler, thus the detected signal will not have a rectangular shape. The goal is to compare this distorted pulse with numerical simulation, and maximize generated power to examine space charge effect. On the other hand, in the bunch train tests, the primary goal is to demonstrate wakefield superposition by multiple bunches, which is better to achieve under low charge condition since space charge effects can thus be minimized. Besides this, to maximize the generated RF power is still a reasonable goal to aim at, although it is limited by the QE of the photocathode.

Since the insertion loss of the RF output coupler is -0.41dB (shown in Figure3.14) at 7.8GHz, the power coupling efficiency from the decelerator to the output WR112 waveguide is 91%, which means the extracted power is 91% of the generated power. Furthermore, coupling of the bidirectional coupler is -64.6dB at 7.8GHz, and cable attenuation from the bidirectional coupler to the oscilloscope is -5.9dB, where extra attenuators may be used when the signal is too strong.

5.1 Single Bunch Tests

During the single bunch tests the laser beam is configured as shown in Figure 4.7. Above the vacuum cross chamber there is a third window, under which is placed a third mirror to relay the image of the laser spot on the cathode to the laser camera for alignment. In the alignment process, first a visible helium laser beam (632nm) was sent to hit the center of the cathode, where whether the laser spot on the cathode was centered was checked by eye. Then the image of the laser spot was captured by the laser camera and displayed on a monitor, and the location of the laser spot was marked on the monitor screen. The UV laser beam, which cannot be seen by eye but can be seen with the camera and the monitor, was then guided to the cathode. The UV mirrors before the laser input windows, which can be controlled both manually and remotely, were adjusted so that the UV laser spot on the monitor overlaps with the helium laser spot. Then the UV laser beam was regarded to be striking the center of the cathode. Also after ten days of pumping the pressure inside the power extractor reached 7×10^{-9} Torr.

The output power versus charge over a range from 10 to 66nC has been studied. The extracted RF signal was measured with Tektronix TDS6154C 15GHz oscilloscope (sampling rate: 40Gs/s), and the charge transmitted through the power extractor was measured with ICT2 (shown in Figure 4.2). A 20dB attenuator was used to protect the oscilloscope. Figure 5.1(a) shows the maximum measured voltage and Figure 5.1(b) shows the corresponding spectrum after taking the discrete Fourier transform (DFT) of the voltage signal. The frequency of the measured signal is 7.8GHz indicating a good

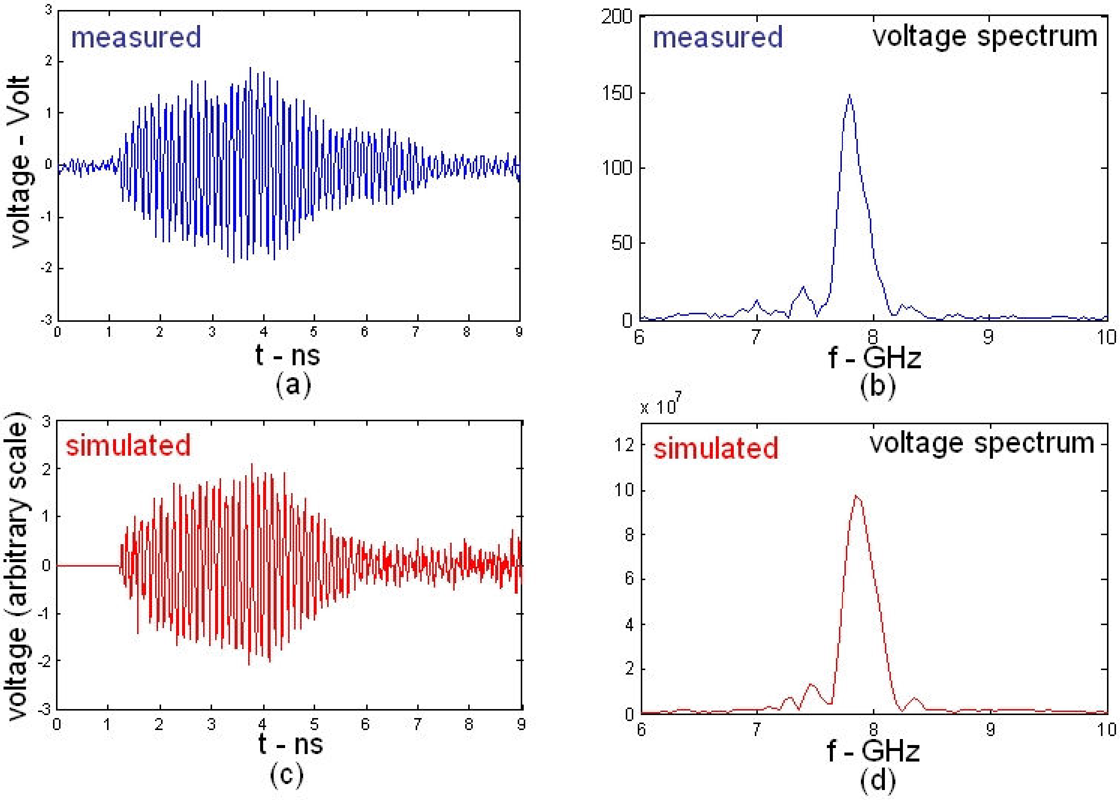

Figure 5.1. Comparison of the Measured and Simulated Signals Taking into Account the Bandwidth Limitation. (a). The measured voltage signal; (b). the spectrum of the measured signal; (c). simulated voltage signal with MAFIA T3 solver; (d). spectrum of the simulated signal.

agreement with theory and simulations. The pulse length is 1.7ns, smaller than the 2.2ns given by the MAFIA T2 solver where the bandwidth of the RF output coupler is not taken into consideration (shown in Figure 3-3(a)). Another numerical simulation with the MAFIA T3 solver was completed where the RF output coupler was included in the model. Figure 5.1(c) shows the simulated voltage, proportional to the transverse electrical field in the WR112 waveguide, in agreement with the measured voltage. Figure 5.1(d) shows the spectrum of the simulated voltage, which also agrees with the spectrum of the measured voltage.

The generated power has also been maximized by adjusting steering/trimming coils and focusing/defocusing magnets. After maximum power was reached, performance of the power extractor was also checked with lower charge. The power generated by different charges is plotted in Figure 5.2. From the figure we can see that the measured results agree well with simulation, and 30MW of power is generated when the driving charge is 66nC. The maximum single bunch charge transmitted through the decelerator was 66nC, as measured by ICT2. The charge measured by ICT1 is 160nC, which means only 40% of the charge coming out of the gun has passed the power extractor. This may be due to the strong space charge effect under high charge condition which may need to be taken into consideration in future experiments.

5.2 Bunch Train Tests

Later on, in order to generate RF pulses with lengths of a few nanoseconds to a few tens of nanoseconds, electron bunch trains were used for experiments. The electron bunch trains are generated by trains of UV micropulses, as shown in Figure 4.12. Since the shorted waveguide was then extended for longer delay, the beamline was pumped

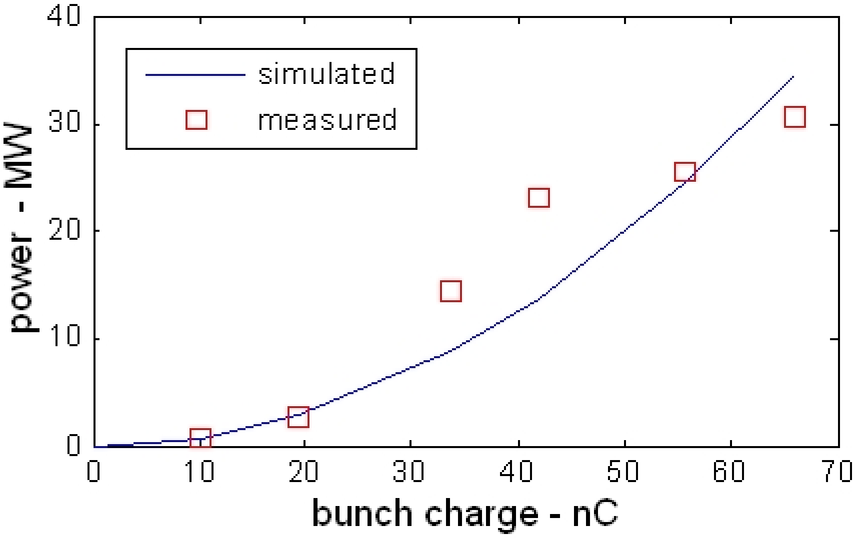

Figure 5.2. Generated Power by Different Bunch Charges in Single Bunch Tests.

again. The pressure curve is plotted in Figure 5.3, while it can be seen approximately 5 days after ion pumps were turned on, the pressure reached 6.3×10^{-9} Torr.

The bunch train tests are different from single bunch tests from the following aspects: i). Single bunch tests show the pulse response of the power extractor, i.e. the output RF signal acts as a “Green’s function” of the structure, while the bunch train tests show superposition of these pulse responses; ii). In single bunch tests, the generated RF pulse is short and its spectrum is limited by the bandwidth of the RF output coupler, while in bunch train tests the spectrum of a long pulse (>10ns) can fit well in the coupler bandwidth so signal distortion is negligible; iii). In single bunch tests to reach the same output power level, the charge per bunch is a few times (3 ~ 4 for this structure) higher than that needed in bunch train tests, thus in single bunch tests the space charge effect is stronger.

5.2.1 RF Pulse Generation by 16 Bunches Spaced by 769ps. When the two micropulse trains are interleaved, the spacing between two adjacent electron bunches is 769ps, thus the total length of the electron bunch train is (16-1)×769ps = 12.3ns, which is able to generate 10ns RF pulses. Figure 5.4 shows a clear signature of wakefield superposition, where the first few bunches and finally all 16 bunches are passed through the power extractor. When the electron bunch train becomes longer and longer, the generated RF pulse is getting longer and longer, while the spectrum is getting narrower and narrower. The strongest voltage signal obtained is shown in Figure 5.5(a), where 2.4MW of power has been generated by a charge of 4.8nC per bunch, and the spectrum is shown in Figure 5.5(b). The curve of generated power by different charges is plotted in Figure 5.6.

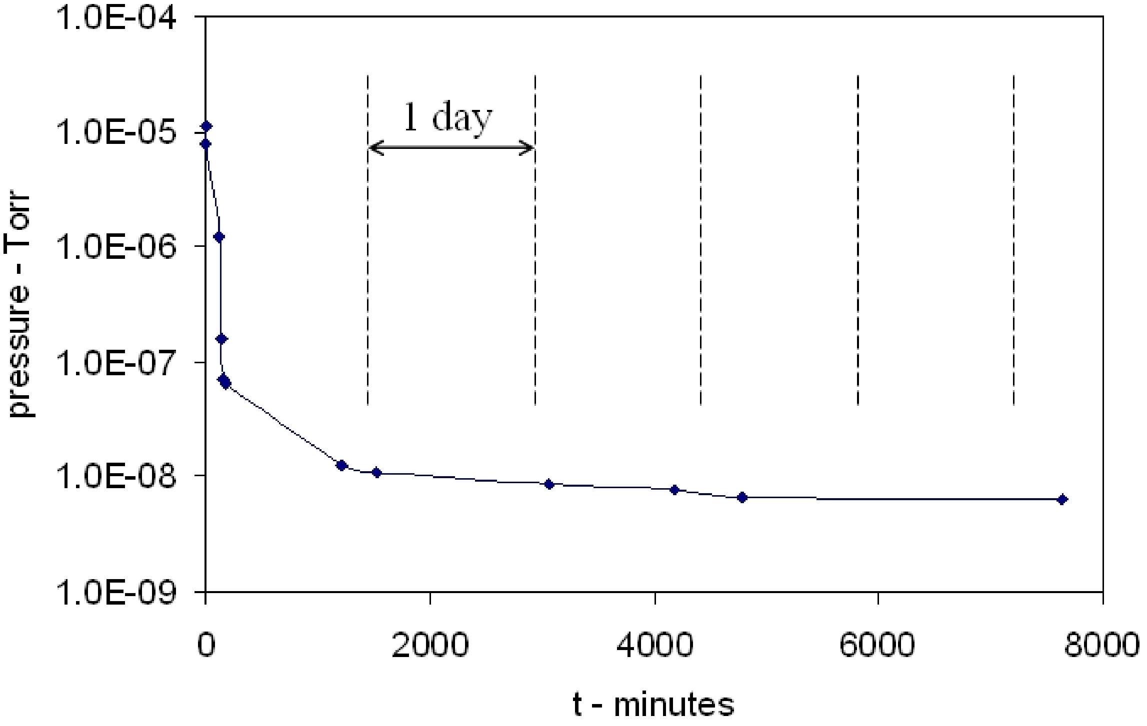

Figure 5.3. Pressure Curve After Ion Pumps were Switched on.

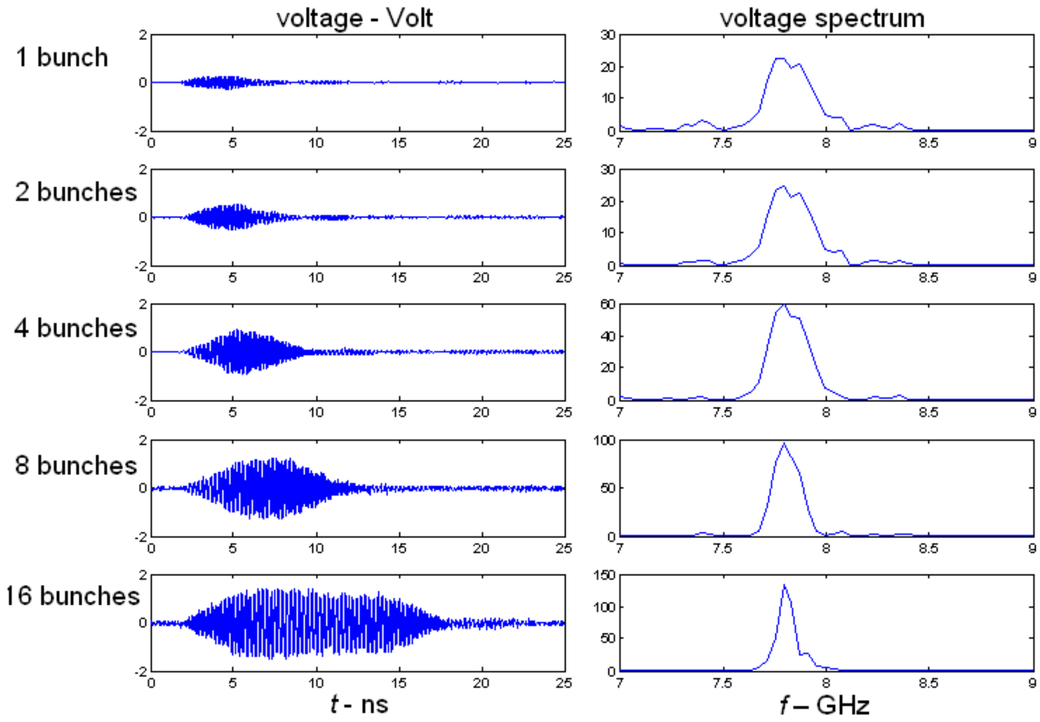

Figure 5.4. Detected Voltage Signals Excited by 1-16 Bunches Spaced by 769ps. When more and more consecutive electron bunches are passed through the power extractor, the generated RF pulse is getting progressively longer due to coherent wakefield superposition, while the spectrum is getting progressively narrower. Voltage is normalized to 1nC per bunch.

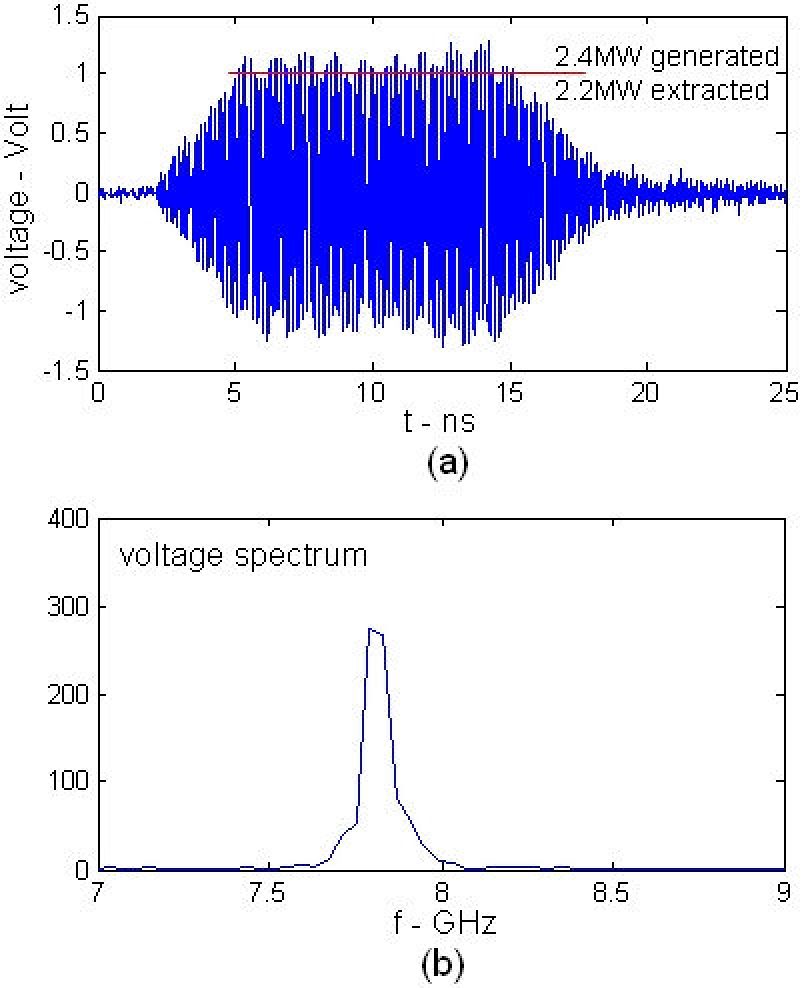

Figure 5.5. 10ns 2.4MW RF Pulse Generation. (a). The measured voltage signal (with 13dB attenuator); (b). the spectrum of the measured signal.

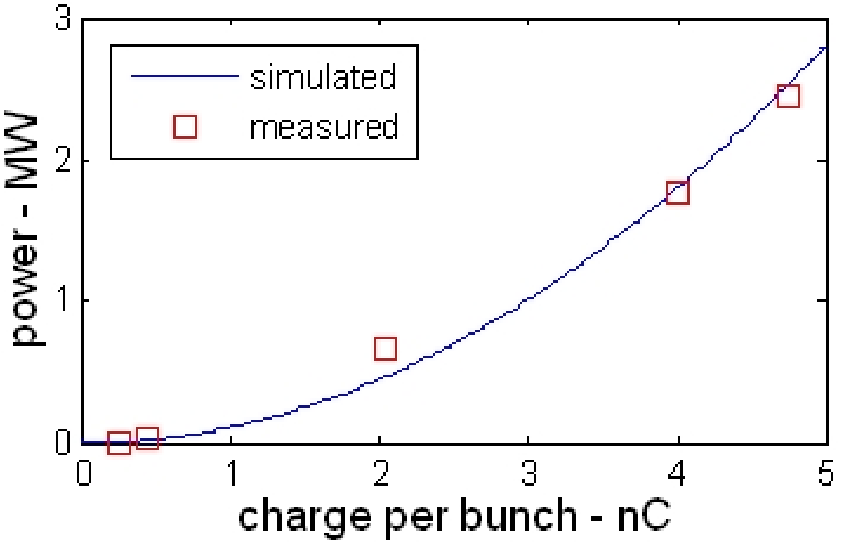

Figure 5.6. Generated Power by Different Bunch Charge in Bunch Train Tests with a Bunch Spacing of 769ps. 2.4MW of maximum power is generated at 4.8nC per bunch.

5.2.2 RF Pulse Generation by 16 Bunches Spaced by 1.538ns. When one micropulse train follows the other, the spacing between two adjacent electron bunches is 1.538ns, thus the total length of the electron bunch train is (16-1)×1.538ns = 24.6ns, which is able to generate 22ns RF pulses. A ND filter with 79% transmission is placed before train A to balance the output RF signal. As shown in Figure 5.7(a), when only micropulse train A or B is passed through the decelerator, a ~10ns RF pulse is generated; when both of the two trains are passed through, a ~22ns RF pulse is generated. The portion of the waveform after t = 31ns is the reflected signal, which can be distinguished from the forward signal due to the delay provided by the shorted waveguide. The curve of generated power by different bunch charges is plotted in Figure 5.8; 0.77MW of maximum power has been achieved by a charge of 4.9nC per bunch.

5.2.3 RF Pulse Generation by 4 Bunches Spaced by 769ps. In the AWA beamline, the beam current is limited by the QE of the magnesium photocathode, thus for a long train the bunch charge is small. For example, in Sections 5.2.1 and 5.2.2, when the train contains 16 bunches, the bunch charge is less than 5nC.

From Figure 3.3(b) it can be seen that for a train of bunches spaced by 769ps, after 4 bunches pass the decelerator, the saturation power level (flat-top level) has been reached. Thus in order to reach the maximum power level under the present low-charge condition, by removing the laser splitters S1 and S2 in Figure 4.8, the UV laser pulse was split into only four micropulses to generate four electron bunches with higher charge per bunch. Figure 5.9(a) shows the detected voltage signal, and Figure 5.9(b) shows the spectrum. The maximum generated power is 44MW at 26.5nC per bunch, while the extracted power is 40MW.

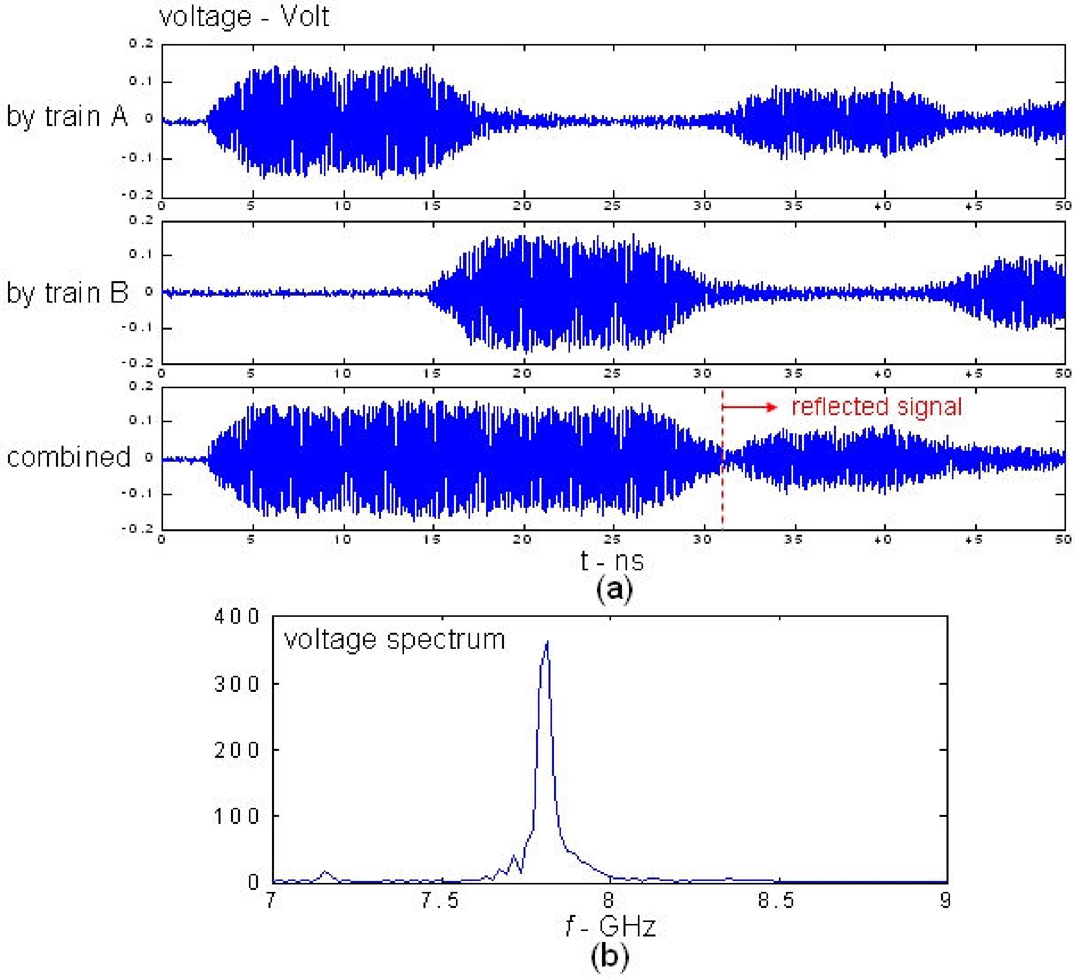

Figure 5.7. Detected Voltage Signal Excited by 16 Bunches Spaced by 1.538ns. For the configuration where one train follows the other: (a) the rf signal generated by each train and the total signal, normalized to 1nC per bunch (with -13dB attenuator); (b). the spectrum of the total RF pulse.

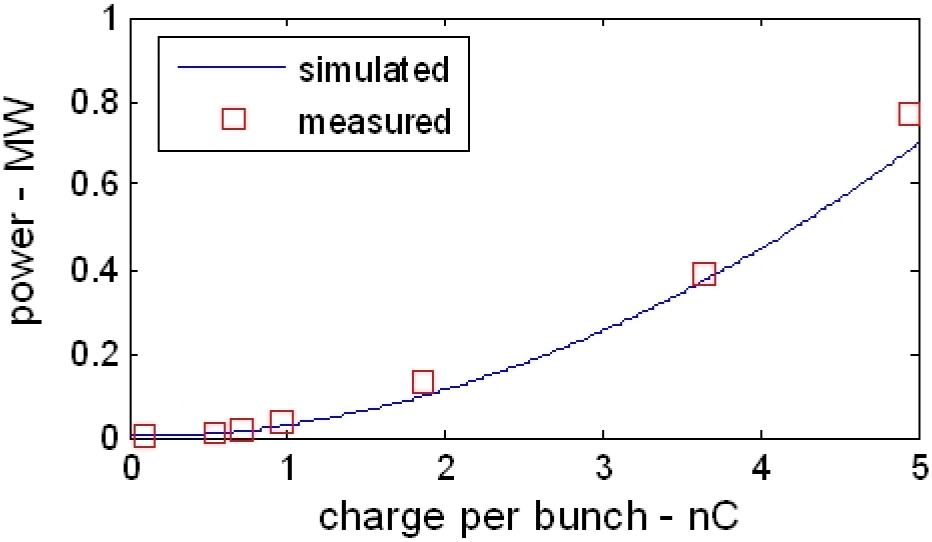

Figure 5.8. Generated Power by Different Bunch Charges in Bunch Train tests with a Bunch Spacing of 1.538ns.

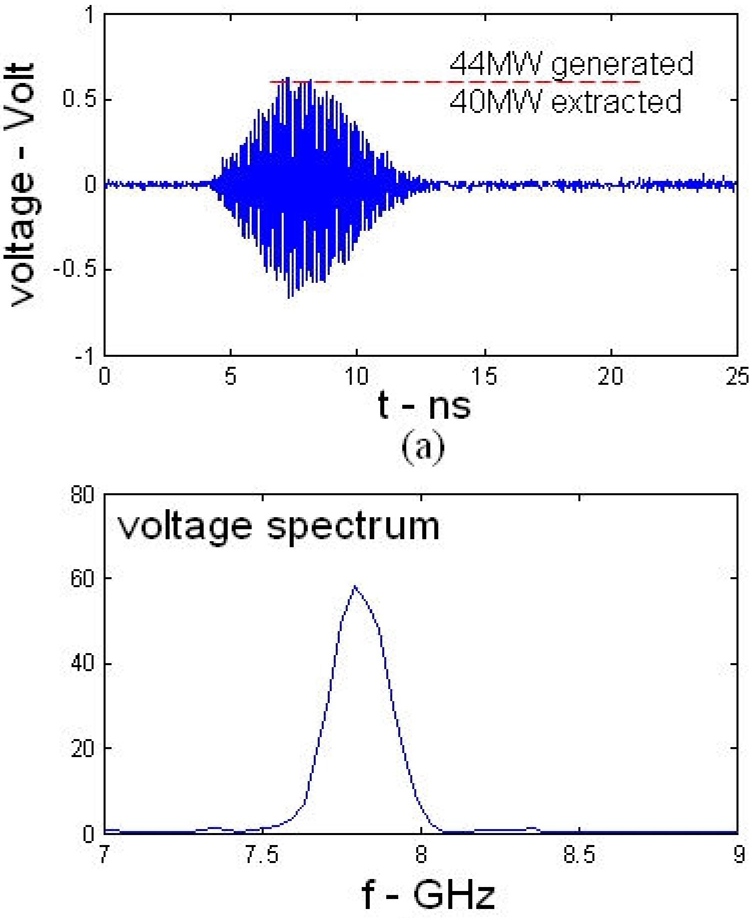

(a)

(b)

Figure 5.9. Generation of 44MW of Flat-top Saturation Power by 4 Electron Bunches Spaced by 769ps. The charge per bunch is 26.5nC. (a). The measured voltage signal (with -30dB attenuator); (b). the spectrum of the measured signal.

CHAPTER 6

HIGHER FREQUENCY I: A 26GHZ POWER EXTRACTOR DESIGN

The prototype 7.8GHz power extractor has been successfully designed and tested, as described in Chapters 2 – 5, although 100MW of power has not been demonstrated due to the limitations on drive beam intensity resulting from the relatively low QE of the magnesium photocathode. Consequently a DL power extractor at a much higher frequency, 26GHz, has been designed to make use of the very short electron bunch length (1.5~3mm) at the AWA.

For high energy physics accelerator applications, klystrons are commercially available to provide high quality RF power sources below X-band frequencies. There are several facilities operating in the US at higher frequencies such as the Ku-band 17.1 GHz gyroklystron at University of Maryland (Gouveia 2002), the 34GHz Ka band magnicon at Yale/Omega-P (Nezhevenko 2003), and the 91GHz W band gyroklystron (Ives 2003). However, the range 20~30GHz is still an open window for high power source.

By using the 20th harmonic of the fundamental frequency of the AWA RF system, a 26GHz (1.3GHz × 20) dielectric loaded power extractor has been designed. The 26GHz structure uses the same scheme as the 7.8GHz structure, as shown in Figure 3.1. In this chapter, the design of the deceleration waveguide, the output coupler and the measurement method are introduced (Jing 2009).

6.1 Design of the 26GHz Dielectric-loaded Decelerator

The 26GHz DL power extractor still uses a circular geometry, and the deceleration mode is still the TM_{01} mode, therefore Equations 2.5-2.6 still hold in this case. The main consideration is to reach high [r/Q] while keeping the inner diameter

(ID = 2a) large to allow high charge to pass through, so that high power can be generated. At such a high frequency, the outer diameter (OD) of the dielectric tube is small, and in order to keep a large ID at the same time, the wall of the dielectric tube will be very thin, which is a challenge for dielectric fabrication. The final design is a trade-off between these requirements.

The parameters of the deceleration waveguide are listed in Table 6.1. The ID and OD are 7mm and 9.068mm, respectively. The dielectric material is Fosterite, with a relative permittivity of 6.64, and a loss tangent of 1×10^{-4}. The waveguide is 300mm long. The synchronous frequencies (at which the phase velocities of the electromagnetic modes are equal to *c*, the speed of light in free space) of the TM_{01} mode and the dipole HEM_{11} mode are 26GHz and 23.5GHz, respectively. The TM_{01} mode has a moderate value of the group velocity of 0.25*c*, close to that for the 7.8GHz power extractor. The $[r/Q]$ of the TM_{01} mode is much larger than that for the 7.8GHz power extractor, since the ID is much smaller. Figure 6.1 shows the dispersion curves of the TM_{01} mode and HEM_{11} mode. It can be seen the two curves intercept the light line at 26GHz and 23.5GHz, respectively.

Figure 6.2(a) shows a 100mm section of the dielectric tube. Three tubes will be used in a deceleration waveguide. Figure 6.2(b) shows the electric field of the TM_{01} mode, simulated with CST Microwave Studio. The maximum electric field is on the axis, thus the possibility of breakdown on the metallic surface is reduced.

The CST MAFIA T2 module was used to simulate the generated electromagnetic pulse (specifically the longitudinal electrical field) by a Gaussian electron bunch at the downstream end of the deceleration waveguide, and the result is shown in Figure 6.3(a). The bunch length is adjustable at AWA by changing the duration of the laser pulse,

Table 6.1. Design Parameters of the 26GHz Dielectric-loaded Decelerator.

Synchronous frequency	f_0	26GHz
Inner diameter of the dielectric tube	$2a$	7.00mm
Outer diameter of the dielectric tube	$2b$	9.068mm
Dielectric tube length	L	300mm
Relative permittivity of the dielectric	ε_r	6.64
Normalized group velocity of the EM mode	β_g	0.25
Loss tangent of the ceramic	δ_d	1×10^{-4}
Total quality factor (metallic wall and dielectric losses)	Q	2950
"*r* over *Q*" per unit length of the structure	$[r/Q]$	9.79K Ω /m

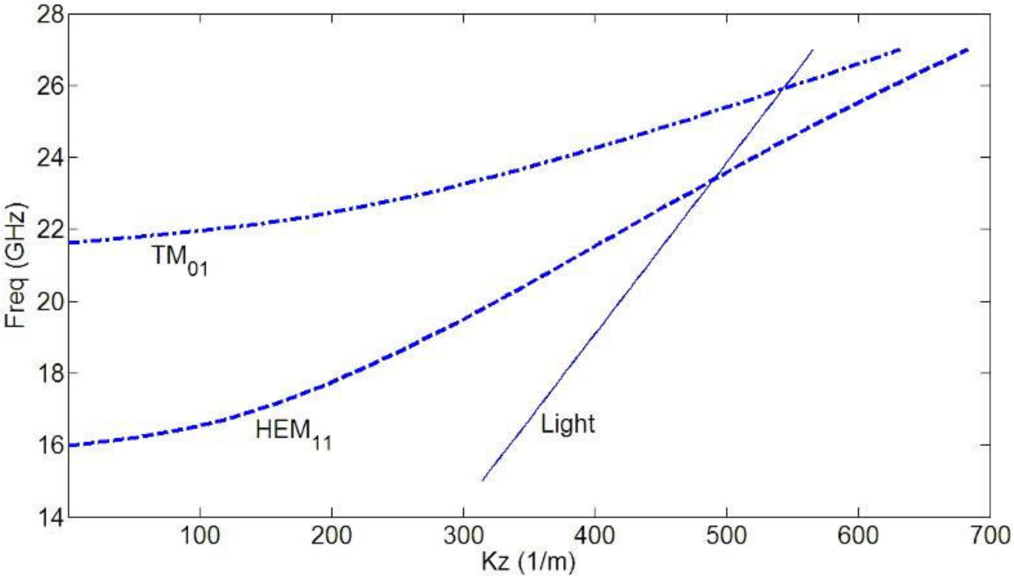

Figure 6.1. The Dispersion Curves of the TM_{01} Mode and the HEM_{11} Mode of the 26GHz Dielectric-loaded Waveguide. The two curves intercept the light line at 26GHz and 23.5GHz, respectively.

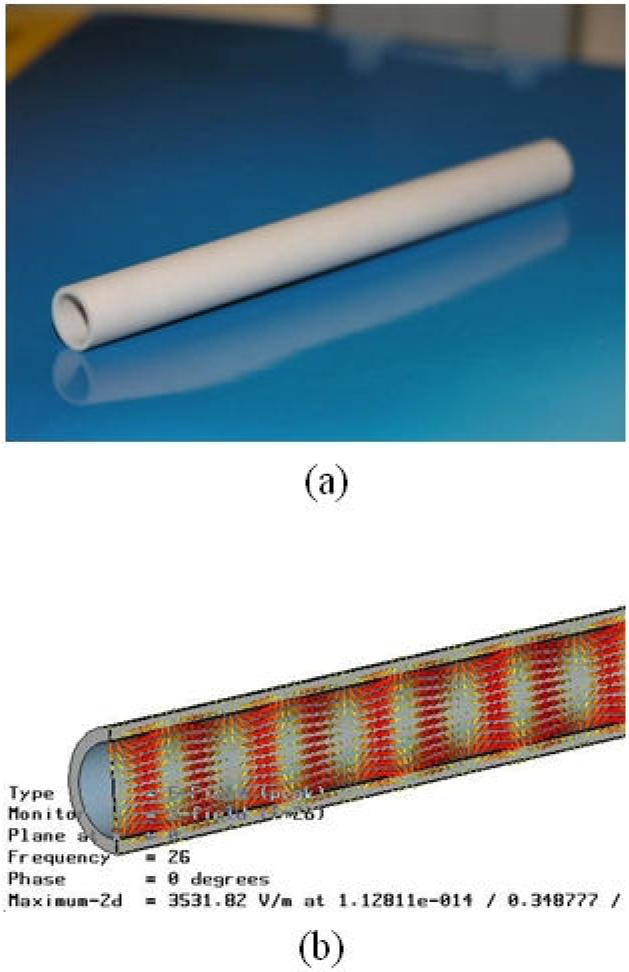

Figure 6.2. The Dielectric Tube for the 26GHz Decelerator. (a). A 100mm section; (b). the electric field of the TM_{01} mode, simulated by CST Microwave Studio.

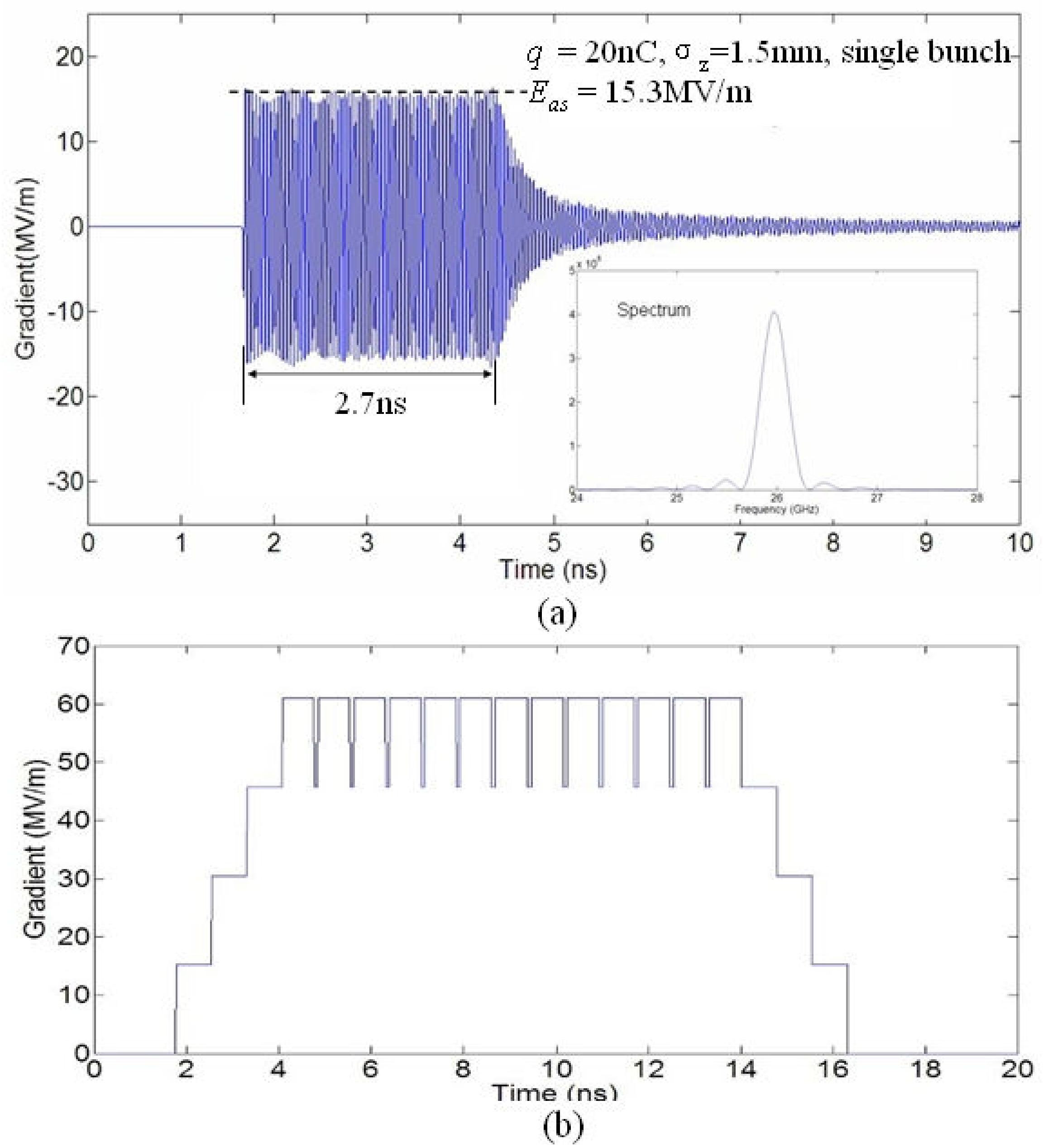

Figure 6.3. EM Pulses Generated in the 26GHz Decelerating Waveguide by an Electron Bunch and a Bunch Train. The bunch length is 1.5mm: (a). an 2.7ns pulse is generated by a 20nC single Gaussian electron bunch; (b). the envelope of the EM pulse generated by a train of 16 bunches with bunch spacing 0.769ns and bunch charge 20nC, corresponding to 148MW of power.

thus a shorter bunch length 1.5mm is chosen and not the previous 2mm for a higher bunch form factor. A 2.7ns EM pulse is generated by the single bunch and the envelope is used to construct the envelope of the RF signal excited by a bunch train. The spectrum shows the frequency is at 26GHz as expected. The envelope of the generated EM pulse by a train of 16 bunches (20nC each) is shown in Figure 6.3(b). As shown in the figure, the pulse length is 10ns, and the simulated power is 148MW, which agrees with the value calculated from Equation 2.22.

6.2 Design of the 26GHz Output Coupler

In the design of the 26GHz power extractor, the standard WR34 waveguide is used for signal output, and a different type of output coupler was chosen in order to reach a wider bandwidth. Figures 6.4(a) and (b) show the simulation model of the output coupler in CST Microwave Studio. At the downstream end of the deceleration waveguide, there is a transition to a hollow circular waveguide. The circular waveguide is connected to a widened rectangular waveguide, and the widened waveguide is connected with a standard WR34 waveguide. Inside the widened waveguide, there is a metallic pin for tuning. The diameter and length of the circular waveguide, and the position and size of the pin, are adjusted for impedance matching. Figures 6.4(c) and (d) show the magnitudes of the electric and magnetic field inside the final structure, respectively.

In S-parameter simulation, in order to investigate the coupling not only between the TM_{01} mode and the TE_{10} mode, but also between the HEM_{11} mode and the TE_{10} mode, the WR34 waveguide end is set as port 1, and the deceleration waveguide end is set as port 2. The simulation results are shown in Figure 6.5. The insertion loss is smaller than -1dB over the 1GHz range, while the reflection is lower than -15dB within a 600MHz

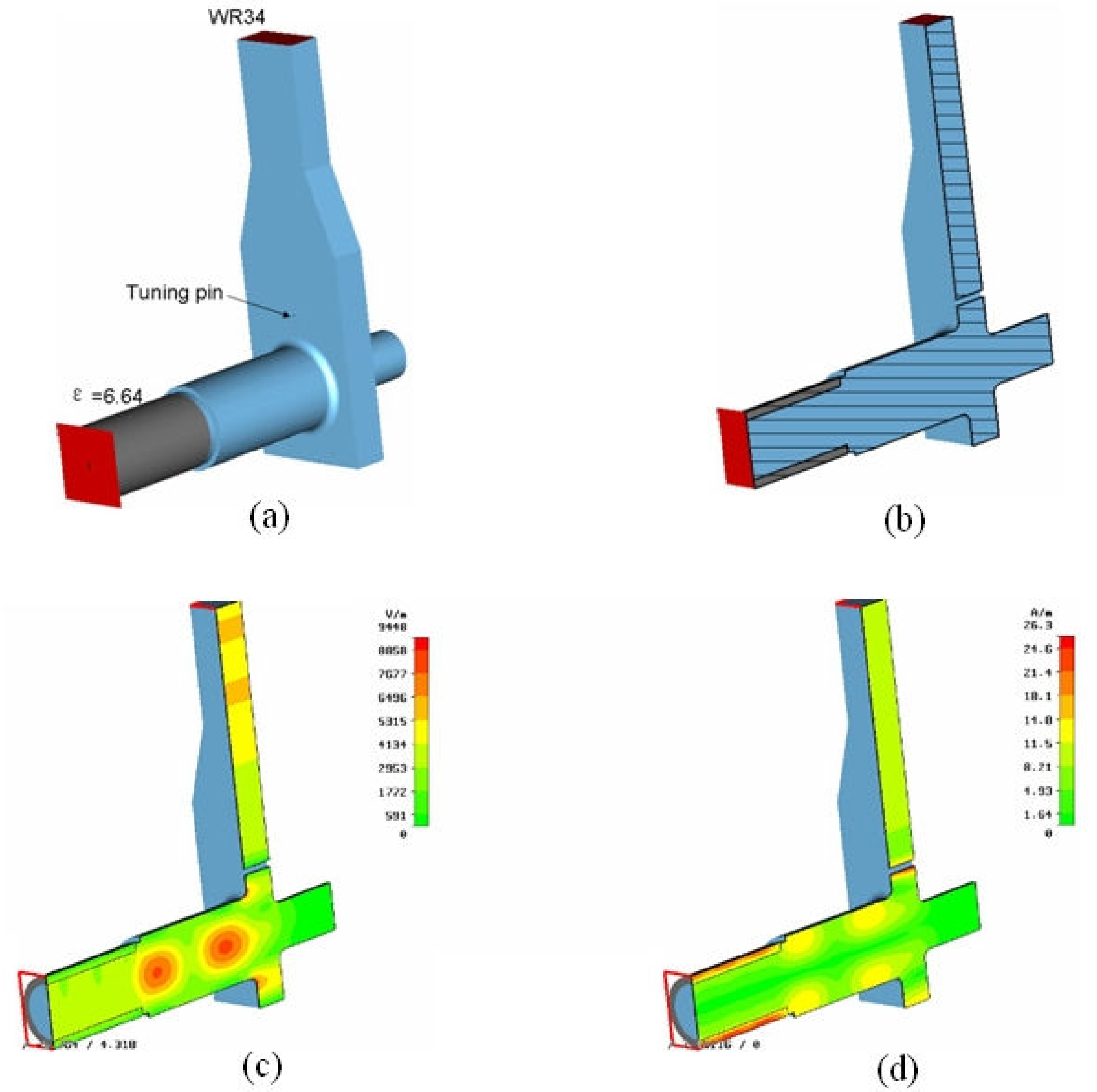

Figure 6.4. Geometry of the 26GHz TM_{01}-TE_{10} Output Coupler. (a) The whole coupler model in CST Microwave Studio; (b). the cutplane; (c). magnitude of the electrical field inside the coupler; (d). magnitude of the magnetic field.

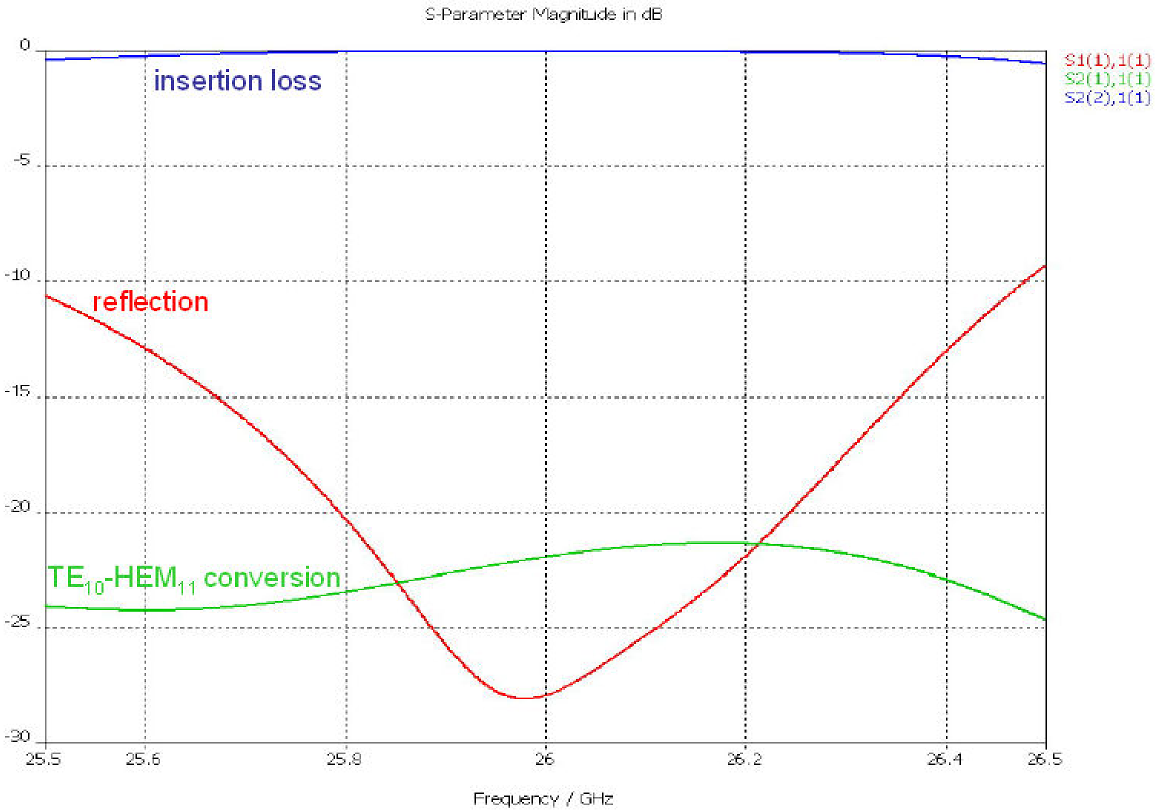

Figure 6.5. Simulated S-parameters of the 26GHz TM_{01}-TE_{10} Output Coupler. Port 1 is the WR34 waveguide end and port 2 is the deceleration tube end.

bandwidth, which means more than 97% of generated power can be coupled out. The coupling between the HEM_{11} mode and the TE_{10} mode is below -20dB, which means the contribution of the HEM_{11} mode is negligible.

6.3 Fabrication and Cold Test

After the parameters of the deceleration waveguide and the output coupler were optimized and finalized, the 26GHz power extractor assembly was fabricated at ANL. The metallic part of the deceleration waveguide and the output coupler is made of OFE copper, except for the standard stainless steel flanges.

The dimensions of the output coupler housing are shown in Figures 6.6(a) through (c). Figure 6.6(a) shows the inner dimensions on the longitudinal cutplane, while Figure 6.6(b) shows those on the transverse cutplane. The left side of Figure 6.6(a) is the upstream side of the metallic housing, and the right side is the downstream side. Figure 6.6(c) shows the details of the circled part in Figure 6.6(a), which is a step to prevent the dielectric tube from sliding into the downstream hollow circular waveguide.

Figure 6.7(a) shows the two halves of the output coupler housing before brazing, where the 0.84mm-thick pin can be seen. First the coupler housing was brazed to form a whole component, and then it was brazed with the copper tube of the deceleration waveguide. Two 3-3/8” flanges were brazed to the upstream and the downstream ends of the power extractor, and one 2-1/2” flange was brazed onto the WR34 waveguide. The whole structure is shown in Figure 6.7(b), where three 100mm dielectric tubes are also shown. Later on, these dielectric tubes were inserted into the copper tube, and secured by a copper plug placed at the upstream end (not shown in the figure). After being assembled the 26GHz power extractor was ready for low power test (cold test).

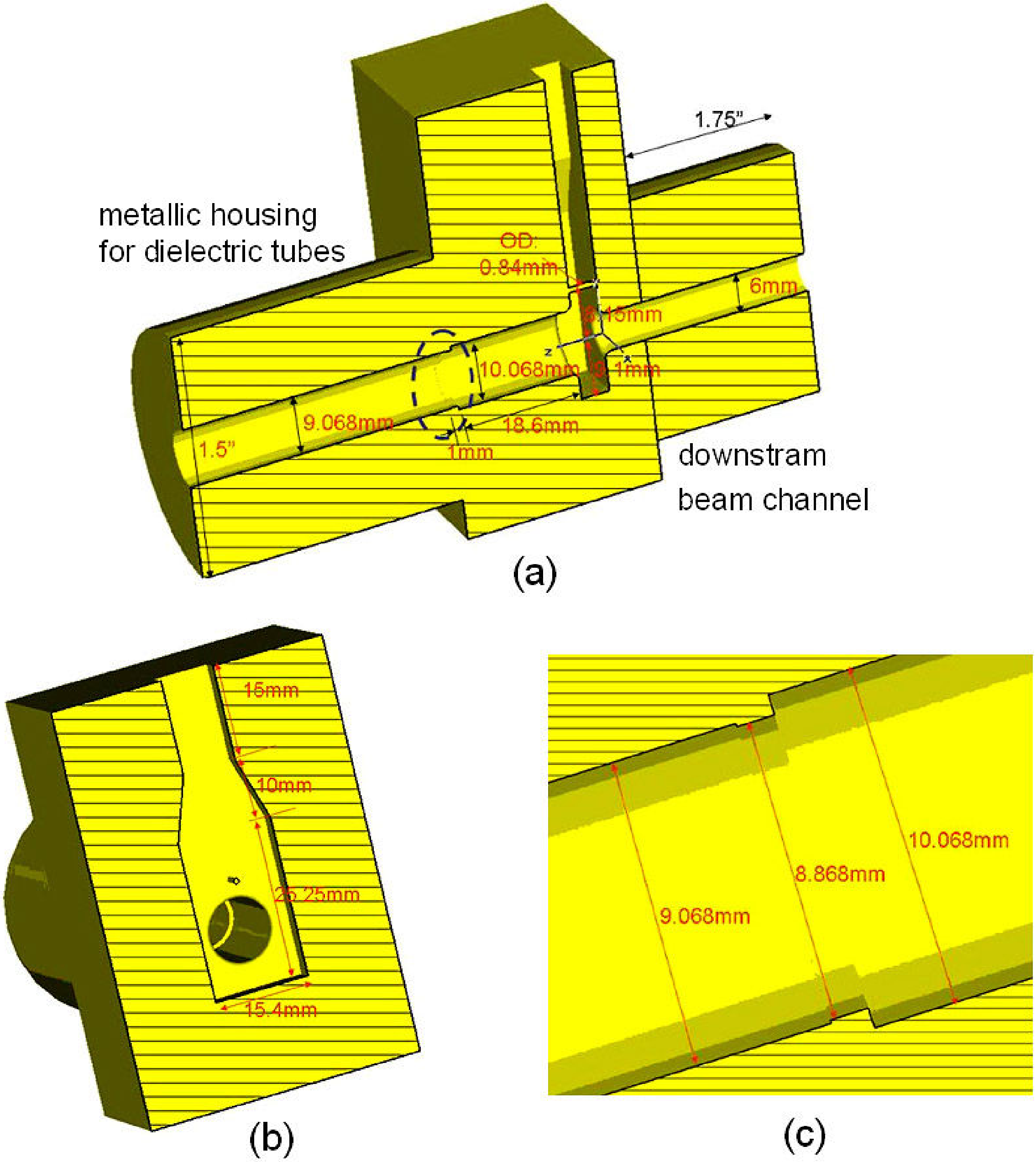

(a)

(b)

(c)

Figure 6.6. Dimensions of the 26GHz Output Coupler Housing. (a). The longitudinal cutplane; (b). a transverse cutplane; (d). details of the circled part in (a).

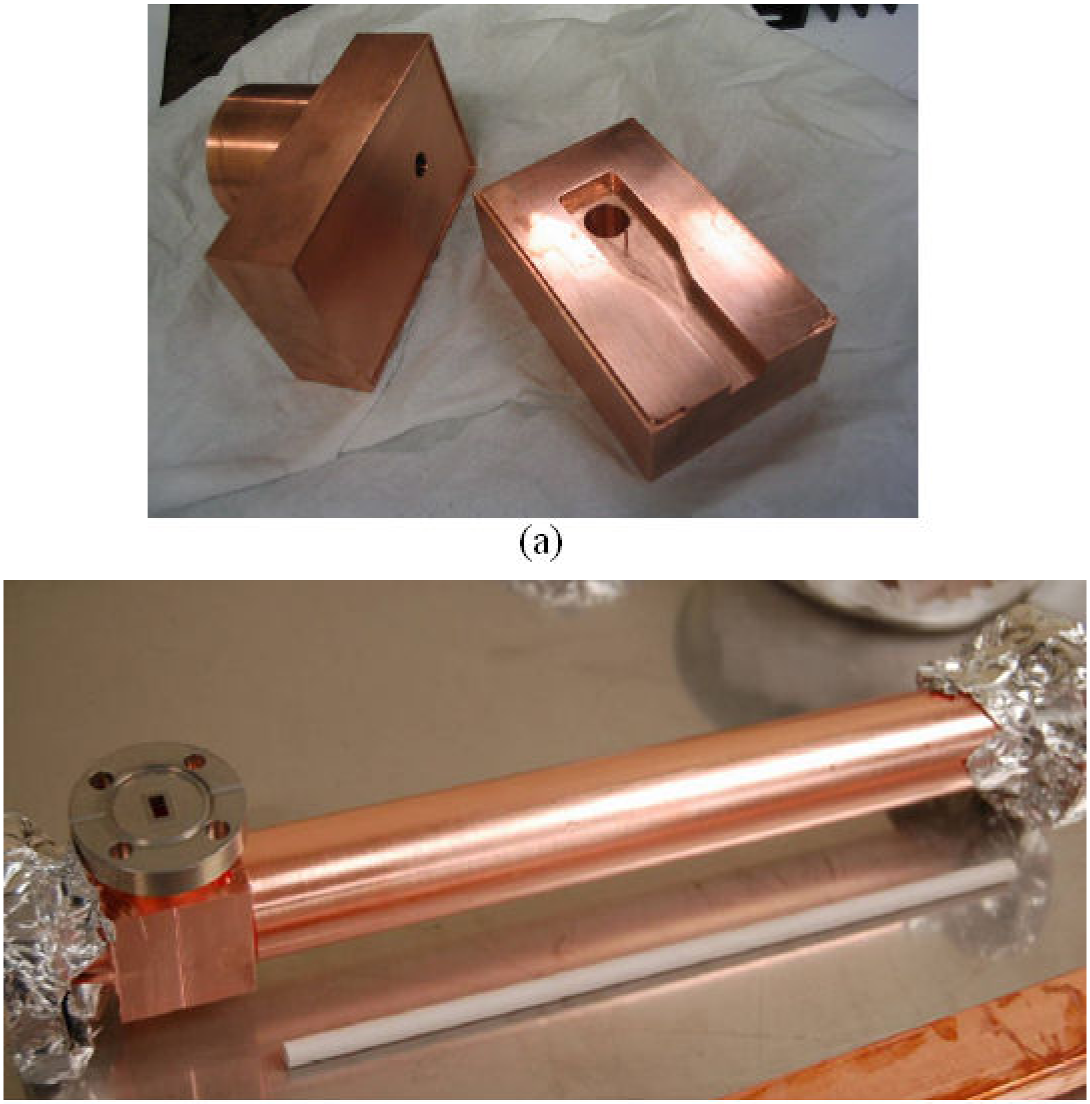

(a)

(b)

Figure 6.7. The Implemented 26GHz Power Extractor. (a). Output coupler housing before brazing; (b). the whole power extractor after brazing. Three 100mm dielectric tubes are also shown.

The setup for the cold test of the output coupler is similar to what shown in Figure 3.13(b), except that the dimensions of the TEM-TM_{01} mode launcher are different. Recall Figure 3.13(a), where the S-parameters were measured with the network analyzer HP8510C, and a mode launcher was used to convert the TEM mode in the coaxial cable to the TM_{01} mode in the deceleration tube. At the output port on the WR34 waveguide, a TE_{10}-TEM adapter was also used to return the signal to the HP8510C. The mode launcher consists of a center pin with a disc on the tip, and a grounded copper inserted into the copper sleeve. For the 26GHz structure, the diameter of the disc *dp* is 4mm, the thickness of the disc *tp* is 1.62mm, and the distance between the disc and the plug *gp* is 2mm. The transmission of the mode launcher is 97% in the 25-27GHz range. The bandwidth of the mode launcher is much wider than that of the output coupler, thus the insertion loss due to the mode launcher is negligible.

The measured S-parameters of the combination of the mode launcher, the 300mm-long DL waveguide and the output coupler are plotted in Figure 6.8. The assembly has a measured insertion loss S_{21} = -2.3dB at 26GHz. By subtracting the loss from the TE_{10}-TEM adapter (-0.5dB), and the theoretical losses (-1dB, including metallic and dielectric losses of the DL waveguide), the loss due to the output coupler is -0.8dB, corresponding to a power coupling efficiency 83%. It needs to be mentioned that losses of the decelerator itself have been taken into account by the attenuation coefficient α_0 in Equation 2.22, therefore in the measurement of coupling efficiency of the 26GHz output coupler, these losses should not be counted twice. Hence the losses from the adapter, the metallic wall, and the dielectric were subtracted from the measured insertion loss of the assembly to get the real insertion loss of the output coupler.

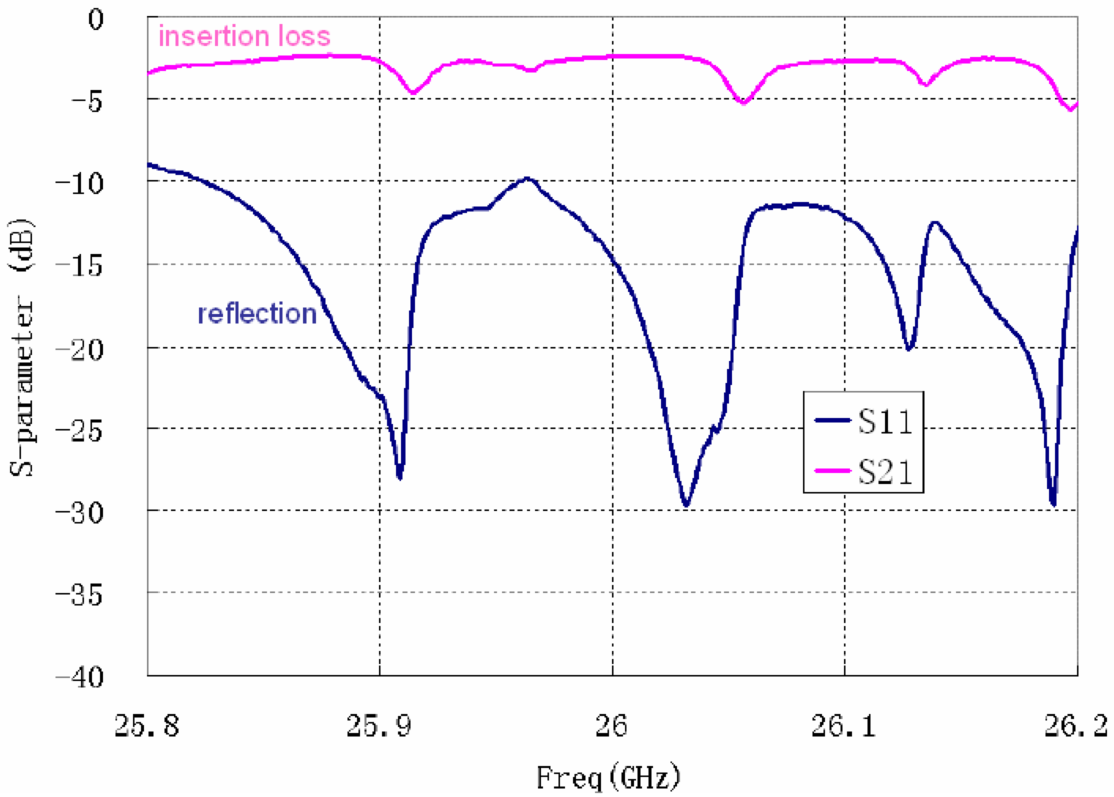

Figure 6.8. Measured S-parameters of the Power Extractor.

6.4 Design of a 26GHz Power Detector

In the 7.8GHz power extraction test, a shorted waveguide was used to delay the reflected RF pulse for signal identification. Before the shorted waveguide, a 7.8GHz bidirectional coupler was used to couple the forward signal to the oscilloscope for detection. For the 26GHz power extraction test, in order to simplify the fabrication process, a probe with a single output port is designed instead of a bidirectional coupler. Since the shorted waveguide delays the reflected signal, this simpler probe works as well as a bidirectional coupler. The probe, together with the WR34 waveguide section on which the probe is fixed, is referred to as a power detector.

Figure 6.9(a) shows the CST Microwave Studio model of the power detector. There are two openings on the upper wall of the WR34 waveguide, above which a coaxial probe is placed. There is a distance from the tip of the probe to the outer surface of the waveguide wall, which is critical for obtaining the right amount of coupling. Figure 6.9(b) gives a top close-up view of the two openings and the probe, while the simulated S-parameters are plotted in Figure 6.9(c). The coupling from the TE_{10} mode in the WR34 waveguide to the TEM mode in the coaxial cable is -57dB, while the coupling to other higher order modes is well suppressed.

Figure 6.10(a) shows the power detector after fabrication, with an ultra-high-vacuum probe on the top. Adaptors at both ends of the WR34 waveguide are used for calibration. The measured coupling is -51dB at 26dB, as shown in Figure 6.10(b). The coupling is stronger than the simulated value because the center conductor of the probe is slightly longer than the nominal value. The flat part of the curve is shifted by 200MHz, which might be due to an imperfection in the fabrication process.

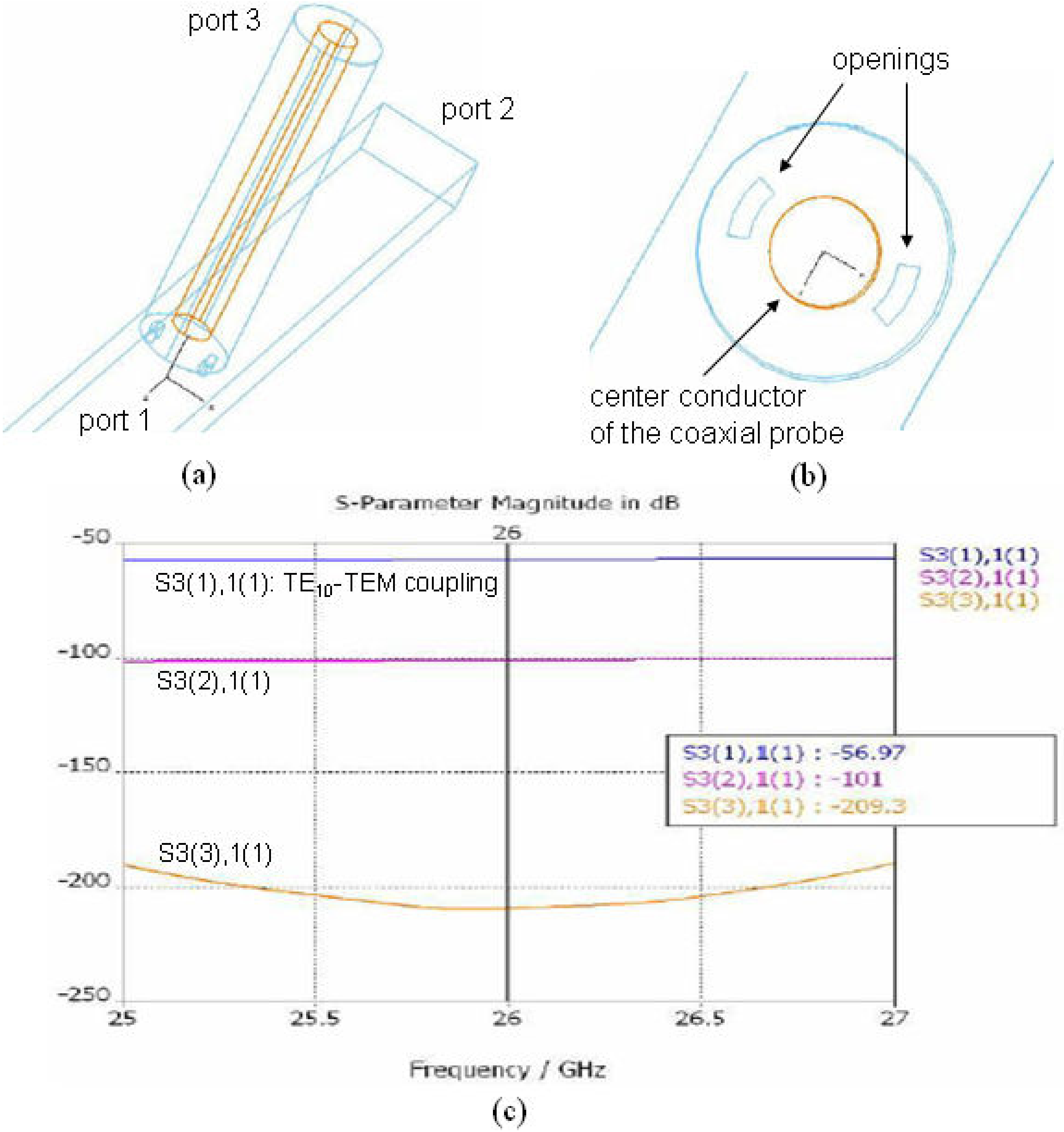

(a) (b) (c)

Figure 6.9. Design of the 26GHz Power Detector. (a). Model of power detector; (b). the details of the openings on the waveguide; (c). simulated S-parameters.

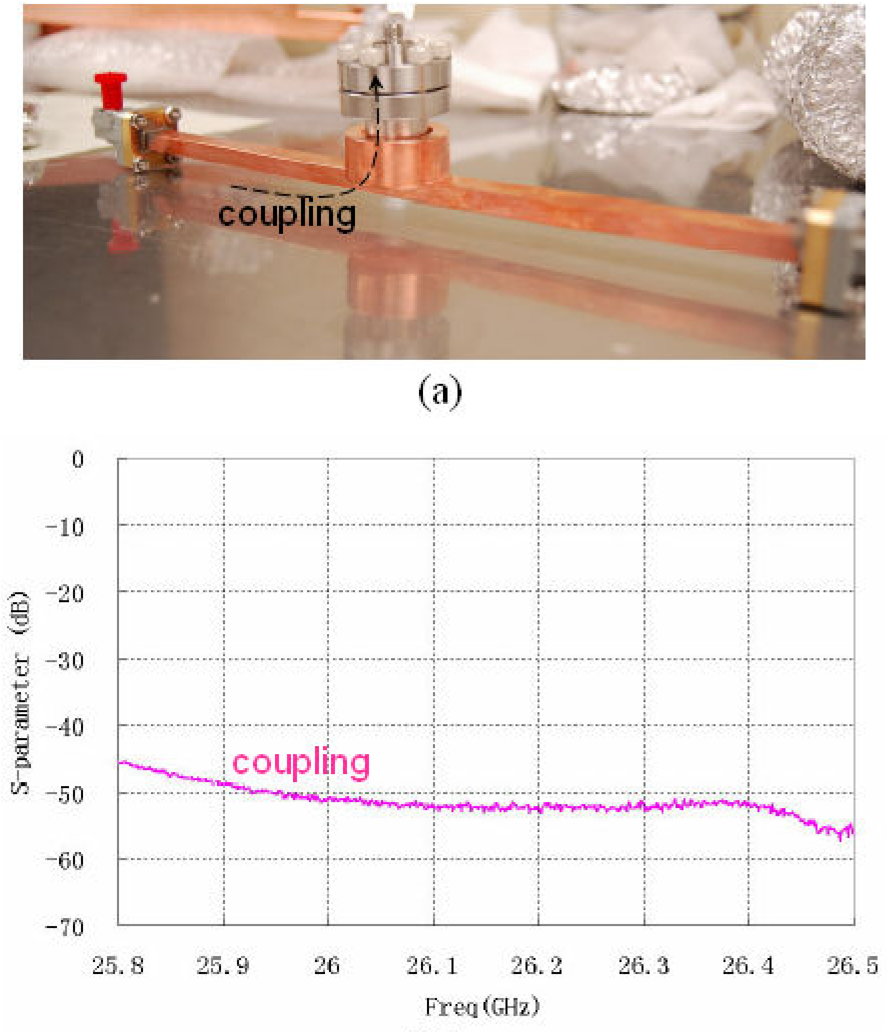

(a)

(b)

Figure 6.10. The Implemented 26GHz Power Detector. (a). The power detector with a ultra-high-vacuum probe on the top (shown with adapters for calibration); (b). measured coupling from the WR34 waveguide to the upper coaxial port.

6.5 Proposed Setup for Beam Tests

Since the expected frequency of the extracted signal is 26GHz, which is beyond the bandwidth of the fastest oscilloscope, a 16GHz Tektronix oscilloscope at this time, direct observation of the 26GHz signal is not possible. A heterodyne receiver circuit can be used to down-convert the 26GHz signal to a lower frequency for detection with the 16GHz oscilloscope.

Figure 6.11 shows the diagram of signal detection. First the 26GHz signal is down-converted by a 14.576GHz local oscillator (LO) signal to 11.424GHz with a mixer. Then the 11.424GHz signal is passed through a band pass filter (BPF) with a bandwidth of 200MHz to block noise and other frequency components. The filtered signal is sent to the 16GHz oscilloscope for detection. Then finally the 26GHz signal can be recovered by multiplying the detected signal (~11.424GHz) and the 14.576GHz LO signal. A high-vacuum load made with SiC is planned to be placed at the end of the output waveguide to absorb the high-power pulse.

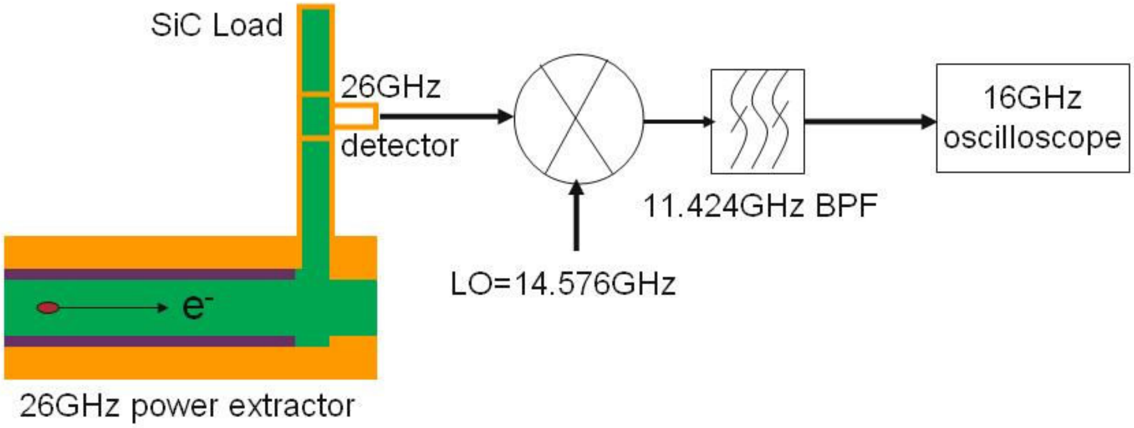

Figure 6.11. Diagram of the AWA Heterodyne Measurement System for the Beam Test of the 26GHz Power Extractor.

CHAPTER 7

HIGHER FREQUENCY II: DUAL-FREQUENCY HIGHER-ORDER-MODE POWER EXTRACTION AT 20.8GHZ AND 35.1GHZ

In Chapter 6, one approach to higher frequency has been described: the ID of the dielectric tube is reduced while the TM_{01} mode is kept as the interaction mode. With comparable dielectric constants (4.6 in Chapter 3 v.s. 6.64 in Chapter 6), the ID of the dielectric tube has been reduced from 12.04mm to 7.00mm, and the frequency has been increased from 7.8GHz to 26GHz. Although this approach is successful in pushing the frequency to the millimeter-wave range, the resultant small beam channel may lead to difficulties: firstly a small beam channel is hard for high charge to pass through, and secondly precision fabrication of such small dimensions is not easy. In this Chapter, an alternative way to push the frequency to millimeter-wave range is presented: the beam channel is kept big, while higher-order TM_{0n} modes ($n > 1$) other than the TM_{01} mode are used as interaction modes.

When an electron beam passes through a DL waveguide shown in Figure 1.1, it excites not only the TM_{01} mode, but also higher order TM_{0n} modes ($n > 1$). Figure 3.4 gives an example of the E_z (longitudinal electrical field) distribution of these TM_{0n} modes. From Table 3.3 it can be seen that the synchronous frequencies of these higher-order TM_{0n} modes ($n > 1$) have already reached the millimeter-wave or near-millimeter-wave region, therefore it is natural to employ these HOMs as interactions modes for millimeter-wave and near-millimeter-wave generation. However, since generally the TM_{01} mode has the strongest interaction with a beam, which means most beam power would still be transferred into this unintended mode, in order to improve efficiency an effective technique to suppress this mode is needed. Moreover, designing output couplers for HOMs is challenging. In this chapter, design considerations for a dual-frequency (20.8GHz for the TM_{02} mode and 35.1GHz for the TM_{03}) power extractor set with changeable output couplers are presented.

The organization of this chapter is as follows: in Section 7.1 enhancement of useful modes and suppression of unintended modes are discussed, in Section 7.2 the design of a dual-frequency decelerator guided by the principles in Section 7.1 is shown, and in Section 7.3 the design of HOM output couplers is finalized.

7.1 Mode Enhancement and Suppression in Bunch Train Power Extraction

In this section both coherent enhancement of a desired operation mode and suppression of an unintended mode are discussed. When a single on-axis particle bunch travels through a circular DL waveguide, it excites azimuthally symmetric TM_{0n} modes, and generally the power generated in one mode decreases with an increasing n. For simplicity, we assume the waveguide is lossless, and the beam is ultrarelativistic with a particle velocity of c. Without loss of generality, for an excited mode which may or may not be intentionally chosen as an interaction mode, with a synchronous frequency f_0 (at which $v_p = c$), the on-axis longitudinal e-field detected at the down stream end of the decelerator is (Gao 2008):

$$e_z(t) = \mathrm{rect}(t/\tau_s - 1/2)e^{j\omega_0 t} \tag{7.1}$$

where τ_s is the EM pulse length by single bunch (drain time), $\omega_0 = 2\pi \times f_0$, and $t = 0$ is the moment the EM pulse begins to exit the waveguide. The Fourier transform of (7.1) is

$$\widetilde{E}_z(\omega) = \frac{\tau_s}{\sqrt{2\pi}}\mathrm{sinc}\left[\frac{(\omega-\omega_0)\tau_s}{2\pi}\right]e^{-j\frac{(\omega-\omega_0)\tau_s}{2}} \tag{7.2}$$

where $\mathrm{sinc}(x) \equiv \sin(\pi x)/(\pi x)$.

When the drive beam is a train of M ($M > 1$) identical bunches repeated at a bunch frequency f_b, by superposition the Fourier transform of the total signal becomes

$$\tilde{E}_{z,total}(\omega) = \frac{\tau_s}{\sqrt{2\pi}} e^{-j\frac{(\omega-\omega_0)\tau_s}{2}} \mathrm{sinc}\left[\frac{(\omega-\omega_0)\tau_s}{2\pi}\right] \times \sum_{m=1}^{M} e^{-j2\pi\frac{\omega}{\omega_b}\times(m-1)} \tag{7.3}$$

where $\omega_b = 2\pi \times f_b$. The magnitude of Equation 7.3 can be written as

$$\left|\tilde{E}_{z,total}(\omega)\right| = A \cdot \left|\overline{G}(\omega)\right| \cdot \left|\overline{H}(\omega)\right| \tag{7.4}$$

where $A = \frac{M\tau_s}{\sqrt{2\pi}}$ is not related to the shape of $\left|\tilde{E}_{z,total}(\omega)\right|$, while

$$\overline{G}(\omega) = \mathrm{sinc}\left[\frac{(\omega-\omega_0)\tau_s}{2\pi}\right] \tag{7.5}$$

determines the spectrum shape of the EM pulse excited by a single bunch, and

$$\overline{H}(\omega) = \frac{1}{M}\sum_{m=1}^{M} e^{-j2\pi\frac{\omega}{\omega_b}\times(m-1)} \tag{7.6}$$

is the *normalized transfer function* due to bunch train excitation. It is noticed that in $\left|\overline{G}(\omega)\right|$, the central peak (centered at $f = f_0$) has a bandwidth of

$$BW_G = 2/\tau_s \tag{7.7}$$

from the first zero at one side of the peak to the first zero at the other side. And in $\left|\overline{H}(\omega)\right|$, highest peaks occur at integer multiples of f_b, with a bandwidth of

$$BW_H = 2f_b/M \tag{7.8}$$

from the first zero at one side of a highest peak to the first zero at the other side.

7.1.1 Coherent Enhancement of a Desired Mode . If this mode is intentionally chosen as the interaction mode, f_0 needs to be an integer multiple of f_b for coherent enhancement, i.e.

$$f_0 = kf_b, \qquad k \text{ is an integer and } k > 0 \tag{7.9}$$

Then

$$\left|\overline{H}(\omega_0)\right| = 1 \tag{7.10}$$

leads to

$$\left|\widetilde{E}_{z,total}(\omega_0)\right| = 1 \tag{7.11}$$

This means that the condition for coherent enhancement is satisfied. From Section 2.2.2.1 when

$$M \geq ceiling(f_b \tau_s), \tag{7.12}$$

the power of the generated EM pulse can reach the flat-top level, and is readily calculated as (loss included)

$$P = q^2 \frac{k_z}{4\beta_g}\left[\frac{r}{Q}\right]\left(\frac{1-e^{-\alpha_0 L}}{\alpha_0 T_b}\right)^2 \Phi^2 \tag{2.22}$$

7.1.2 Suppression of an Unintended Mode. If this mode is not the desired mode for interaction, it needs to be suppressed to allow more power to be transferred into the interaction mode in order to improve the efficiency of the power extractor. Generally in this case f_0 of this unintended mode is not an integer multiple of f_b, and one can always choose a proper length for the decelerator so that the separation between f_0 and the nearest kf_b ($k = 1, 2, \ldots$), $\Delta f = \left|kf_b - f_0\right|$, satisfies

$$\Delta f = l / \tau_s, \text{ where } l \text{ is an integer and } 1 \leq l \leq M/2 \tag{7.13}$$

Equation 7.13 leads to

$$\left|\overline{G}(k\omega_b)\right| = 0 \tag{7.14}$$

thus

$$\left|\widetilde{E}_{z,total}(k\omega_b)\right| = 0 \tag{7.15}$$

This means the highest peak of $\left|\overline{G}(\omega)\right|$ and a highest peak of $\left|\overline{H}(\omega)\right|$ around $f = f_0$ are intentionally displaced to effectively suppress the power generated in this unintended mode, as shown in Figures 7.1(a)-(c). Note that when $BW_H << BW_G$, i.e.

$$\tau_s << M / f_b, \tag{7.16}$$

which is often satisfied in long bunch excitation with a short decelerator, the power generated in the unintended mode is negligible.

7.2 Design of the Dual-frequency Decelerator

In this section, the design of the dual-frequency decelerator is described, and the corresponding CST MAFIA simulation is presented. As mentioned at the beginning of this chapter, the power extraction set consists of a dual-frequency decelerator and two changeable output couplers. The design of this decelerator is based on the current parameters of the AWA beamline. The beamline consists of an electron gun and a linac, both operating at 1.3GHz, leading to a bunch frequency f_b also at 1.3GHz. The electron gun is able to deliver 1-100nC charge per bunch with an r.m.s. bunch length of σ_z = 1.5-2.5mm. The beam energy is ~8MeV upon exiting the gun and is accelerated to ~15MeV by the linac. It is to be upgraded to 75MeV but in the decelerator design the beam is assume to be ultrarelativistic for simplicity.

The dielectric used for the decelerator is Corderite with a relative permittivity ε_r = 4.76. The TM_{02} and TM_{03} modes were chosen as operation modes since their synchronous frequencies (f_0) are in the near-millimeter-wave and millimeter-wave range with a beam channel of a manageable size. A systematic way to determine *a*, the inner

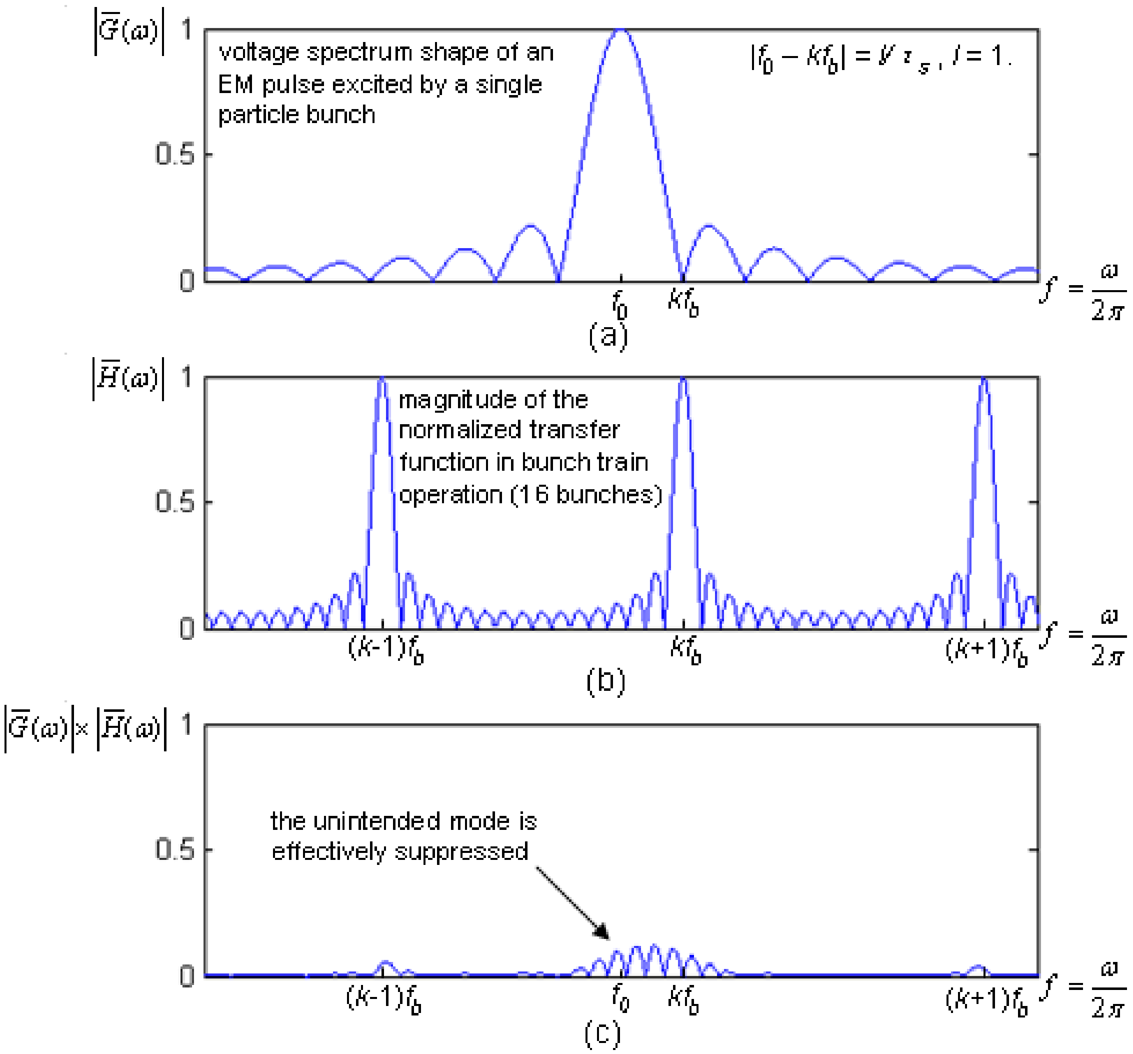

Figure 7.1. Mode Suppression of an Unintended Mode. (a). The voltage spectrum of an EM pulse excited by a single particle bunch, where the central frequency of an unintended mode is f_0; (b). the normalized transfer function due to bunch train operation; (c). the product of (a) and (b) leads to mode suppression.

radius of the dielectric tube and b, the outer radius of the tube is as follows: First we choose an f_0 for the TM$_{02}$ mode as an integer multiple of f_b, such as 20.8GHz, for which we obtain a curve of b v.s. a. Next we choose an f_0 for the TM$_{03}$ mode as an integer multiple of f_b, such as 35.1GHz, for which we get another curve of b v.s. a. Finally the intersection of the two curves determines the proper a and b. In practice, a and b were obtained with fine tuning as follows: First for a given a, we set f_0 for the TM$_{02}$ mode as 20.8GHz to obtain an outer radius b. Next we calculate the f_0 of the TM$_{03}$ mode to see if it is also an integer multiple of f_b. If not, we keep tuning a until the condition is met. When this happens, the right a and b are obtained. The f_0 of the TM$_{02}$ mode was determined to be 20.8GHz, the 16th harmonic of f_b; and the f_0 of the TM$_{02}$ mode was determined to be 35.1GHz, the 27th harmonic of f_b. Accordingly, a was determined to be 7.85mm, and b was determined to be 12.76mm. The loss tangent of the dielectric is assumed to be 0.0005 at both 20.8GHz and 35.1GHz. The metallic sleeve is assumed to be copper, with a conductivity 5.8×10^7s/m.

Unlike the TM$_{02}$ and TM$_{03}$ mode, the f_0 of the unintended TM$_{01}$ mode is 7.53GHz, not an integer multiple of f_b. Around 7.53GHz, the nearest harmonic of f_b is 7.8GHz, thus $\Delta f = |7.8-7.53| = 0.27$GHz. Recall Equation 7.13, with $l = 1$ (using the first zero), τ_s is calculated to be 3.7ns, which leads to a decelerator length $L = 35$cm. Considering the end effect, CST MAFIA simulation shows that L needs to be increased to 38cm in order to set the first zero of the TM$_{01}$ peak in $\left|\overline{G}(\omega)\right|$ to 7.8GHz, in single bunch excitation. When the bunch train contains 16 bunches, $M/f_b = 16/1.3\text{GHz} = 12.3\text{ns} = 3.3\tau_s$. If L is increased by l times (l is an integer and $1 < l \le M/2$) to set the l-th zero of $\left|\overline{G}(\omega)\right|$ to 7.8GHz, the TM$_{01}$ mode can be further suppressed. However, unfavorable consequence may show up.

Firstly, a longer decelerator is more difficult to construct, and secondly, detuning effects of the TM_{02} and TM_{03} modes may be more severe if the transverse dimensions of the decelerator are not accurate due to fabrication tolerance.

The characteristics and resultant power levels of the TM_{02} and TM_{03} modes are listed in Table 7.1, for which the power levels were calculated with the assumption of ultrarelativistic Gaussian electron bunches with a bunch length σ_z = 2mm. Results of calculation indicate that 95.9MW and 10.1MW of power can be generated in the TM_{02} and TM_{03} modes respectively, by a bunch train with a bunch frequency of 1.3GHz, and with charge of 50nC per bunch. From Equation 7.12 it can be seen that to reach this power level, at least three bunches are needed for the TM_{02} mode and two for the TM_{03} mode.

In order to confirm the TM_{01} mode is effectively suppressed in bunch train operation, CST MAFIA simulations were performed for both single bunch and bunch train excitations. For simplicity the structure was assumed to be lossless, which overestimates the power level slightly but should give negligible difference in the spectral shape. The charge of the on-axis beam was set at 1nC per bunch. Figures 7.2(a) and (b) show the near-axis (1-cell, 0.17mm away from the axis) longitudinal electric field probed at the downstream end of the decelerator. The reason of the near-axis arrangement is that if the probe is placed on the axis, the head of the probed signal will be affected by high-frequency numerical noise caused by a passing beam. From Figures 7.2(a) and (b) it can be seen the TM_{01} mode dominates the spectrum, but the first zero from its central peak has been intentionally placed at 7.8GHz. Figure 7.3 (a) shows the electric field excited by a train of 16 bunches, superposed from the one in Figure 7.2(a). The spectrum in

Table 7.1. Design Parameters of the Dual-frequency Dielectric-loaded Decelerator.

Modes	TM_{02}	TM_{03}
Synchronous frequency f_0 (GHz)	20.8	35.1
“r over Q” per unit length $[r/Q]$ (kΩ/m)	1.214	0.392
Quality factor Q	3170	3377
Shunt impedance per unit length r_{sh} (MΩ/m)	3.85	1.32
Normalized group velocity $\beta_g = v_g/c$	0.37	0.46
EM pulse length by single bunch τ_s (ns)	2.19	1.52
Number of consecutive bunches needed to reach Flat-top power level	3	2
Bunch form factor Φ	0.68	0.34
Generated P (KW) @ 1nC/bunch	38.4	4.05
Generated P (MW) @ 50nC/bunch	95.9	10.1

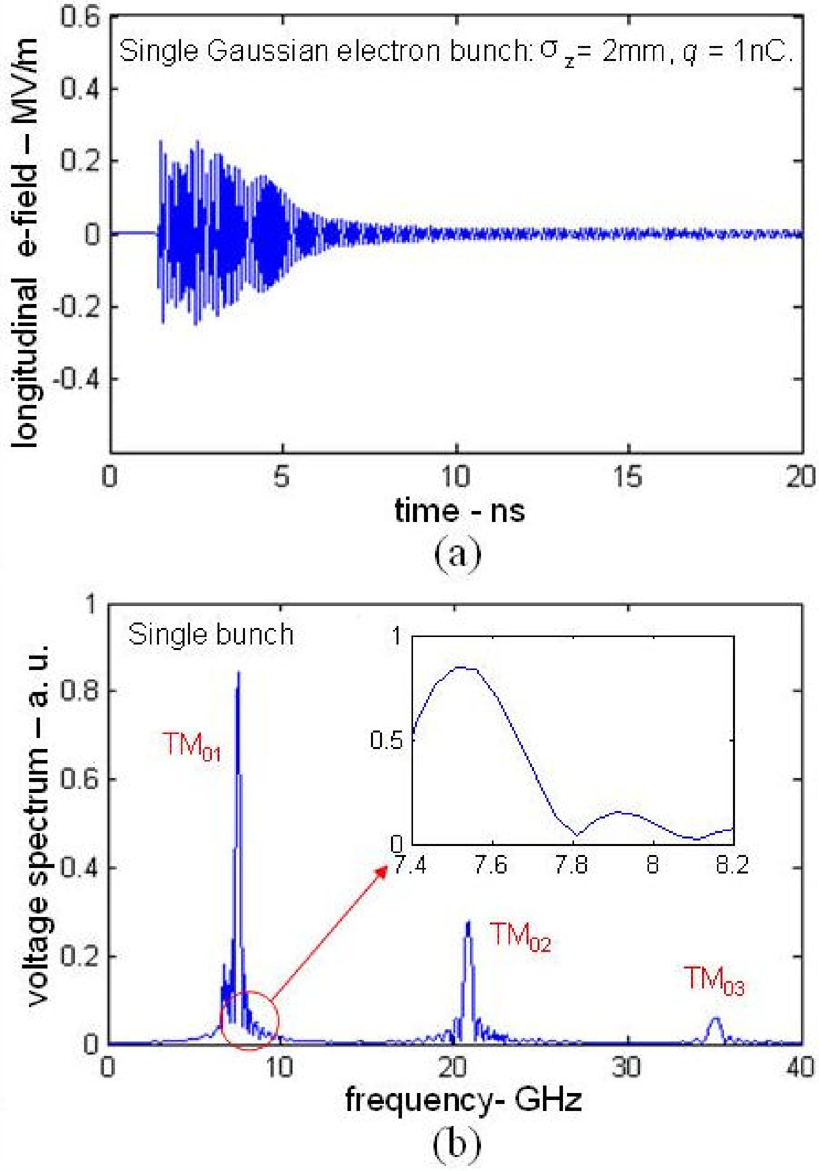

Figure 7.2. The Longitudinal Near-axis Electric Field at the Downstream End of the Decelerator Excited by a Single Bunch. (a). The e-field; (b). the voltage spectrum, where it can be seen the first zero of the TM$_{01}$ peak is intentionally placed at 7.8GHz.

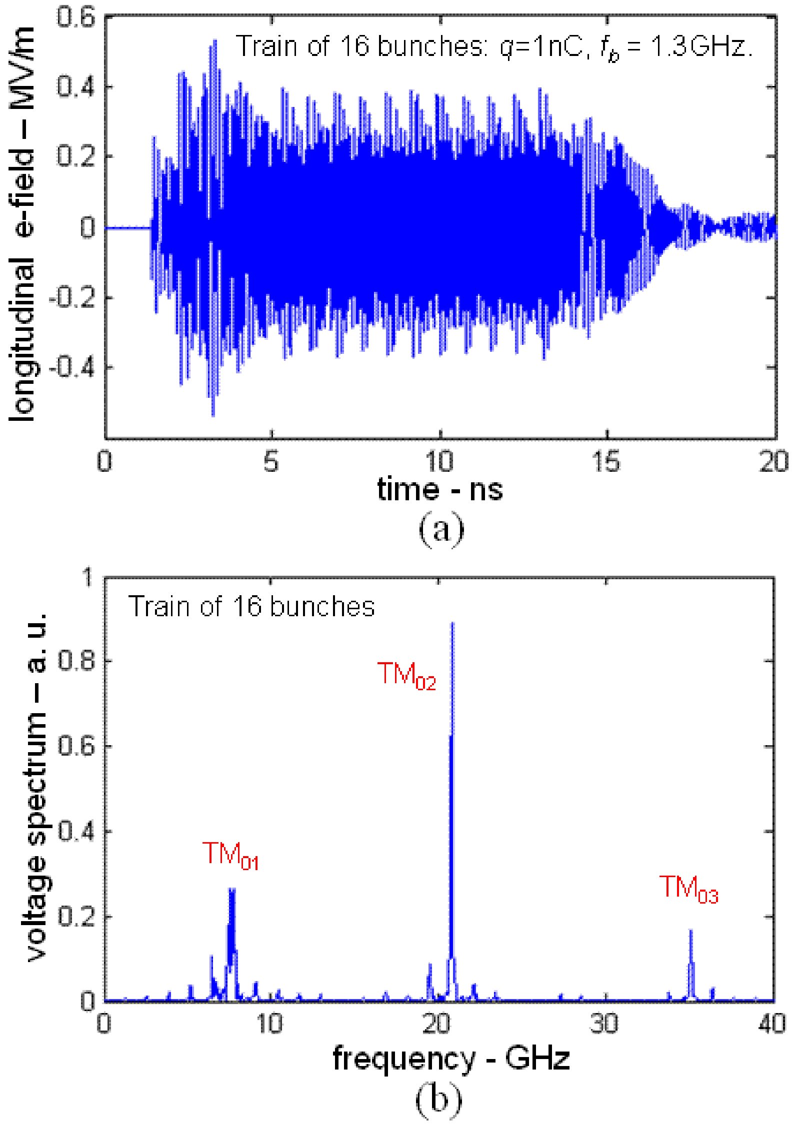

Figure 7.3. The Longitudinal Near-axis Electric Field at the Downstream End of the Decelerator Excited by a Train of 16 bunches. It is superposed from the single bunch curve. (a). The e-field; (b). the voltage spectrum, where it can be seen the TM_{01} mode is effectively suppressed.

Figure 7.3(b) shows that the TM_{01} mode is effectively suppressed, with much lower relative strength (from 3 times the height of the TM_{02} peak in single bunch excitation to only 1/3 in bunch train excitation), while the TM_{02} and TM_{03} modes are enhanced. This observation on the simulation results confirms the effectiveness of the design in the suppression of the unintended TM_{01} mode.

7.3 Design of the HOM Output Coupler

For flexibility the dual-frequency decelerator discussed in Section 7.2 is designed to be used with two changeable output couplers, one for the TM_{02} mode and the other for the TM_{03} mode. The idea is that one can choose the copper housing of the coupler one needs and bolt it with the copper sleeve of the decelerator, then slide in the dielectric tube or tubes, resulting in a power extractor for either 20.8GHz or 35.1GHz. To simplify the design process for each output coupler, each of the TM_{02} and TM_{03} modes is first converted to the TM_{01} mode in a smaller hollow circular waveguide with a tapered section. The TM_{01} mode is then converted to the TE_{10} mode in a standard rectangular waveguide. In this section we will describe the design of the TM_{02}/TM_{03}-TM_{01} mode converters, the TM_{01}-TE_{10} mode converters, and the simulation results for the two entire output couplers. The background material in the models is perfect electric conductor.

7.3.1 The TM_{02}/TM_{03}–TM_{01} Mode Converters. The guideline for designing the TM_{02}/TM_{03}-TM_{01} mode converters is to make the geometries as simple as possible, with minimum insertion losses and adequate bandwidths. Figure 7.4 shows a view of the 20.8GHz TM_{02}-TM_{01} mode converter by a cross section along the axis. The beam channel of the DL waveguide is extended at the downstream end to be a hollow circular waveguide. A vacuum ring is placed at the end of the DL waveguide as a choke

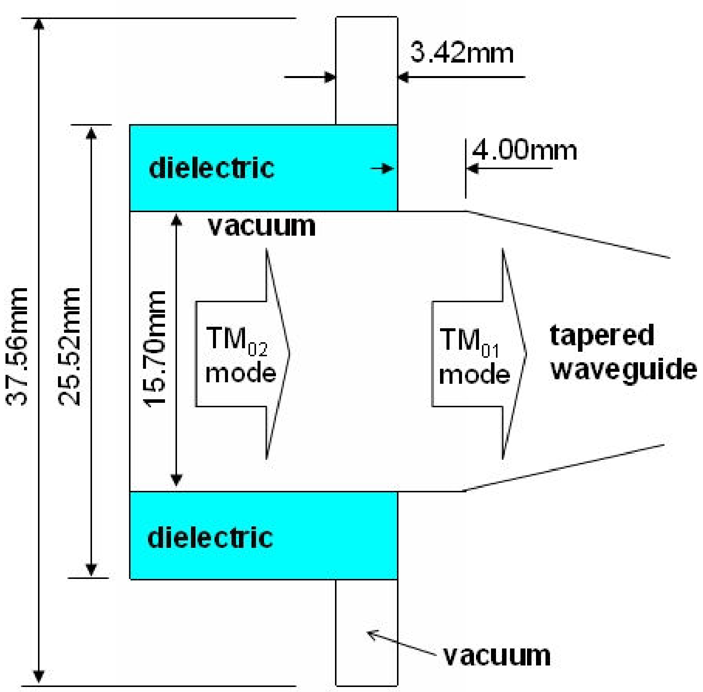

Figure 7.4. The 20.8GHz TM_{02}-TM_{01} Mode Converter. The cutplane is along the axis.

for impedance matching. The hollow waveguide is then tapered to be matched with the TM_{01}-TE_{10} mode converter. Simulation with CST Microwave Studio shows the converter (without the taper section) has an insertion loss $S_{21} \approx -0.2$dB at 20.8GHz, and the S_{21} is better than -0.3dB in the range from 20GHz to 21.6GHz.

Figure 7.5 shows a view of the 35.1GHz TM_{03}-TM_{01} mode converter by a cross section along the axis. The DL waveguide is first stepped down with a smaller *b* value to convert most power into the TM_{02} mode. A ring choke is then used to convert the TM_{02} mode to the TM_{01} mode. The reflected signals at the two transition points are expected to cancel to improve transmission. The hollow waveguide is slightly larger than the beam channel and tapered down for the TM_{01}-TE_{10} mode converter as well. Simulation with CST Microwave Studio shows the converter (without the taper section) has an insertion loss $S_{21} \approx -0.35$dB at 35.1GHz, and the S_{21} is better than -0.5dB in the range from 33.1GHz, the lower frequency limit in simulation, up to 36GHz.

7.3.2 The TM_{01} –TE_{10} Mode Converters.

Once the TM_{02}/TM_{03} mode is converted to the TM_{01} mode in a hollow circular waveguide, a TM_{01}-TE_{10} mode converter can be used for the rectangular output waveguide. The geometry of the designed TM_{01}-TE_{10} mode converter is shown in Figure 7.6 and is similar to the one shown in Section 6.2. First the hollow circular waveguide is tapered to a smaller size to suppress harmful reflection of quadruple modes. Two edges in the high gradient region are bent with a bending radius *rbend* (shown in Figure 7.6). The downstream beam channel after the rectangular waveguide is beyond cutoff for the TM_{01} mode, and it can be used for beam monitoring. Power in the TM_{01} mode is coupled into a wide rectangular waveguide which is later tapered to a standard WR42 waveguide for 20.8GHz output or to a WR28 waveguide for

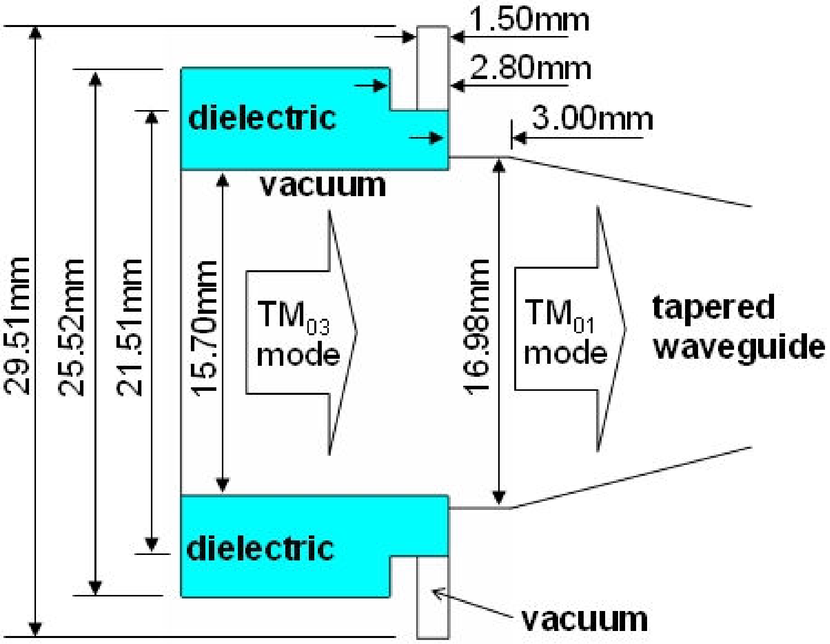

Figure 7.5. The 35.1GHz TM_{03}-TM_{01} Mode Converter. The cutplane is along the axis.

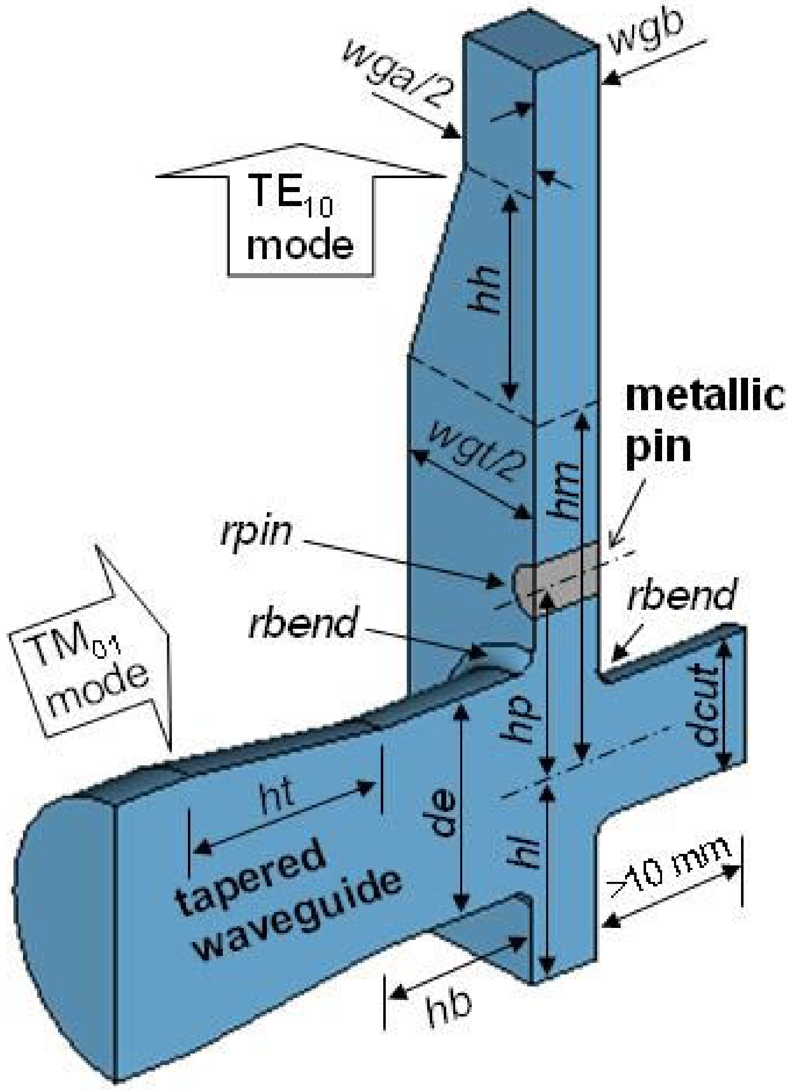

Figure 7.6. The TM_{01}-TE_{10} Mode Converter. The cutplane is along the axis of the beam channel. For 20.8GHz (unit: mm): *de* =12.50, *dcut* = 7.50, *hb* =10.00, *hh* = 12.50, *hl* = 11.72, *hm* = 20.20, *hp* = 10.60, *ht* = 12.70, *rbend* = 1.00, *rpin* = 1.50, *wga* = 10.668, *wgb* = 4.318, *wgt* = 19.25. For 35.1GHz (unit: mm): *de* = 7.40, *dcut* = 4.44, *hb* = 6, *hh* = 7.41, *hl* = 6.95, *hm* = 11.97, *hp* = 6.27, *ht* = 38.10, *rbend* = 0.60, *rpin* = 0.89, *wga* = 7.112, *wgb* = 3.556, *wgt* = 11.41.

35.1GHz output. A metallic pin with a radius *rpin* (shown in Figure 7.6) is used for impedance matching. CST Microwave Studio simulations show that for the 20.8GHz parameters the insertion loss is negligible at 20.8GHz, and for the 35.1GHz parameters the insertion loss is approximately -0.2dB.

7.3.3 The Entire TM_{02}/TM_{03}–TE_{10} Output Couplers. Finally the TM_{02}/TM_{03}-TM_{01} mode converters are cascaded with corresponding TM_{01}-TE_{10} mode converters for CST Microwave Studio simulations. Figure 7.7 shows the simulated S-parameters for the entire 20.8GHz TM_{02}-TE_{10} output coupler. The insertion loss S_{21} = -0.26dB at 20.8GHz indicates power coupling efficiency of 94.3%, and it is better than -1dB in the range from 20.40GHz to 21.29GHz. The reflection is S_{11} = -20.98dB at 20.8GHz and is lower than -15dB in the range from 20.65GHz to 20.94GHz. Figure 7.8 shows the simulated S-parameters for the entire 35.1GHz TM_{03}-TE_{10} output coupler. The insertion loss S_{21} = -0.66dB at 35.1GHz indicates power coupling efficiency of 85.9%, and it is better than -1dB from 34.6GHz, the lower frequency limit in simulation, up to 35.54GHz. The reflection is S_{11} = -25.77dB at 35.1GHz and is lower than -25dB in the range from 34.90GHz to 35.26GHz. The results are close to what would be expected from results in Sections 7.3.1 and 7.3.2. It can also be observed that the sum of $|S_{21}|^2$ and $|S_{11}|^2$ is always smaller than 1, since many other unintended modes are also excited by the TM_{02}/TM_{03} mode.

From the power coupling efficiencies (calculated from S_{21}: 94.3% at 20.8GHz and 85.9% at 35.1GHz) and power levels calculated in Table 7.1, we can conclude that when the drive bunch train has charge of 50nC per bunch, 95.9×0.943 = 90.4MW of power is expected to be extracted at 20.8GHz, and $10.1\times0.859 = 8.68$MW of power is expected to be extracted at 35.1GHz.

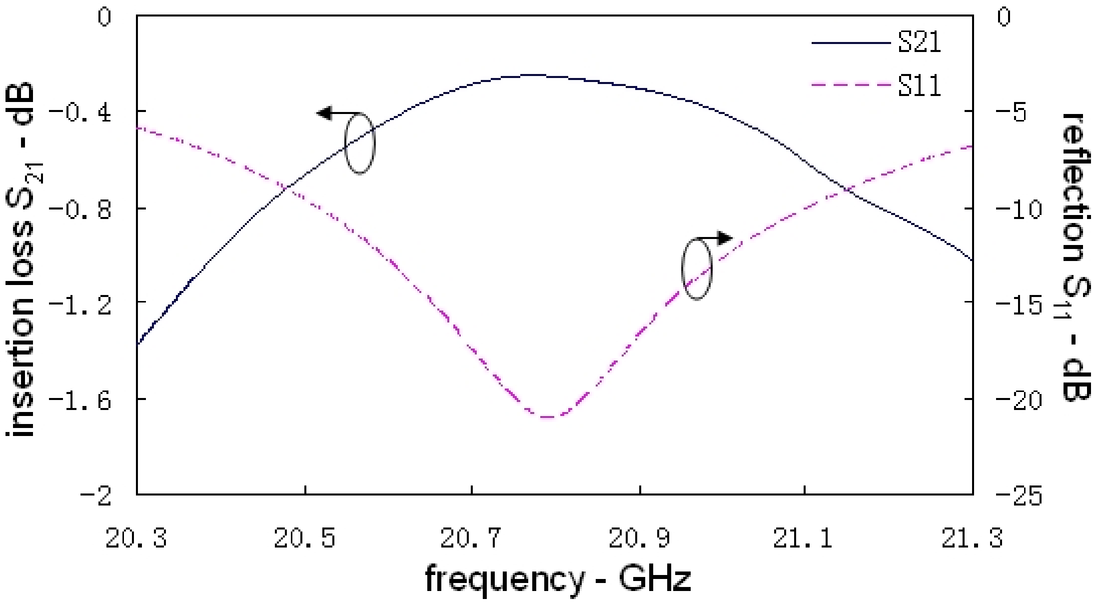

Figure 7.7. Simulated S-parameters of the Entire 20.8GHz TM_{02}-TE_{10} Output Coupler.

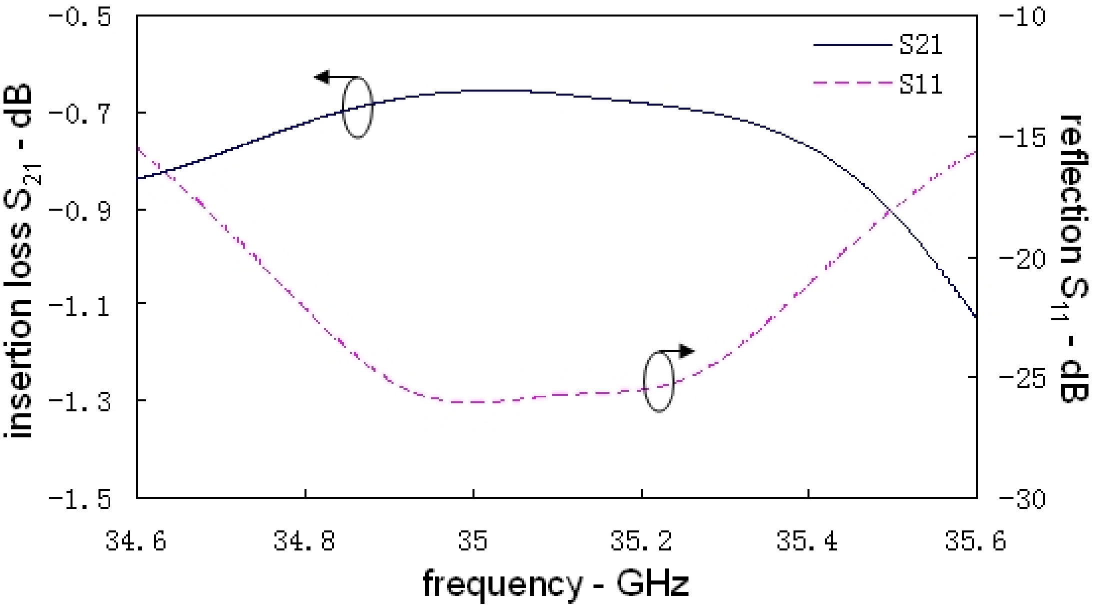

Figure 7.8. Simulated S-parameters of the Entire 35.1GHz TM_{03}-TE_{10} Output Coupler.

CHAPTER 8

CONCLUSIONS

The DL structure is an alternative to the traditional disc-loaded structure for future charged particle acceleration. Wakefield power extraction based on the DL structure is potentially a good approach for high power RF source development, mainly due to the simplicity in geometry, the ease in suppressing harmful deflecting modes, and the field distribution that mitigates breakdown on the metallic wall of the structure.

As part of the DL TBA plan at AWA, a 7.8GHz DL power extractor has been designed and tested with the intense electron beam, which was developed specifically for wakefield study. In this thesis, the fundamentals of both particle accelerators and high power RF sources are introduced, including previously investigated acceleration structures and power generation techniques. Mathematical expressions of power extraction using a constant-impedance traveling-wave structure are also given. Numerical simulations on the 7.8GHz power extractor agree with theoretical analysis, and they both further agree with electron beam tests. 30MW of power has been generated in single bunch tests and 44MW in bunch train tests, also 10ns and 22ns RF pulses have been generated in bunch train tests. Furthermore, a 26GHz DL power extractor, and a 20.8/35.1GHz HOM dual-frequency power extractor set have also been designed, which shows the potential of power extraction in the millimeter-wave range.

The scheme for generation of electron bunch trains has also been demonstrated. With a laser beam splitting set, the single laser pulse was split into two trains of micropulses, which were delayed by different distances. Later on, with different configurations of recombination, electron bunch trains of different lengths were generated. Picosecond-level control of the spacing between two adjacent electron bunches was done with both beam energy monitoring and the charge-versus-launch-phase curve, and it has been experimentally demonstrated by in-phase superposition of wakefield excited by consecutive bunches. This scheme has the potential for high power RF pulse shaping, since by placing ND filters in the laser paths, the intensities of the laser micropulses can be adjusted differently and thus the RF pulse can be shaped.

Although tests on the prototype 7.8GHz power extractor are successful in demonstrating high power multi-nanosecond pulse generation, a few more changes are needed to reach the goal of a stable 100MW-level RF source: replacing the current magnesium photocathode with a cesium telluride photocathode which has a much higher QE, installing more linacs powered by additional klystrons, and effective beam confinement under high charge condition.

In the 7.8GHz power extraction test, the maximum charge of a train consisting of 16 electron bunches is only ~5nC per bunch, which is only able to generate 2.4MW of power with 769ps bunch spacing and 0.77MW of power with 1.538ns bunch spacing. One limitation of the low charge is that the QE of the present magnesium photocathode is relatively low (~10^{-4}), thus for a given amount of energy inside an input laser micropulse the charge of the generated electron bunch is low. Another limitation is that the number of laser beam splitters through which each laser micropulse goes and mirrors on which each laser micropulse is reflected, is very large (rangings from 9 to 18 for each micropulse). For example, even for 18 splitters/mirrors with a 3% low loss each, the final micropulse energy is only 58% of the initial value. While the first limitation can be bypassed with a high QE photocathode, the second limitation is almost unavoidable due to the limited available location for the laser splitting apparatus. At AWA, a cesium telluride photocathode with a much higher QE (~10^{-2}) is being developed, which is expected to greatly increase charge generation (at least 50nC per bunch). The new beam current calculated from 769ps bunch spacing will be at least 65A within the pulse. Since the QE of the new photocathode is two orders of magnitude higher than the present one, when the new one is being used, it is expected that the space charge effect will replace charge generation as the new bottleneck.

In order to increase the beam power at AWA so that more power can be extracted from the beam without catastrophic space charge effect, a few more linac cavities are planned to be added into the beamline together with more klystrons. Powered by the new klystrons, the linacs are expected to push the present 15MeV beam energy to 75MeV. From the calculated 65A of beam current with the new CsTe photocathode, the beam power will be approximately 5GW, which is sufficient not only for this single-section power extraction, but also for future multi-section power extraction or in other words, the DL TBA.

Beam confinement techniques were not used for the deceleration waveguide during the first 7.8GHz power extraction tests since the charge per bunch was as low as ~5nC in bunch train tests. However in the future these techniques will be necessary since much larger bunch charge will be present and much stronger space charge effect will show up, especially head-tail instability. One example is that during the 7.8GHz single bunch tests, the maximum charge transmitted was 66nC, which was only 40% of the 160nC of charge coming out of the electron gun. In order to fully make use of future high bunch charge as a "carrier" to convert the power from the 1.3GHz klystrons to their harmonics (the 6th for 7.8GHz, the 20th for 26GHz, and in HOM operation the 16th for 20.8GHz and the 27th for 35.1GHz), charge transmission needs to be improved. An attempt has been made to solve the problem for a beam traveling through a DL waveguide, where the use of a focusing-defocusing channel around the decelerator can be used to control the head-tail instability.

BIBLIOGRAPHY

Aldophsen, C., and L. Laurent. 2007. High power test of an X-band slotted-iris accelerator structure at NLCTA. *Proc. Particle Acceleration Conference*:2191-2193.

APS. 2009. Available from http://www.aps.anl.gov/About/APS_Overview/storage_ring.html.

AWA. 2009. Available from http://www.hep.anl.gov/awa/links/area-layout.htm.

Bair, J. K., J. A. Biggerstuff, C. M. Jones, J. D. Larson, J. W. McConnell, W. T. Milner and N. F. Ziegler. 1975. Design consideration of the ORBL 25MW tandem accelerator. *IEEE Tran. Nucl. Sci.* 22:1655-1658.

Baker, R. J., and E. Schamiloglu. 2001. *High-power microwave sources and technologies*: IEEE.

Blank, M., B. G. Danly, B. Levush, P. E. Lathan and D. E. Pershing. 1997. Experimental demonstration of a W-band gyroklystron amplifier. *Phys. Rev. Lett.* 79:4485-4488.

Brau, J., Y. Okada, N. Walker, A. Djouadi, J. Lykken, K. Mönig, M. Oreglia, S. Yamashita, N. Phinney, N. Toge, T. Behnke, C. Demerell, J. Jaros and A. Miyamoto, ed. 2007. International Linear Collider Reference Design Report.

Braun, H., R. Corsini, T. D'Amico, J. Delahaye, G. Guignard, C. D. Johnson, A. Millich, P. Pearce, A. J. Riche, L. Rinolfi, R. Ruth, D. Schulte, L. Thorndahl, M. Valentini, I. H. Wilson and W. Wuensch. 1998. The CLIC RF power source: a novel scheme of two-beam acceleration for electron-positron linear colliders. CLIC-Note-364.

Bryant, P. J. 1993. A brief history and review of accelerators. In *CERN Accelerator Technology and Physics Introduction*.

CERN. 2008. *LHC Design Report*. Available from http://ab-div.web.cern.ch/ab-div/Publications/LHC-DesignReport.html.

Chao, A. W. 1993. *Physics of Collective Beam Instabilities in High Energy Accelerator*: John Wiley & Sons.

Cheng, J., X. Xu, W. J. Lawson, J. P. Calame, M. Castle, B. P. Hogan, V. L. Granatstein, G. S. Nusinovich and M. Reiser. 1999. Experimental studies of a high power, X-band, coaxial gyroklystron. *IEEE Trans. Plasma Sci.* 27:1175-1187.

Chojnacki, E., W. Gai, P. Schoessow, and J. Simpson. 1991. Accelerating field step-up transformer in wake-field accelerators. *Proc. Particle Acceleration Conference*:2557-2559.

Cockcroft, J. D., and E. T. S. Walton. 1932. Experiment with high velocity ions. *Proc. Royal Soc., Series A* 136:619-630.

Conde, M. E. 2007. Survey of advanced dielectric wakefield accelerators. *Proc. Particle Acceleration Conference*:1899-1903.

Conde, M. E., S. Antipov, F. Franchini, W. Gai, F. Gao, C. Jing, R. Konecny, W. Liu, J. G. Power, H. Wang, and Z. Yusof. 2006. High gradient wakefields in dielectric loaded structures. *AIP Conf. Proc.* 877:260-265.

Conde, M. E., W. Gai, R. Konecny, J. G. Power, P. Schoessow and P. Zou. 1999. RF power generation and coupling measurements for the dielectric wakefield step-up transformer. *AIP conf. Proc.* 472:626-634.

CST. 2000. MAFIA 4.0. Computer Simulation Technology.

CST. 2003. Microwave Studio 5.0.0. Computer Simulation Technology.

Danly, B. 1995. RF sources for linear colliders. *AIP Conf. Proc.* 335:25-28.

Flesher, G., and G. Cohn. 1951. Dielectric loading for waveguide linear accelerators. *AIEE Trans.* 70:887-893.

Gai, W., A. D. Kanareykin, A. L. Kustov, and J. Simpson. 1997. Numerical simulations of intense charged-particle beam propagation in a dielectric wake-field accelerator. *Phys. Rev. E* 55:3481-3488.

Gai, W., and P. Schoessow. 2001. Design and simulation of a high-frequency high-power RF extraction device using a dielectric-loaded waveguide. *Nucl. Instum. Meth. – A* 459:1-5.

Gao, F., M. Conde, W. Gai, R. Konecny, W. Liu, J. Power, Z. Yusof, T. Wong and C. Jing. 2008. Design and testing of a 7.8GHz power extractor using a cylindrical dielectric-loaded Waveguide. *Phys. Rev. ST-AB* 11:041301.

Gao, F., M. E. Conde, W. Gai, C. Jing, R. S. Konecny, W. Liu, J. G. Power, T. Wong and Z. Yusof. 2009. Multi-nanosecond high power pulse generation at 7.8GHz with a dielectric-loaded power extractor. *IEEE Trans. Nucl. Sci.* 56(3):1492-1497.

Gold, S. H., and G. S. Nusinovich. 1997. Review of high-power microwave source research. *Rev. Sci. Instru.* 68:3945-3974.

Gold, S. H., A. K. Kinkead, W. Gai, J. G. Power, R. Konecny, J. Long, C. Jing, S. G. Tantawi, C. D. Nantitsa. 2007. Development of a dielectric-loaded accelerator. *Proc. Particle Acceleration Conference*:3211-3213.

Gouveia, E. S., V. Granatstein, B. Hogan, B. Huebuschman, W. Lawson. 2002. Development of high-gain second harmonic gyroklystron for accelerator applications. *Proc. EPAC*:2320-2322.

Granatstein, V. L., B. Levush, B. G. Danly and R. K. Parker. 1997. A quarter century of gyrotron research and development. *IEEE Trans. Plasma Sci.* 25:1322-1335.

Ives, R. L., J. M. Neilson, M. Read, M. Mizuhara, T. Robinson, D. Marsden, W. Lawson and B. Hogan. 2003. 10MW, 91GHz gyroklystron for high frequency accelerator research. *Proc. Particle Acceleration Conference*:1119-1121.

Jing, C. 2004. Group velocity effect on wakefield calculation. Argonne Wakefield Accelerator notes WF-222.

Jing, C., A. Kanareykin, J. G. Power, M. Conde, Z. Yusof, P. Schoessow and W. Gai. 2007. Observation of enhanced transformer ratio in collinear wakefield acceleration. *Phy. Rev. Lett.* 98:144801.

Jing, C., A. Kanareykin, P. Schoessow, W. Gai, R. Konecny, J. G. Power, M. Conde, F. Gao, S. Kazakov and A. Kustov. 2009. Development of 26GHz dielectric-based wakefield power extractor. *AIP Conf. Proc.* 1086:458-463.

Jing, C., W. M. Liu, W. Gai, J. G. Power and T. Wong. 2005. Mode analysis of multilayered dielectric-loaded accelerating structure. *Nucl. Instrum. Meth. - A* 539:445-454.

Kübner, K. 1992. Two-beam Linear Colliders. *XVth International Conf. on High Energy Accelerators*:791.

Lawrence, E. O., and N. E. Edlefsen. 1930. On the production of high speed protons. *Science*, 376-377.

Lawson, W., J. P. Calame, B. P. Hogan, M. Skopec, C. D. Striffler and V. L. Granastein. 1992. Performance characteristics of a high-power X-band two-cavity gyroklystron. *IEEE Trans. Plasma Sci.* 20:216-223.

Leemans, W. P., B. Nagler, A. J. Gonsalves, Cs. Tóth, K. Nakamura, C. G. R. Geddes, E. Esarey, C. B. Schroeder and S. M. Hooker. 2006. GeV electron beams from a centimetre-scale accelerator. *Nature Phys.* 2:696-699.

McMillan, E. M. 1945. The synchrotron - a proposed high-energy particle accelerator. *Phys. Rev., Letter to the editor* 68:143-144.

Neal, R. B. 1968. *The Stanford's two-mile accelerator*: W. A. Benjamin Inc.

Newsham, D., A. Smirnov, D. Yu, W. Gai, R. Konecny, W. Liu, H, Braun, G. Garron, S. Deobert, L. Thorndahl, I. Wilson and W. Wuensch. 2003. Construction and Testing of a 21 GHz Ceramic Based Power Extractor. *Proc. Particle Acceleration Conference*:1156-1158.

Nezhevenko, O. A., M. A. LaPointe, V. P. Yakovlev, J. L. Hirshfield. 2003. 34 GHz, 45MW pulsed magnicon: first results. *Proc. Particle Acceleration Conference*:1131-1133.

Nezhevenko, O. A., V. P. Yakovlev, M. A. LaPointe, E. V. Kozyrev, S. V. Shchelkunov and J. L. Hirshfield. 2005. Status of 34GHz, 45MW pulsed magnicon. *Proc. Particle Acceleration Conference*:1922-1924.

Nezhevenko, O. A., V. P. Yakovlev, S. H. Gold and B. Hafizi. 1994. Design of a high power X-band magnicon amplifier. *IEEE Trans. Plasma Sci.* 2:785-795.

Plettner, T., R. L. Byer, E. Colby, B. Cowan, C. M. S. Sears, J. E. Spencer, and R. H. Siemann. 2005. Visible-laser acceleration of relativistic electrons in a semi-infinite vacuum. *Phys. Rev. Lett.* 95:134801.

Proch, D. 1998. Superconducting cavities for accelerators. *Rep. Prog. Phys.* 61:431-482.

Schoessow, P., M. E. Conde, W. Gai, R. Konecny, J. Power, and J. Simpson 1998. High power radio frequency generation by relativistic beams in dielectric structures. *J. Appl. Phys.* 84:663-667.

Sessler, A. M. 1982. The free electron laser as a power source for a high-gradient accelerating structure. *AIP Conf. Proc.* 91:154-159.

Sessler, A. M., and S. S. Yu. 1987. Relativistic klystron two-beam accelerator. *Phys. Rev. Lett.* 59:2439-2442.

Vaganian, S., and H. Henk. 1995. The Panofsky-Wenzel theorem and general relations for the wake potential. *Particle Accelerators* 48:239-242.

Van de Graaff, R. J., 1931. A 1,500,000 volt electrostatic generator. *Phys. Rev.* 38:1919-1920.

Varian, R. H., and S. F. Varian. 1939. A high frequency oscillator and amplifier. *J. Appl. Phys.* 10:321-327.

Waloschek, P. 1994. The infancy of particle accelerators. DESY 94-039.

Wangler, T. 1998. *RF Linear Accelerators*: John Wiley & Sons, Inc.

Whittum, D. 1998. Introduction to electrodynamics for microwave linear accelerators. SLAC-PUB-7802.

Wilson, P. B. 1991. High energy electron linacs: applications to storage ring RF systems and linear colliders.

———. 1996. Advanced RF power sources for linacs. SLAC-PUB-7263.

Yu, D., D. Newsham and A. Smirnov. 2002. 21-GHz ceramic RF power extractor. *AIP Conf. Proc.* 647:484-505.

Zhang, T. B., J. Hirshfield, T. Marshall, and N. Hafizi. 1997. Stimulated dielectric wake-field accelerator. *Phys. Rev. E* 56:4647-4655.

Zou, P. 2001. X-band dielectric loaded RF driven accelerator structures: theoretical and experimental investigation. Department of Electrical and Computer Engineering, Illinois Institute of Technology, Chicago. PhD dissertaion.

Zou, P., W. Gai, R. Konecny, X. Sun, T. Wong and A. Kanareykin. 2000. Construction and testing of an 11.4GHz dielectric structure based traveling wave accelerator. *Rev. Sci. Instru.* 71:2301-2304.

High Energy Physics Division
Argonne National Laboratory
9700 South Cass Avenue, Bldg. 362
Argonne, IL 60439-4815

www.anl.gov

A U.S. Department of Energy laboratory
managed by UChicago Argonne, LLC